

The Polar Wind: Recent Observations

Andrew W. Yau^a, Takumi Abe^b, and W.K. Peterson^c

^aDepartment of Physics and Astronomy, University of Calgary, 2500 University Dr. NW, Calgary, Alberta T2N1N4 Canada

^bInstitute of Space and Astronautical Science, Japan Aerospace Exploration Agency, 3-1-1 Yoshinodai, Sagami-hara, Kanagawa 229-8510 Japan

^cLaboratory of Atmospheric and Space Physics, University of Colorado, 1234 Innovation Drive, Boulder, Colorado 80304 USA

Corresponding Author:

Andrew W. Yau
Department of Physics and Astronomy,
University of Calgary,
2500 University Dr. NW,
Calgary, Alberta T2N1N4 Canada
1-403-220-8825, fax 1-403-220-3616, yau@phys.ucalgary.ca

Abstract

The polar wind is an ambipolar outflow of thermal plasma from the high-latitude ionosphere. Satellite-borne ion composition observations above 1000 km altitude reveal several important features in the polar wind that are unexpected from “classical” polar wind theories and attributable to several “non-classical” ion acceleration mechanisms. These include day-night asymmetry in velocity, appreciable O^+ flow at high altitudes, and significant electron temperature anisotropy in sunlit polar wind. Significant questions remain on the relative contribution of the different sources of the high-altitude O^+ polar wind and the relative importance between the classical and non-classical ion acceleration mechanisms.

Keywords: Polar wind, Ionosphere, Outflow

1. Introduction

The discovery of O^+ ions (Shelley et al., 1972) in the magnetosphere revealed the ionosphere as an important source of magnetospheric plasma, and it is now generally accepted that there are two major sources of plasmas in the magnetosphere: ion outflows from the polar ionosphere, and direct or indirect entry of the solar wind plasma. Indeed, the polar ionosphere is a significant and at times dominant source of plasma to the magnetosphere, and the polar wind is one of the principal contributors of this source of plasma.

The discovery of the magnetotail, plasmopause, and atmospheric helium attrition in the early years of space exploration led to the postulation of the existence of the polar wind in the late sixties. In its original concept, the polar wind consists primarily of electrons and light (H^+ and He^+) ions, and is an ambipolar outflow of thermal plasma from the high-latitude ionosphere to the magnetosphere along “open” geomagnetic field lines. Axford (1968) coined the term “polar wind” to describe the supersonic nature of the thermal plasma expansion and outflow, in analogy to the supersonic expansion of the solar wind plasma from the solar corona into interplanetary space.

In this issue, Lemaire et al. (2007) review the history of development of polar wind theories and models, as well as that of earlier polar wind observations. Tam et al. (2007) review in details the various collisionless and collisional kinetic models of the polar wind, and compare them with the MHD and transport-equation based models, while the review of Schunk (2007) focuses on global, time-dependent simulation models. The limitations of both polar wind observations and theory have led to confusion about what is and what is not meant by the term “classical polar wind” and whether this distinction is physically relevant. The objective of this review is to assess the current state of observation knowledge of the polar wind, based primarily on observations on ISIS-2, DE-1, Akebono and POLAR, and discuss gaps and unresolved questions in our present knowledge.

The organization of this review is as follows. Section 1 briefly outlines the historical background of recent polar wind observations, and the scope of this review in the context of ionospheric ion acceleration and outflow. Section 2 identifies key predictions from polar wind models that had motivated – and in some cases helped shape – the observations. The discussion in section 2 focuses on the theoretical issues that have led to the introduction of the term “classical polar wind”, and includes a summary of predictions made by polar wind theories and simulations. Section 3 reviews the observed characteristics of the polar wind on DE-1, Akebono, POLAR, and other satellites at various altitudes and under various geophysical (ionospheric, magnetic and solar activity) conditions. Section 4 compares the observed and theoretically predicted characteristics, and discusses remaining questions in the existing observations as well as the current polar wind literature.

Conceptually, the spatial separation between the free electrons and the heavier, (mainly O^+) gravitationally bound ions results in an ambipolar electric field, which continuously accelerates (mainly) the light ions upward in the polar ionosphere. Along “open” magnetic field lines, the polar wind expands at supersonic speed into the magnetotail lobes in response to the plasma pressure gradient (and other forces) between the polar ionosphere and the magnetotail. Such ion escape was initially predicted as a bulk subsonic flow of light thermal ions through plasma diffusion (Nishida, 1966) or thermal evaporation (Dessler and Michel, 1966), and was subsequently suggested to be supersonic (Axford, 1968; Banks and Holzer, 1968), and confirmed experimentally by in-situ satellite observations.

At low altitudes (below a few thousand km), the dominant source of polar wind H^+ is the accidentally resonant charge exchange reaction between O^+ and H. The source of He^+ is the photo-ionization of neutral helium. The polar wind ion flux is limited by the rate of production of the outflowing ions and that of their Coulomb collisions with the other ions. For typical ionospheric densities and temperatures in the topside ionosphere and under steady-state conditions, these sources and Coulomb collision processes result in a maximum limiting H^+ flux of $\sim 3 \times 10^8 \text{ cm}^{-2} \text{ s}^{-1}$ at 1000 km altitude at solar minimum. The H^+ limiting flux decreases to $\sim 1 \times 10^8 \text{ cm}^{-2} \text{ s}^{-1}$ near solar maximum due to the increase in exospheric temperature and the corresponding increase in neutral hydrogen density at high altitude. In comparison, the limiting He^+ flux is dependent primarily on the neutral atmospheric He and N_2 , which affect the photo-ionization rate of He and the loss rate of He^+ due to the He^+-N_2 charge-exchange reaction, respectively, and varies from $\sim 1-3 \times 10^5 \text{ cm}^{-2} \text{ s}^{-1}$ in solar minimum summer to $\sim 0.5-1.5 \times 10^7 \text{ cm}^{-2} \text{ s}^{-1}$ in solar maximum winter, the winter-to-summer and solar-maximum-to-minimum flux ratio being ~ 25 and ~ 2 , respectively (Raitt and Schunk 1983). Thus, the polar wind flux is expected to be primarily H^+ , with a few percent of He^+ .

Hoffman (1970), Brinton et al. (1971), and Hoffman et al. (1974) first reported in-situ observations of the polar wind on Explorer 31 and ISIS 2. On ISIS-2, Hoffman and Dodson (1980) inferred the presence of H^+ and He^+ polar wind at 1400 km altitude from the relative angles of arrival between the observed H^+ , He^+ , and O^+ ions, by assuming the O^+ ions to be stationary. The inferred H^+ ion velocity was in the range of $0.5-4 \text{ km s}^{-1}$ and larger than the corresponding He^+ velocity, consistent with classical polar wind theory prediction.

A few years later, Nagai et al. (1984) observed cold ($<1 \text{ eV}$ temperature) H^+ and He^+ polar wind ions that had a Mach number of 2.6–5.1 in the nightside polar cap near $2 R_E$ altitude on DE-1 during a large substorm. This study confirmed the supersonic nature of the polar wind at high altitudes, and motivated the survey of Chandler et al. (1991) using DE-1 data and that of Abe et al. (1993a, 2004) using Akebono data.

The survey of Chandler et al. (1991) covered the period from 1981 to 1983, near the maximum of Solar Cycle (SC) 21, and the altitude range of 1000–4000 km. It examined the altitude, seasonal, and magnetic-activity dependences of the polar wind and found the observed velocity profile to correlate with the solar $F_{10.7}$ flux.

The survey of Abe et al. (1993a, 2004) covered the period from 1989 to 1998, from SC 22 maximum to SC 23 maximum, and the altitude range of 1000–10,000 km. The initial survey (Abe et al., 1993a) covered the 1990–1992 period and focused on the altitude, local time, and mass dependences of the polar wind velocity, and the follow-on survey (Abe et al., 2004) covered the full 1989–1998 data period and focused on the solar activity and seasonal dependences of the polar wind. The initial survey found the observed ion velocity of all species to be highly variable, and the O^+ polar wind ions above 5000 km to have upward velocity up to 4 km s^{-1} and standard deviation of comparable magnitude. This suggested significant upward O^+ polar wind flow above this altitude most but not necessarily all the time, contrary to classical polar wind theory predictions, and motivated the interest on the O^+ component of the polar wind in the subsequent studies of Chandler (1995) and of Su et al. (1998).

Chandler (1995) reported regions of downward moving O^+ ions below 4000 km on DE-1 during southward interplanetary magnetic field (IMF), and interpreted these ions as low-energy O^+ ions originating from the cusp or cleft ion fountain that were undergoing anti-sunward convection and falling back into the ionosphere due to the fact that they were not sufficiently energetic to overcome gravitation. Su et al. (1998) surveyed the characteristics of H^+ , He^+ , and

O⁺ polar wind ions on POLAR at both 5000 km and 8 R_E altitude over the polar cap, and found the averaged H⁺ and O⁺ velocities to be ~45 and ~27 km s⁻¹, respectively, at 8 R_E altitude. As will be discussed in Section 3 and 4 below, the large velocities reflect the continuing acceleration of the polar wind at very high altitudes due to a number of mechanisms.

In addition to the polar wind, suprathermal and energetic ion outflows have been observed at high latitude. Yau and André (1997) classified the variety of outflows in the polar ionosphere into two categories: bulk ion flows with energies up to a few eV, such as the polar wind and auroral bulk upflow, and energetic ion outflows such as upward ion beams and conics, in which a portion of the ion population is accelerated to much higher energies, and upwelling ions in the cleft, which have typical energies up to a few tens of eV and characteristic temperatures of a few eV (Pollock et al., 1990).

It is important to note that the various types of outflow populations in the polar ionosphere are sometimes mixed due to horizontal plasma transport, and that ion energization processes can accelerate the polar wind into an energetic ion outflow population at auroral latitudes or in the polar cap. In particular, upwelling ions (UWI) originating from the cusp or the cleft can be transported into the polar cap. Under southward IMF conditions when convection across the polar cap is predominantly anti-sunward, the UWI can appear as a “cleft ion fountain (CIF)” in the polar cap, where they may be present at lower apparent temperatures than in the cleft due to velocity filtering effects (Horwitz and Lockwood, 1985), and contribute to the thermal ion population – and become a part of the ambipolar outflow.

Auroral bulk upflows are another important contributor of low-energy O⁺ ions to the polar wind ion population in the polar cap. Different types of upflow that reach velocities of ~1–2 km s⁻¹ below 1500 km altitude are often observed in the topside ionosphere during active times (Wahlund et al., 1992, Ogawa et al., 2000): thermal flow that is associated with enhanced ion temperature, strong perpendicular electric field, and low electron density, non-thermal flow that is associated with the auroral arc and enhanced electron temperature, and upflow in the dayside cusp that is accompanied by significant ion temperature anisotropy, electron temperature increase, and electron density enhancement.

Observationally, it is often not possible to definitively distinguish between thermal-energy ions that originate from different sources in the high-altitude polar ionosphere: the CIF, auroral bulk upflows, and “classical” polar wind from the topside ionosphere at polar-cap or auroral latitudes. An attempt is often made in statistical surveys to empirically separate the UWI and CIF from the polar wind and other thermal-energy ion populations based on specific attributes of individual data samples, such as their data sampling location (invariant latitude and MLT) and ion temperature. However, it is not possible to separate “classical” polar wind ions originating from the topside ionosphere at or below polar-cap latitudes from other sources of thermal-energy ions such as auroral bulk upflows, because of their similar energy and temperature characteristics in the high-altitude polar cap.

In this review, we use the term “polar wind” to refer to the ambipolar outflow of thermal ions on or near open magnetic field lines in the polar ionosphere, as a result of acceleration of the ambient ions primarily by ambipolar electric fields, recognizing that the latter may be due to pressure gradient, charge separation, or kinetic effects of photoelectrons, etc, and that other mechanisms in addition to ambipolar electric field may contribute to the ion acceleration. We also note that at high latitude, various thermal-energy ion populations including auroral bulk upflows typically drift into and out of different regions of the high-latitude ionosphere at different times, depending on the time-dependent convection electric field, and continually

change their velocity characteristics in response to local pressure gradient and other forces, as well as their geophysical location and identity as they do so. For simplicity we refer to all thermal ion flow populations at high latitude collectively as the “polar wind”.

2. Theoretical Predictions

In the presence of the Earth’s gravitation, an ambipolar electric field (E_{\parallel}) develops in the polar wind, as the ion is much more massive and experiences a much larger gravitational force compared with the electron, and the spatial separation between the two produces a polarization electric field in the vertical direction that acts to accelerate the ion in the upward magnetic field direction. An ambipolar field also develops in the presence of an anisotropic particle distribution, in order to maintain charge neutrality along the magnetic field line. In general, “classical” polar wind models differ in their detailed treatment of the boundary conditions that determine the characteristics of the ambipolar electric field, and the effects of the field on the dynamics of the polar wind ion flow.

The early polar wind models were focused on the “classical” polar wind, in which the ambient plasma pressure gradient and the ambipolar (polarization) electric field are the only sources of acceleration for the polar wind ions and result in a steady-state and current-free flow of quasi-neutral plasma along the field line, i.e. $\sum_i n_i q_i = 0$ and $\sum_i n_i q_i u_i = 0$ where n_i and q_i

denote the density and charge of polar wind species i , and u_i denotes its field-aligned velocity. In general, these “classical” polar wind models do not take into consideration any of the “non-classical” ion acceleration mechanisms, which are included in the “non-classical” polar wind models that will be discussed later in this section.

These early polar wind models were based on one of two approaches: the fluid approach and the collisionless kinetic approach. The two approaches are remarkably complementary to each other. The former is based on the macroscopic velocity moments of the polar wind ions and electrons, and includes the steady-state hydrodynamics models of Banks and Holzer (1969) and Marubashi (1970), and the hydromagnetic and generalized transport equations-based models of Schunk and co-workers (cf. Raitt and Schunk, 1983, and references therein). The latter is based on the kinetic treatment of the detailed velocity distributions themselves in the collisionless altitude regime, and includes the “evaporative theory” model of Dessler and Michel (1969) and the collision-less kinetic model of Lemaire and Scherer (1971, 1972a, 1972b). See Ganguli (1996) and other papers in this issue for excellent and comprehensive reviews of both categories of models.

These early models were followed by one-dimensional (1D) time-dependent fluid models and 3-dimensional (3D) steady-state or time-dependent generalized fluid (transport equations-based) models (Schunk and Sojka, 1997; Demars and Schunk, 2002), as well as “collisional” kinetic models that take into account Coulomb collisions, “hybrid” models that treat some plasma species kinetically and the other species as fluids (e.g. Demars and Schunk, 1991, 1992; Su et al., 1998b; in which such models were labeled as “semi-kinetic” models), and “semi-kinetic” models that combine the kinetic approach for the collisionless altitude regime with the moments-based approach for the collision-dominated regime (e.g. Lie-Svendson and Rees, 1996). A number of these more recent models may be considered as “non-classical” models in that they include a variety of “non-classical” mechanisms such as wave particle interaction and escaping atmospheric photoelectrons in their treatment of polar wind ion acceleration.

2.1 Collisionless Kinetic Model Predictions

In kinetic polar wind models, the velocity phase space function of a polar wind species is described by the Boltzmann equation. Under gyrotropic approximation,

$$[1] \quad \frac{df}{dt} = \frac{\partial f}{\partial t} + v_{\parallel} \frac{\partial f}{\partial z} - \left(g - \frac{qE_{\parallel}}{m} \right) \frac{\partial f}{\partial v_{\parallel}} - \frac{v_{\perp}^2}{2B} \frac{dB}{dz} \left(\frac{\partial f}{\partial v_{\parallel}} - \frac{v_{\parallel}}{v_{\perp}} \frac{\partial f}{\partial v_{\perp}} \right) = \left(\frac{\delta f}{\delta t} \right)_c$$

where $f = f_i(z, t, v_{\parallel}, v_{\perp})$ is the particle velocity phase space of species i at position z along the field line, time t , and parallel and perpendicular velocity components v_{\parallel} and v_{\perp} , and the species subscript i has been omitted for clarity. The collision term $(\delta f_i / \delta t)_c$ is a differential-integral function of the velocity distribution functions of all species.

In collisionless kinetic models, the collision term $(\delta f_i / \delta t)_c$ is neglected and the Boltzmann equation reduces to the Vlasov equation or the collisionless Boltzmann equation. In the steady state, Liouville's theorem applies, and the evolution of the velocity distribution of each polar wind species along the field line is given by: $f(\mathbf{r}, \mathbf{v}) = f(\mathbf{r}_0, \mathbf{v}_0)$, $\xi = mv^2 / 2 + q\Phi_E(\mathbf{r}) + m\Phi_G(\mathbf{r}) = mv_0^2 / 2 + q\Phi_E(\mathbf{r}_0) + m\Phi_G(\mathbf{r}_0)$, and $\mu = mv_{\perp}^2 / B = mv_{0\perp}^2 / B_0$, where μ and ξ are the particle magnetic moment and total energy, Φ_E and Φ_G are the electric and gravitational potentials, and the subscript 0 denotes the reference altitude. The distribution of Φ_E is governed by the conditions of quasi-neutrality and current-free flow in the polar wind, and the flux of each polar wind species along the field line is proportional to B .

In the model of Lemaire and Scherer (1972a), a monotonic potential energy altitude profile was assumed for each particle species. The particles are subdivided into four trajectory types: ballistic, escaping, trapped, and incoming. All four trajectory types are allowed for particles such as O^+ ions that have positive (electric plus gravitational) potential energies above the baropause, but only escaping and incoming trajectories are possible for particles such as H^+ ions that have monotonically decreasing potential energies. Lemaire and Scherer (1972a) defined the baropause at 2000 km in their model, as the altitude above which the Knudsen number K_n (the ratio between the electron Coulomb collision mean free path and density scale height) exceeds unity. Note that the terms "baropause" and "exobase" are sometimes used interchangeably in the literature, and that the term "exobase" usually refers to the transition altitude at which the neutral collision mean free path equals the atmospheric scale height (see e.g. Schunk and Nagy, (2000)), and this altitude is typically about 500 km.

Lemaire and Scherer (1971) considered several models of different ion composition and particle trajectory types. Figure 1 shows the calculated electric field and electric potential as a function of altitude in their most realistic model, which consisted of H^+ , O^+ and electrons, and included ballistic, escaping and trapped particles in a dipole magnetic field. The electric field decreased from about 0.5 $\mu\text{V/m}$ at the baropause to less than 0.02 $\mu\text{V/m}$ at high altitudes. The potential difference between 2000 and 20,000 km was about 1.7 V, and resulted in the acceleration of the H^+ ions to above supersonic velocities, and the transition from O^+ to H^+ as the major ion species above 5500 km. The corresponding acceleration of O^+ was much smaller.

2.2 Moments-Based Model Predictions

Hydrodynamic and generalized fluid polar wind models derive continuity equations for the moments of the distribution functions by taking the velocity moments of the Boltzmann or Vlasov equation, and seek to solve these continuity equations to obtain the spatial and/or temporal distributions of plasma density, velocity, temperature, or other higher moments of each species. In the generalized fluid models, the collision terms are retained, and the number of coupled equations to be solved for each species depends on the moment approximation used. In both types of models, the system of continuity, momentum, energy, and/or higher order moment equations are used to describe the density, momentum, energy, and/or other moments of the polar wind along the field line. The next higher-order moment is specified based on imposed boundary conditions in terms of the lower-order moments, as a means to close the system of equations.

The hydrodynamic models of Banks and Holzer (1968) and Marubashi (1970) was focused on the supersonic nature of the polar wind flow, and included only the steady-state continuity and momentum equations of the H^+ -electron plasma; to close these equations the system was assumed to be isothermal. The density and velocity profiles obtained predicted light H^+ ion outflows along the field line at supersonic speeds above the H^+ - O^+ collision region due to the presence of the ambipolar electric field.

The model of Holzer et al. (1971) was focused on the possible effects of ion temperature anisotropies on the polar wind. This model removed the isothermal assumption and included the energy equations for the parallel and perpendicular temperatures. The system of equations was closed by specifying the heat flux terms in terms of collision energy transfer. Both heat conduction and viscosity were found to be relatively unimportant in H^+ polar wind transport.

The model of Raitt et al. (1975, 1977) examined the effects of convection, and the resulting ion-neutral collisions and (frictional) ion heating. In this model, the heating increased the plasma pressure gradient between the ionosphere and the magnetosphere, which enhanced the polar wind flux, but it also reduced the F-region O^+ density, which reduced H^+ production. Overall, convection increased the H^+ and O^+ densities and temperatures and decreased the H^+ velocity.

The model of Schunk and Walker (1970a, b) studied the effects of thermal diffusion and diffusion thermal heat flow. Downward thermal diffusion was found to reduce the upward flow of H^+ , increasing the ion density and reducing its temperature. Diffusion thermal heat flow would occur in the presence of relative drifts between ion species, either assisting or opposing thermal conduction depending on the direction of the relative drift, and acting to cool the topside H^+ significantly (by more than 500 K above 900 km (Schunk et al. 1978)).

The predicted characteristics of He^+ in general differ from those of H^+ . In the model of Banks and Holzer (1969), helium was sufficiently light to acquire a non-negligible flow velocity (> 1 km/s) above the collision-dominated altitudes. In the model of Raitt et al. (1978), which covered the 200-2000 km altitude range, the limiting He^+ escape flux was found to vary with the neutral atmospheric helium density but was otherwise insensitive to a wide range of peak O^+ density, H^+ flow velocity, or convection electric field.

2.3 Generalized Transport-Equations Based Model Predictions

In generalized-transport-equation based models, the lower-order moments are assumed to be independent of the higher-order expansion of the velocity distributions to first order, and the system of equations is closed by truncation of the expansion series. In the steady-state 13-moment model of Schunk and Watkins (1981, 1982), the 13 moments in the system of equations

were reduced to 5 moments for each plasma species in the gyrotropic approximation: density, parallel velocity, parallel and perpendicular temperatures, and heat flow; $T = (T_{\parallel} + 2T_{\perp})/3$. This model consisted of H^+ , O^+ and electrons and extended from 1200 to 12,000 km altitude, and was used to study both ion and electron temperature anisotropies. In this model, the parallel H^+ ion temperature at high altitudes was greater than the perpendicular temperature ($T_{H\parallel} > T_{H\perp}$). At low altitudes, collisions dominated and temperature anisotropy was absent up to 2500 km. The electron temperature anisotropy (parallel to perpendicular temperature ratio, $T_{e\parallel} / T_{e\perp}$) was less than unity, due to the higher electron temperature at the upper boundary than at the lower boundary; Ganguli and Palmadesso (1987) showed that in such models, the direction of electron temperature anisotropy depends on the upper boundary conditions.

In the corresponding 16-moment models of Ganguli et al. (1987) and Demars and Schunk (1989), which used the same input conditions as in the 13-moment model of Schunk and Watkins (1982), the parallel and perpendicular heat flows were treated independently: $q = (q_{\parallel} + 2q_{\perp})/3$ where q_{\parallel} and q_{\perp} are the parallel and perpendicular heat flows, respectively. The ion and electron anisotropies were found to be similar to those in the 13-moment model. $T_{H\parallel} > T_{H\perp}$ and $T_{e\parallel} < T_{e\perp}$ above the collision-dominated region. In addition, the H^+ heat flux was predicted to be upward. The predicted velocity was as large as 16–20 km/s and corresponded to a Mach number in the range of ~ 2.5 –4 at high altitude.

As discussed in Yasseen and Retterer (1991), the subsonic to supersonic transition altitude for the H^+ polar wind – the sonic point – is typically near or below 1500 km. This point corresponds to a singularity in a system of moment equations, making its numerical solution intrinsically difficult to obtain in moment-based polar wind models. In both the 13-moment model of Schunk and Watkins (1981, 1982) and the 16-moment models of Ganguli et al. (1987) and Demars and Schunk (1989), a lower boundary of ~ 1500 km altitude was assumed and the polar wind velocity was either subsonic or supersonic throughout the altitude range of the model, depending on the assumed boundary conditions. In contrast, the polar wind velocity in the 13-moment model of Mitchell and Palmadesso (1983) and the 16-moment model of Blelly and Schunk (1993) transitioned from subsonic to supersonic.

As in moments-based models, the predicted characteristics of He^+ in general differ from those of H^+ . In the 16-moment model of Demars and Schunk (1994), which included H^+ , He^+ , and O^+ as major species and a number of other ions as minor species, both supersonic and subsonic He^+ flows were considered. In the supersonic case, the He^+ density decreased with increasing altitude more rapidly than H^+ density, and the heat flow was positive and confined to low altitudes. In the subsonic case, He^+ was the dominant ion at high altitudes, and both the parallel and perpendicular temperatures were significantly higher than for the supersonic case, suggesting that adiabatic cooling may be less important in determining the energy balance. Both the parallel and perpendicular components of He^+ heat flow were negative and remained large to high altitudes.

2.4 Collisional Kinetic Model Predictions

In the case of a non-thermal (highly non-Maxwellian) distribution, the higher-energy particles may not be fully thermalized because of the strong velocity dependence of the Coulomb collision frequency ($f_c \propto v^{-3}$, where f_c is the collision frequency and v is the relative velocity). In such a case, the Coulomb collision integral in the moment equations may not be an accurate

approximation and moment-based models may become inaccurate. Collisional kinetic models are more applicable to describe the effects of Coulomb collisions on such a distribution (Barghouthi et al., 2001). In such models, the Boltzmann equation is often cast in the form of the Fokker-Planck equation, and the effect of collisions incorporated into a Coulomb collision operator for the $(\delta f_i / \delta t)_c$ term, by assuming a simple collision model. For example, Barakat et al. (1991) used the Maxwell molecule collision model, which is strictly speaking applicable to non-resonant ion-neutral collisions only and may not be appropriate for $H^+ - O^+$ Coulomb collisions, and Wilson (1992) used a randomized binary $O^+ - O^+$ self-collision model.

Barakat et al. (1995) and Lie-Svendsen and Rees (1996) studied the effects of Coulomb collisions on H^+ ions as a minor species in the steady state, using Monte-Carlo test particle calculations which assumed a pre-defined electric field, a drifting Maxwellian for the background O^+ ions, and negligible self-collisions between the H^+ ions. The study of Lie-Svendsen and Rees (1996) was performed for the collisional to collisionless transition altitude region in a semi-kinetic model that also covers the collisional altitude regime below and the collisionless altitude regime above. Both of these studies predicted the evolution of the minor H^+ ions from a thermal Maxwellian distribution to a double-humped distribution at 1000-2000 km altitude, due to the velocity dependence of the Coulomb collision mean free path and the non-local nature of the polar wind flow. Figure 2 shows that the H^+ velocity distribution exhibits a secondary peak at 1280 km altitude, and evolves into a suprathermal tail at higher altitudes, as more or more lowest-energy ions are overcome by the gradually increasing potential barrier. Recently, Pierrard and Lemaire (1998) obtained qualitatively similar results using a spectral method based on the Legendre and speed polynomials.

2.5 Hybrid Model Predictions

The linearized Fokker-Planck equation is valid only for a minor species under the assumption of negligible self-collisions. For a major ion species in a collisional kinetic polar wind model, a nonlinear solution to the Fokker-Planck equation is required. To our knowledge, such a nonlinear solution does not yet exist. However, Tam et al. (1995a) developed a hybrid model which treated the nonlinear Coulomb interactions of photoelectrons in the presence of H^+ and O^+ ions and thermal electrons. They considered the energy and momentum transfer of the isotropic thermal electrons due to Coulomb collisions in the fluid part of their model, and treated the photoelectrons as test particles in the kinetic part of the model. Because of the self-collisions among the H^+ ions and the resulting collisional relaxation of the H^+ velocity distribution to a drifting Maxwellian, the distribution in their model did not evolve into a double-humped distribution until a much higher altitude, compared with the linearized collisional kinetic model of Barakat et al. (1995) (cf. Figure 2 in Section 2.4 above).

2.6 Non-classical Polar Wind Model Predictions

In classical polar wind models, the O^+ ions are usually considered too heavy to overcome their gravitational potential barrier and assumed to be confined to hydrostatic equilibrium. Consequently, both the escape flux of O^+ and its density above the topside ionosphere (above ~ 1500 km altitude) are expected to be negligibly small. In contrast, significant acceleration of O^+ and other heavy ions is theoretically possible in non-classical polar wind models, in which a number of “non-classical” polar wind ion acceleration mechanisms may be present. These

mechanisms include external ion heating, wave particle interaction (WPI), centrifugal acceleration, strong ionospheric convection, enhanced electron temperature, enhanced ion temperature, and escaping atmospheric photoelectrons, or other mechanisms that are not yet identified.

Gombosi et al. (1985) considered external ion heating in their hydrodynamic model, and found the O^+ flow to become supersonic in response to strong external heating. Gombosi and Killeen (1987) considered ion-neutral collision frictional heating, and found that a short duration of horizontal frictional heating due to ion-neutral collisions can lead to near-sonic upward flow of O^+ (~ 2 km/s) along the field line.

Wave particle interactions (WPI) constitute a special form of ion heating. Perpendicular ion heating resulting from WPI leads to ion acceleration in the upward direction because of the magnetic mirror (∇B) force in the Earth's divergent dipole magnetic field. Barakat and Barghouthi (1994) considered the perpendicular velocity diffusion of polar wind O^+ ions due to WPI in their steady-state test-particle calculations, and found the WPI to enhance the O^+ escape flux by as much as five orders of magnitude.

Cladis (1986) was the first to show that strong $E \times B$ convection in regions of curved magnetic field, for example near the high-altitude cusp, can produce significant parallel ion acceleration in the polar ionosphere. Horwitz et al. (1994) and Ho et al. (1997) referred to such ion acceleration as "centrifugal acceleration" in the convecting plasma frame of reference, and examined this effect on polar wind O^+ ions using 1-dimensional particle-in-cell (PIC) simulations. Both studies found the high-altitude O^+ escape flux to increase by two orders of magnitude as the convection electric field at ionospheric altitudes increased from 0 to 100 mV/m. The centrifugal acceleration of polar wind ions is effective mainly at high (above a few R_E) altitudes, where the local magnetic field curvature increases with increasing altitude.

At low altitudes where the effect of centrifugal acceleration is negligible, Schunk and coworkers demonstrated that convection is important as a means of transporting energized O^+ ions to the polar wind. Schunk and Sojka (1989; 1997) used their 3-dimensional time-dependent models of the "generalized" polar wind, in which flux tubes containing energized O^+ ions convect into the polar wind region, while Barakat and Schunk (2001) used particle-in-cell (PIC) simulations in which only a single convecting flux tube is considered. Both studies demonstrated clearly that observationally it is not always possible to unambiguously separate an energized "non-polar-wind" O^+ ion such as a low-energy "cleft ion fountain" ion that has convected into a polar wind flux tube from an energized "polar-wind" O^+ ion that is accelerated locally by "non-classical" polar-wind ion acceleration mechanisms.

In a parametric study of the effect of electron temperature on O^+ polar wind flow, Barakat and Schunk (1983) assumed the electric field to be approximately proportional to the electron temperature ($E_{\parallel} \propto -kT_e \nabla n_e$ where T_e is electron temperature and n_e is electron density), and found the O^+ velocity at high altitudes to increase from <1 km/s to a few km/s, as the electron temperature increased from a few 1000 K to 10,000 K. Based on this study, Demars et al. (1996) suggested that the effect of enhanced electron temperature is more important on the O^+ escape flux compared with that of centrifugal acceleration.

Using a similar model to study the effect of ion heating on O^+ flow, Li et al. (1988) found that an increase in ion temperature at the exobase from 3000 K to 10,000 K would result in an increase of five orders of magnitude in the O^+ flux and that the effect of ion heating on the O^+ flux would dominate over that of electron heating at ion temperatures of ~ 3 eV ($\sim 30,000$ K). Since the ion temperature at the exobase is typically about 1000-3000 K, the effect of electron

temperature is probably more important than that of ion temperature in most if not all polar wind conditions.

Barakat and Schunk (1984) studied the effect of hot magnetospheric electrons, by treating them as an isotropic hot electron fluid that is coexisting with an isotropic cold ionospheric electron fluid. They found that for large hot-to-cold electron temperature or hot-to-total electron density ratio, a double layer (discontinuity of the electric field) would develop and reflect the cold ionospheric electrons, and the magnetospheric electrons would reduce the potential barrier for the O^+ ions and enhance their escape.

Historically, Axford (1968) postulated the enhancement of the ambipolar electric field by escaping atmospheric electrons in his classic paper on the polar wind and the terrestrial helium budget, and speculated on the effects of the enhanced electric field on the O^+ ions. In the presence of escaping atmospheric photoelectrons, Coulomb collisions between the photoelectrons and the thermal polar wind electrons are expected to result in energy transfer between the two populations. The change (increase) in the thermal electron temperature will increase the ambipolar electric field and the ion flow velocity. Furthermore, the strong ($\propto v^4$) velocity dependence of Coulomb collision mean free path results in the relative lack of collisional thermalization of the higher-energy electrons compared with the lower-energy electrons, and the gradual formation of a temperature anisotropy and a non-thermal tail in the electron distribution at higher altitudes. The resulting additional charge separation (polarization) force acting on the polar wind ions can in principle enhance the ambipolar electric field and accelerate the ions further to higher velocities and increase the O^+ escape flux. In their collisionless kinetic model, Lemaire (1972) found that the ambipolar electric field, the ion velocity, and the thermal electron temperature and flux all increase with the photoelectron flux if the latter exceeds the escaping thermal electron flux.

Yasseen et al. (1989) used a global collisional hybrid model to study the effects of Coulomb collisions between photoelectrons and thermal electrons in the polar wind, by assuming a thermal electron distribution based on fluid simulation and using electric field observed on DE-1. They found their steady-state solutions for the photoelectron distributions to be consistent with the observed downward electron distribution on DE-2. Tam et al. (1995b) used a 16-moment model to generate altitude profiles of the electric field and thermal particle moments, which were used as background profiles for test photoelectrons in a non-local kinetic collisional calculation. These authors found the heat flux of the test photoelectrons to be much larger than that of the background thermal electrons, and argued that the presence of photoelectrons would significantly increase the electric field. Tam et al. (1995a, 1998) used a self-consistent hybrid model (without the 16-moment equations) to investigate the heat flux of the photoelectrons and thermal electrons, and the evolution of the H^+ and O^+ ion velocity distributions and the thermal electron energy and momentum due to Coulomb collisions, including self-collisions. Their simulations predicted a double hump in the H^+ velocity distribution at much higher altitudes than that in Barakat et al. (1995) and Pierrard and Lemaire (1998); presumably the self-collisions act to thermalize the distribution to drifting Maxwellian. It is important to note that the double-humped H^+ velocity distribution is a unique and basic feature predicted only by the collisional kinetic models, and represents a fundamental difference between distributions from fluid and kinetic models.

From their self-consistent hybrid model, Tam et al. (1998) found that a photoelectron concentration of 0.05–0.1% increased the potential drop on the dayside from its nightside value of 2V to a value of 5 to 12 V, and resulted in a significant upward heat flux that dominated over

the thermal electron heat flux. Figure 3 shows the potential drop and the corresponding O^+ velocity for the nightside and for 3 different photoelectron concentrations on the dayside.

2.7 Comparison of Model Predictions

As demonstrated in the “simple kinetic” model of Holzer et al. (1971) and the comparisons between moment-based and corresponding kinetic models in Demars and Schunk (1991), predictions from comparable fluid and kinetic polar wind models are generally in agreement, insofar as predicted polar wind properties such as ion density and velocity; see also the reviews of Schunk (2006) and Tam et al. (2006). Table 1 below summarizes the predictions of the different polar wind models discussed in this section, both quantitative and qualitative, that will be compared with observations later in the Section 4. A detailed comparison of the quantitative predictions of the different models is beyond the scope of this review, and may not be very meaningful in many cases, where the quantitative details of a specific prediction may depend strongly on the assumed background ionospheric conditions

3. Observations

3.1 Overview

For many years after the theoretical prediction of the polar wind, only indirect evidence for its presence was available: the existence of the light ion trough (Raitt and Dorling, 1976) and the latitudinal variation of the $H^+ - O^+$ ion transport height (Titheridge, 1976). The most successful of the early polar wind measurements were those of Hoffman and co-workers from Explorer 31 (Hoffman 1970) and ISIS-2 (Hoffman and Dobson 1980). Over the past three decades, polar wind observations have been made using ion composition and other thermal plasma instruments on a number of polar-orbiting satellites, including ISIS-2, DE-1, Akebono, and POLAR. These observations covered different altitude ranges and spanned different solar cycles (SC 20 to 23). From these observations, a coherent, though incomplete, picture of the characteristics of the polar wind and their dependence on geophysical location (altitude, invariant latitude, and magnetic local time) and geomagnetic and solar activity levels is starting to emerge.

In the following subsections (Section 3.2 to 3.5), we will review important observations from the different satellites in chronological sequence, in order to gain some insight into how the in-situ polar wind measurements have evolved as our capabilities in thermal plasma instrumentation have improved and instrument flight opportunities have arisen. Our review will focus predominantly on in-situ ion measurements, since relevant polar wind electron measurements are more limited in the literature. Figure 4 depicts schematically the observed polar wind flow in the polar ionosphere, where the polar wind is regularly observed at all local times and latitudes and the light H^+ polar wind ions typically attain appreciable speeds (≥ 1 km/s) at ~ 1000 km altitude in the topside ionosphere. The direction, length and width of the arrows in the figure denote the flow direction, speed, and temperature, respectively, of the polar wind ions. As the polar wind ions flow upward along “open” magnetic field lines and undergo generally anti-sunward convection in the polar cap and dayside cusp poleward of the plasmasphere, they increase in both drift speed and temperature. The arrows of different colors (or shades) depict the presence of different ion mass species in the polar wind.

To provide a framework with which to relate observations in different altitude ranges and in different phases of the 11-year solar cycle from the different satellites, Figure 5 shows (a) the mean, maximum and minimum solar radio flux, $F_{10.7}$, in each 27-day solar rotation in the period from 1965 to 2005 in units of solar radio flux ($1 \text{ sfu} = 10^{-22} \text{ W m}^{-2} \text{ Hz}^{-1}$), and (b) the altitude and time spans of each set of polar wind observations in this period. This period spans Solar Cycle (SC) 20 to 23, including the SC 20 maximum in 1969 and the SC 23 maximum in 2000. The $F_{10.7}$ index is used as an index of solar electromagnetic radiation energy input (EUV flux). Near solar maximum, the $F_{10.7}$ index spans a wide range within a solar rotation. This implies that the level of solar EUV flux varies significantly over a solar rotation. Occasionally on days of large solar flare events, the daily $F_{10.7}$ value exceeds 350 and sometimes reaches 600 or greater; we have excluded daily values exceeding 350 in determining the maximum $F_{10.7}$ value in a solar rotation.

The polar wind observations from the different satellites in Figure 5b span a wide range of altitudes, from about 1000 km to $\sim 50,500$ km ($8 R_E$) altitude. In particular, the Explorer-31, ISIS-2 and low-altitude DE-1 observations were below 4,000 km. The Akebono observations spanned the range from 1000 km to 10,000 km. The POLAR observations were primarily near its perigee (5000 km) and apogee ($\sim 50,500$ km) but included data down to $\sim 22,000$ km. For convenience, we refer to observations below 4000 km as low-altitude observations, those above 10,000 km as high-altitude observations, and those in between as mid-altitude observations, recognizing that both the ion-exosphere upper boundary (<3000 km) and the source region of upwelling ions (~ 2500 – 3500 km) lie within our “low-altitude” region and that the so-called auroral “parallel acceleration” region (~ 5000 – $10,000$ km) falls within our “mid-altitude” region.

3.2 Explorer and ISIS-2 Observations

Hoffman and Dobson (1980) and Brinton et al. (1971) reported high-latitude ($>71.6^\circ$ invariant) ion density altitude profiles derived from ion mass spectrometer measurements between 500 and 3000 km altitude on Explorer 31 and 32, respectively. In contrast to the mid-latitude profiles, in which the O^+ density dominated below and the H^+ density dominated above the “crossover” altitude near 1000 km, these high-latitude profiles featured (a) an abrupt change in the O^+ scale height at about 1400 km, (b) dominant O^+ density (over H^+) at all altitudes up to 3000 km or higher, and (c) a lower total ion density in comparison with the mid-latitude. These features were interpreted as evidence of an upward bulk flow of H^+ ions, and indicative of the presence of the H^+ polar wind.

In the ISIS-2 measurements, the ion mass spectrometer measured incident ion fluxes as a function of the spacecraft spin angle, and the instrument was biased by a negative 6 V potential, to allow sampling of thermal ions at all energies in the presence of the spacecraft potential and spacecraft potential variations (~ 1 eV). The relative angles of arrival between H^+ , He^+ , and O^+ ions were used to infer the upward field-aligned flow of H^+ and He^+ . At 1400 km altitude, the observed (inferred) H^+ velocity was in the range of 0.5–4 km/s. The corresponding He^+ velocity was generally smaller. Because of the limited altitude precision on ISIS-2, it was not possible to determine the corresponding O^+ velocity; instead, O^+ was assumed to be stationary and its velocity was assumed to be zero.

Figure 6 shows the measured H^+ and O^+ polar wind densities and upward H^+ fluxes and velocities on ISIS-2, in the summer and winter solstice, respectively, of 1971-1972, in the early declining phase of the solar cycle. The latitude dependences of the H^+ density and velocity were anti-correlated. This is indicative of a constant upward flux and a condition of limiting flux. In

the summer, the averaged H^+ flux above 60° invariant was $\sim 7 \times 10^7 \text{ cm}^{-2} \text{ s}^{-1}$. The velocity peaked at about 2.5 km s^{-1} . In the winter, the observed polar wind was more variable. The flux peaked at its summer value at 75° – 85° invariant but dipped to $3 \times 10^7 \text{ cm}^{-2} \text{ s}^{-1}$ at the pole. The velocity peaked at 4 km s^{-1} . Assuming an ion temperature of 0.1 eV or greater, the flow was subsonic at all times in the summer and at most times in the winter.

In contrast to H^+ , He^+ exhibited a somewhat opposite seasonal dependence. The observed He^+ flux peaked at winter, at ~ 1 – $2 \times 10^7 \text{ cm}^{-2} \text{ s}^{-1}$, compared with the summer solstice value of $1.5 \times 10^6 \text{ cm}^{-2} \text{ s}^{-1}$, corresponding to a winter-to-summer ratio of about 10.

3.3 DE-1 Observation

The polar wind measurements on DE-1 covered the period from October 1981 to April 1983, in the early declining phase of Solar Cycle 21, and spanned primarily the altitude range from 1000 to 4000 km (Chandler et al., 1991) and episodically the $2 R_E$ altitude region (Nagai et al., 1984). These measurements were made using the retarding ion mass spectrometer (RIMS), by sampling ions in the spacecraft spin (and orbit) plane.

Over approximately 33 hours of the low-altitude data were analyzed, including 15 hours of high-latitude data, under the assumption of zero ion convection velocity in the spin plane. Because these data were all acquired at the zero retarding potential analyzer (RPA) voltage setting, it was in principle not possible to ascertain the relative contributions between the polar wind and other higher-energy ion populations in these measurements. However, since the analysis was restricted to invariant latitudes above 70° , the effects of both suprathermal ions of auroral or cusp origin and of convective electric fields are believed to be minimized.

The average flux of the observed H^+ polar wind exhibited a factor-of-3 seasonal variation, and ranged from $5 \times 10^7 \text{ cm}^{-2} \text{ s}^{-1}$ in the summer to $1.5 \times 10^8 \text{ cm}^{-2} \text{ s}^{-1}$ in spring. In comparison, the observed He^+ polar wind flux had a much larger (factor-of-20) variation and ranged from a minimum of $1 \times 10^6 \text{ cm}^{-2} \text{ s}^{-1}$ in the summer and a peak value of 2×10^7 in the winter.

The observed flux exhibited a variation of a factor of 3 over the range of Kp from 0 to 7–. The observed variations with both the 3-hr Kp and the daily Ap indices were considered insignificant compared with the standard deviations about the means. Despite limited data sampling in periods of high and low solar activity ($F_{10.7} > 200$ and $F_{10.7} < 100$, respectively) in the DE-1 data set, the spread of $F_{10.7}$ in the summer data was large enough to allow Chandler et al. to study the correlation between the observed polar wind flux and the value of $F_{10.7}$. However, no significant trend was found.

Figure 7 shows the averaged H^+ polar wind velocity observed on DE-1 as a function of altitude. Figure 7a compares the velocity at times of high and low solar flux ($F_{10.7} > 190$ and < 140), respectively. At times of low $F_{10.7}$, the average velocity increased with altitude, from about 3 – 4 km s^{-1} below 2000 km to $\sim 11 \text{ km s}^{-1}$ above 3000 km. In comparison, at times of high $F_{10.7}$, the acceleration (increase in velocity with altitude) occurs above 2000 km, and the velocity at 3000 km is about 8 km s^{-1} , i.e. about 30% smaller. The lower velocity at times of high solar $F_{10.7}$ is attributed to the higher solar output at these times, and the resulting higher neutral exospheric temperature, higher oxygen density, and lower hydrogen density, since the increased oxygen density and photo-ionization rate in turn result in more O^+ ions and the extension of the H^+ - O^+ friction to higher altitude.

Likewise, Figure 7b compares the velocity in the summer and winter, respectively. Above 2500 km, the velocity in the summer is about 30-70% higher than that in the winter. The velocity

in the fall (not shown) was between those for summer and winter. In contrast to the ISIS-2 observations at 1400 km altitude discussed in subsection 3.2 above, the velocity below 1500 km in the summer appeared to be larger and more variable than that in the winter.

On average, the velocity of He^+ was about 0.28 that of H^+ . Its altitude profile was similar to that of H^+ , as was its $F_{10.7}$ variation. However, compared with H^+ , its seasonal variation is much smaller in magnitude, the velocity in the summer being less than 20% lower than that in the winter.

Above 2000 km, the observed O^+ velocity ranged from -2 km s^{-1} (i.e. downward ion flow) to $+2 \text{ km s}^{-1}$ (upward ion flow) in most cases, and appeared to correlate with both the mean and the standard deviation of the H^+ velocity. The highest upward O^+ velocity was observed at times of maximum H^+ velocity mean and standard deviation. Chandler et al. (1995) attributed the apparent correlation to collisional interaction processes between H^+ and O^+ below 2000 km, and possibly other processes that affect the ambipolar electric field.

In the case of both H^+ and He^+ , the average ion velocities tended toward zero as the altitude decreased, and exhibited large statistical variations that increased with altitude.

O^+ was the dominant ion species in the polar wind up to the highest altitude (4000 km) in the studies of Chandler et al. (1991, 1995). The mean O^+ density was about 2000 cm^{-3} at 2000 km and had a scale height of $\sim 1500 \text{ km}$. H^+ and He^+ were minor ions, the H^+ and He^+ density was about 0.05 and 0.02 of the O^+ density, respectively, and had roughly the same altitude dependence as the O^+ . The O^+ density at times of high $F_{10.7}$ was about a factor of 2 larger than that of low $F_{10.7}$, but there was no significant variation in either the H^+ or the He^+ density with $F_{10.7}$.

The densities of all three ion species exhibited significant seasonal variations. The O^+ density decreased from summer to winter, by a factor of about 1.5–3. At low altitude where density measurements were available, the H^+ and He^+ densities increased from summer to winter, by a factor of about 2 and 10, respectively. At higher altitudes, the larger positive spacecraft potential due to the decreased plasma density screened out the lowest-energy H^+ and He^+ ions and precluded the accurate determination of densities. Only lower limit estimates were available.

In a more detailed analysis using a more restrictive, Kp-dependent polar cap boundary, Chandler et al. (1995) examined the possible contributing effects of solar illumination, ion convection, geomagnetic activity, and IMF, on O^+ polar wind. They found that inside the polar cap below 3000 km, the O^+ velocity was on average near zero ($|v| < 100 \text{ m s}^{-1}$). Between 3000 and 4000 km, the velocity was on average $\leq 1 \text{ km s}^{-1}$ and downward, and its standard deviation was $\sim 2 \text{ km s}^{-1}$ and considerably larger than the magnitude of the average. This suggests that both upward and downward velocities were observed in comparable frequency and/or magnitude. Figure 8 shows the average velocity above 2500 km as a function of IMF B_z , and it clearly associates the average upward velocity with northward IMF and the average downward velocity with southward IMF.

Compared with the IMF, the contributing effects of solar illumination, ion convection, and geomagnetic activity on O^+ polar wind flow were not as pronounced. The average (downward) velocity in the sunlit polar cap ($\text{SZA} < 90^\circ$) was smaller in magnitude than that in the dark polar cap ($\text{SZA} > 90^\circ$), suggesting that photoelectrons may play a discernible though not overriding role in O^+ polar wind flow. At high levels of geomagnetic activity ($\text{Kp} > 3$), the velocity below 3000 km increased marginally upward from zero, and the velocity above was near zero. The difference was attributed to increased anti-sunward ion convection during active times, and the farther transport of ions across the polar cap. In other words, upward O^+ ions originating from a

certain location (altitude, invariant latitude, and MLT) on the dayside would fall back to their original altitude at a location of lower invariant latitude on the nightside.

Overall, Chandler et al. (1995) estimated the total O^+ ion down-flow and up-flow in the low-altitude (<4000 km) polar ionosphere ($\geq 60^\circ$ invariant) to be roughly 0 and 5.7×10^{25} ions s^{-1} during periods of northern IMF, and 1.0×10^{25} and 4.4×10^{25} ions s^{-1} during periods of southern IMF, respectively. This implies that averaged over all IMF conditions, the return flow is $\sim 10\%$ of the up-flow.

At high ($\sim 2 R_E$) altitude outside the plasmasphere, where the plasma density was typically below 10^3 cm^{-3} and the DE-1 spacecraft was often charged to a few volts positive, the lowest-energy polar wind ions were repelled by the spacecraft potential. Nagai et al. (1984) used a negative bias aperture in the DE-1 RIMS instrument to partially overcome the positive spacecraft potential, and successfully detected both H^+ and He^+ polar wind ions down to ~ 0 eV in a large substorm in the winter. The observed H^+ flux was fairly stable, and had a flow velocity of 16–25 km/s, a temperature of 0.12–0.2 eV, and an equivalent Mach number of 2.5–5.1 and normalized flux of $2.6 \times 10^8 \text{ cm}^{-2} \text{ s}^{-1}$ (at 1000 km). The observed He^+ flux was quite variable. The He^+/H^+ ratio varied between <0.01 and 1.

Near DE-1 apogee ($\sim 3.65 R_E$ altitude), higher-energy ion flows with peak energy of 10–20 eV in velocity phase space density and temperature of a few eV were often observed, which Gurgiolo and Burch (1982) interpreted as O^+ polar wind ions that were perpendicularly heated at lower altitude and convecting anti-sunward. However, Green and Waite (1985) argued that these were ions with 10 eV perpendicular and 1 eV parallel initial temperature originating from the dayside cusp, leaving open the question of whether these ion flows were steady-state O^+ polar wind ions.

The polar-cap electron density distribution is an important part of the polar wind equation. Persoon et al. (1983) derived the local electron density in the northern polar cap above 71.6° invariant over the altitude range of 7000 to 23,300 km, using the measured electric field spectrum from the plasma wave instrument (PWI) on DE-1 in the first five months of the mission, from September 1981 to February 1982 in the early declining phase of SC 21. In this altitude range of the polar cap, the electron plasma frequency is generally much smaller than the electron gyrofrequency. Therefore the measured upper cutoff frequency for the whistler mode is effectively equal to the electron plasma frequency. By identifying the cutoff frequency on the electric field spectrum, one can estimate the electron plasma frequency and the corresponding electron density, using the relation $n_e = (f_p / 9)^2$ where n_e is the electron density in cm^{-3} and f_p is the electron plasma frequency in kHz.

Persoon et al. (1983) analyzed over 80 2-hr spectrograms over the polar cap. The calculated electron density was found to vary over 1-2 orders of magnitude for a given altitude, but generally decrease with increasing altitude. Figure 9 is a log-log plot of the median value and quartiles of the electron density as a function of geocentric distance. The density ranged from $35.2 \pm 8.5 \text{ cm}^{-3}$ at 7000 km ($2.1 R_E$ geocentric) to $0.99 \pm 0.51 \text{ cm}^{-3}$ at 23,300 km altitude ($4.66 R_E$ geocentric), and followed a power law relationship with geocentric distance R and a power-law index of $\alpha = -3.85 \pm 0.32$, i.e. $n_e \propto R^\alpha$.

In comparison, assuming a steady-state polar wind ion flow and a negligible divergence in its perpendicular ion flux as well as its local production and loss, the continuity equation for the flow requires that $F_i = n_i v_i \propto 1/A \propto B \propto R^{-3}$, where F , n_i , and v_i are the flux, density, and velocity of polar wind i , and A and B are the flux tube area and magnetic field intensity at

geocentric distance R ; $B \propto R^{-3}$ in the dipole approximation. In the case of a single-species, singly-charged polar wind, $n_i = n_e$, and the polar wind ion velocity is expected to vary inversely with the product of the density and R^3 , i.e. $v_i \propto 1/(n_e R^3)$. Thus, the power law index of -3.85 suggests that the polar wind ion velocity increases approximately linearly with geocentric distance between 7000 km and 23,300 km altitude.

Persoon et al. (1983) compared their electron density profile on DE-1 above 7000 km with a profile derived from Alouette II and ISIS-1 topside sounder data below 3000 km. Below 1000 km, the Alouette/ISIS profile basically followed the diffusive equilibrium model profile. Above 1000 km, it appeared to transition to a slower density decrease with increasing altitude (i.e. smaller power law index magnitude), which is consistent with the transition of the H^+ polar wind from subsonic to supersonic speeds in the 1000 – 1500 km altitude region. Based on their comparison between the DE-1 and Alouette/ISIS profiles, Persoon et al. (1983) suggested that another transition in the electron density profile presumably occurs in the data gap between the two, i.e. between 3000 and 7000 km. However, they also noted that the Alouette/ISIS profile was likely biased toward regions of higher densities and that the actual density at 3000 km may be an order of magnitude lower. Nevertheless, it is interesting to note that the H^+ velocity observed on Akebono did exhibit a transition near 4000 – 5000 km (cf. Figure 10 below), and that the transition from dominant O^+ at low altitudes to dominant H^+ at high altitudes is expected to occur between 4000 and 7500 km, depending on the neutral hydrogen density.

3.3 Akebono Observation

Both polar wind ion and electron measurements were made on Akebono (Abe et al., 1993a, 1996, 2004). The ion measurements were made using the suprathermal mass spectrometer (SMS) (Whalen et al., 1990), and covered the altitude range from 1000 to 10,000 km and spanned the period from April 1989 to December 1999, over close to a full solar cycle starting from the eve of the Solar Cycle 22 (SC22) maximum. The electron measurements were made using the thermal electron detector (TED) (Abe et al., 1990), and spanned a much more limited altitude range (1000 – 4000 km mostly).

The SMS was a 3-stage, folded Bennett-type radio-frequency ion mass spectrometer and it measured the mass-per-charge, energy-per-charge, and angular distributions of thermal (0.1-25 eV/q) and suprathermal-energy (<4 keV/q) ions in the spacecraft spin-plane (Yau et al., 1998). In its “thermal fast scan mode”, SMS used a retarding potential analyzer (RPA) for ion energy analysis, and sampled 4 ion species (H^+ , He^+ , O^+ , and typically O^{++}) at 32 spin angles and 8 RPA steps in each 6-s spacecraft spin. Since Akebono was Sun-pointing, and SMS had a large acceptance angle out of the spacecraft spin plane ($\pm 60^\circ$ in the large aperture mode), this allowed incident ion sampling over the full 180° pitch angle range in most cases at high latitudes. The TED instrument consisted of two orthogonal, planar probes that viewed in the radial direction in the spin plane. Each probe completed four 0.5-s voltage sweeps in the 0–5 V range in each spacecraft spin, and measured the second harmonic component of the incident probe current as a function of the probe voltage. The measured current data in each sweep was used to derive the electron temperature in the probe direction, resulting in 8 independent electron temperature estimates per spin.

As described in Drakou et al. (1997), an iterative fitting procedure was applied to the measured ion count rate data, in which the different ion species were assumed to have the same perpendicular ion convection velocity (perpendicular ion drift energy proportional to ion mass),

and the detailed instrument energy and angular response was taken into account. The fitting procedure derived initial estimates for the spacecraft potential, perpendicular ion velocity, and the parallel ion velocity of each species from the moments of the count rate distributions, and then iteratively corrected for the shielded portions of the incident ion distributions below the spacecraft potential in the case of positive spacecraft charging and fit the corrected distribution of each species to a drifting Maxwellian until convergence. The procedure provided an estimate of the density, temperature, parallel ion velocity, and the spin-plane component of the perpendicular velocity for each species, in addition to the estimate of spacecraft potential.

Abe et al. (1993a) presented a statistical study of the observed polar wind characteristics on Akebono between 1000 km and 10,000 km (initial Akebono apogee) in the first 2 years of the Akebono mission (February – September 1990 and March – August 1991), near the maximum of SC22. This study was focused primarily on the velocity of the three major polar wind ion species (H^+ , He^+ , and O^+), and was based on data above 80° invariant from over 400 polar orbit passes. As noted by these authors, the data sampling was concentrated on the dayside at high altitude, and was dominated by spring and winter, summer, and spring data at high, mid, and low altitude, respectively.

Figure 10 shows the averaged parallel ion velocity of each species and its standard deviation as a function of altitude, on both the dayside (06 to 18 MLT; Figure 10a) and the nightside (18 to 06 MLT; Figure 10b). The dayside and nightside profiles were qualitatively similar for all three species: the (approximately) monotonic increase in velocity with altitude, the mass dependence of the magnitude of the velocity, and the starting altitude of detectable upward velocity are apparent in both cases. The H^+ velocity typically reached 1 km/s near 2000 km, the He^+ and O^+ velocities near 3000 and 6000 km. For all three species, the velocity on the dayside was significantly larger than that on the nightside. For example, the H^+ , He^+ , and O^+ velocity at 10,000 km was about 12, 6, and 4 km/s, respectively, on the dayside, and ~7, 4, and 3 km/s on the nightside.

On the dayside, the averaged O^+ velocity began to increase near 5000 km, and reached a maximum of about 4 km/s near apogee. Its standard deviation was smaller compared with (less than 50% of) the mean above this altitude, but was comparable or greater below, reflecting the fact that the measured velocity data samples were predominantly upward above this altitude but were comprised of both upward and downward velocity samples at lower altitudes. On the nightside, the averaged O^+ velocity started to increase from zero at 7000 km. It is possible that the small negative velocity (magnitude less than 1 km/s and comparable to the standard deviation) between 5000 and 6000 km might reflect the larger number and/or velocity values of downward velocity samples compared to the upward velocity samples in this altitude region, although Abe et al. (1993a) noted that it may possibly be an artifact in the data due to ion flows perpendicular to the spin plane.

Abe et al. (1993a, 1993b) investigated the possible dependence of the polar wind on magnetic activity, by sorting the measured velocity data by the Kp index, and found that the velocity of H^+ and He^+ appeared to be more variable during active times than at quiet times. For example, the variability (standard deviation) of the H^+ velocity was as much as 50% of the mean at apogee during active times. However, the average velocity was only weakly dependent on Kp over the range of Kp sampled (1– to 4+), and the active-time value was only marginally larger than that at quiet times for both species. The active-time O^+ velocity was also similar to its quiet-time value, except at 5000–7000 km where it was as much as a factor of 2 larger.

Figure 10 shows clearly that near solar maximum, the acceleration (increase of velocity with altitude) of the H⁺ polar wind ions was largest below 4000 km. Abe et al. (1993b) attributed this acceleration to the presence of the polarization electric field in the polar wind due (primarily) to the plasma pressure gradient along open magnetic field lines in the polar ionosphere. These authors compared the observed ion velocity at a given altitude with the ambient electron temperature under a variety of magnetic activity conditions, and found the magnitude of ion acceleration to correlate strongly with the electron temperature.

Figure 11 shows the scatter plot of the H⁺ ion velocity versus local electron temperature in three altitude intervals centered at 2000, 2500, and 3000 km, respectively. At all three altitudes, the velocity increased with electron temperature. The rate of increase was smallest at the lowest altitude and largest at the highest altitude. For an increase of electron temperature from 4000 K to 7000 K, the increase in velocity was about 50 percent (from 1.0 to 1.5 km/s) at 2000 km, and a factor of 3 (from 1.3 to 4 km/s) at 3000 km. Abe et al. (1993b) noted that the larger rate of increase at higher altitude reflects the cumulative increase in ion velocity due to the ambipolar electric field along the field line, and the direct relationship between the local magnitude of ion acceleration and that of the ambipolar electric field responsible for the acceleration.

It is interesting to note here that the electron temperature typically increases with altitude (i.e. has a positive gradient) in the polar ionosphere. Theoretically, the polarization electric field in the polar wind is related to the electron plasma pressure (density and temperature) as $qE = -kT_e [d \ln(n_e T_e) / dr]$ where E is the polarization electric field, n_e and T_e are the electron density and temperature, and q and k are the electron charge and the Boltzmann constant, respectively. In the case of positive electron temperature gradient (i.e. increasing electron temperature with altitude), the polarization electric field remains upward provided that the electron density decreases with altitude more rapidly, as was usually observed on Akebono up to at least 4000 km. Thus, the polar wind ions are expected to experience a continuous acceleration in velocity in the course of its upward expansion.

The MLT dependence of the polar wind ion flux strongly resembles the corresponding dependence of the observed ion velocity. Figure 12 shows the upward H⁺ ion flux for each MLT sector near solar maximum in 1990 and 1991, as a function of invariant latitude for northward and southward IMF conditions ($B_z \geq 1$ nT and $B_z \leq -1$ nT), respectively. The flux was observed between 6000 and 9000 km, and normalized (projected) to 2000 km altitude in this figure. Above 75° invariant, the ion flux was largest in the noon sector and smallest in the midnight sector. Above 80° invariant in the polar cap, the observed ion flux was due predominantly to the polar wind. Below 80° invariant the flux in the noon and dusk sectors is believed to contain a significant contribution from the cleft ion fountain also, at least in the case of southward IMF (Figure 12b). The narrow latitude distribution in the midnight sector was in direct contrast to the broad distributions in the other MLT sectors. The latter is consistent with the larger ambipolar electric field in the sunlit polar wind, which is attributed to escaping atmospheric photoelectrons. The H⁺ flux in the noon sector was in the range of $1\text{--}20 \times 10^7 \text{ cm}^{-2} \text{ s}^{-1}$. As will be evident in Figure 13 below, the corresponding O⁺ flux was typically a factor of 1.5–2.0 smaller. The observed H⁺ flux was comparable to the range of flux observed on ISIS-2 at 1400 km in the declining phase of SC 20 ($\sim 2\text{--}20 \times 10^7 \text{ cm}^{-2} \text{ s}^{-1}$; Hoffman and Dobson (1980)), and the storm-time flux observed on DE-1 at 2 R_E altitude near the maximum of SC 21 ($20 \times 10^7 \text{ cm}^{-2} \text{ s}^{-1}$ when normalized to 2,000 km; Nagai et al. (1984)).

Figure 13 shows the integrated flux of both H⁺ and O⁺ above 75° invariant for each MLT sector as a function of the Kp index. In both species, the integrated flux was largest in the noon

sector and smallest in the midnight sector under all Kp conditions. The flux in the noon sector was at least a factor of 10 larger than that in the midnight sector. The O⁺ flux was generally a factor of 1.5–2 smaller than the corresponding H⁺ flux in all MLT sectors and Kp conditions, except at magnetically active times (Kp ≥ 5) outside of the midnight sector. In both species, the flux appeared to be only weakly dependent or independent on Kp. The larger H⁺ flux in the noon and dusk sectors at quiet times (Kp ≤ 2) may be attributed to the fact that the dayside cleft is centered at about 78° invariant and that the observed ions above 75° invariant likely included a significant component of the cleft ion fountain at these times.

Figure 14 shows the outflow rate of both species above 75° latitude, as a function of the Kp index and IMF B_z, respectively. The rate was derived by integrating the integrated ion flux at a particular Kp index (in Figure 13) or IMF B_z over all MLT. This figure also shows the outflow rate of both species below 75° invariant, to provide a comparison of the relative contributions between the polar wind and auroral flows to the overall thermal ion outflow in the high-latitude ionosphere. In general, the rate above 75° invariant appeared to be weakly dependent on Kp for both species. The H⁺ rate decreased by a factor of 2 while the O⁺ rate increased by about a factor of 1.7 as Kp increased from 1 to 6, and both rates decreased with Kp for Kp above 6. In comparison, the rate below 75° invariant was more strongly dependent on Kp for both species. The H⁺ rate increased by a factor of 2 as Kp increased from 1 to 3, and decreased by a factor of 1.4 as Kp increased from 3 to 7. The O⁺ rate increased monotonically by a factor of 5 as Kp increased from 1 to 7.

For both species, the magnitude of increase of the outflow rate below 75° invariant with Kp was confirmed in the recent study of Cully et al. (2003), which covered a longer (9-year) data period that spans both the maximum of SC 22 and the minimum of SC 23, and examined the dependence of the outflow rate on magnetic activity and solar wind conditions as well as solar radio flux. In Cully et al. (2003), which included measurements up to 85° invariant but was dominated by data samples below 75° invariant, the outflow rate of low-energy H⁺ and O⁺ ions increased by a factor of about 2.5 and 10, respectively, as Kp increased from 1 to 5+ near both solar maximum and minimum. Thus, the increase observed in both Abe et al. (1996) and Cully et al. (2003) clearly reflects the pre-dominance of auroral ion flows below 75° invariant.

In Figure 14, the O⁺ outflow rate below 75° invariant was larger than the corresponding rate above by less than a factor of 2–3 during quiet times (Kp ≤ 2). This means that the quiet-time ion flux per unit area in the polar cap was actually larger than that in the auroral zone, since the area of the auroral zone is about 3 times larger than that of the polar cap. It would be interesting to determine if the same is true at lower altitudes, as that would imply that a significant component of the observed ion flux in the polar cap originates from the topside polar cap ionosphere rather than the dayside cleft or the auroral ionosphere.

At moderate and active times, the O⁺ outflow rate below 75° invariant was a factor of 3–5 larger than the corresponding rate above. A number of factors are believed to contribute to the larger increase in rate with Kp below 75° invariant. As the level of geomagnetic activity increases, the auroral oval expands equatorward, resulting in a smaller portion of the dayside cleft and nightside auroral zone above 75° invariant. At the same time, the overall rate and the spatial regions of ion acceleration both increase, in both the auroral zone and the polar cap, resulting in an exponential increase in the total ion outflow rate. The speed of anti-sunward convection also increases, resulting in the transport of ions from the dayside cleft further into the nightside of the polar cap. The interplay between these factors combines to increase the overall

magnitude of thermal O^+ outflow in the polar cap during active times. Whether and by how much it also increases the relative contributions of the cleft ion fountain and the topside dayside cleft ionosphere to the overall outflow are less clear. Measurements in the 500 to 3000 km altitude region at both cleft and polar cap latitudes may shed important light on this question, as this altitude region spans the bottom-side of the auroral bulk upflow, polar wind, and cleft ion fountain regions.

The same factors above are believed to apply in the case of H^+ , where the outflow rate above 75° invariant decreased monotonically with K_p . Compared with O^+ the increase in overall rate and spatial regions of H^+ ion acceleration with geomagnetic activity is more modest. Hence the increase in the total ion outflow rate is also smaller. Also, because of the so-called “geomagnetic mass spectrometer effect” (Moore et al., 1986), different ion species accelerated to the same energy in the upward field-aligned direction have the same convection velocity but a different parallel velocity that is inversely proportional to the square root of their ion mass. Thus, for a given geomagnetic activity level and anti-sunward ion convection strength, a smaller fraction of an H^+ ion population originating from the dayside cleft will reach the polar cap at a certain altitude compared with an O^+ population with the same parallel energy distribution. This is believed to account for the qualitatively different K_p dependences between the H^+ and O^+ rates in the polar cap.

As the level of geomagnetic activity increases, the frequency of acceleration of the polar wind ions to higher energies is expected to increase. Consequently, the fraction of the polar wind ion population beyond the upper energy-limit of the thermal ion measurements is also expected to increase, and this may account for the reduction in the observed outflow rate at very high K_p index. Horita et al. (1993) reported the frequent occurrence of ion depletion zones at altitudes down to 3000 km in the nightside polar cap above 70° invariant, in which the thermal-energy ion density was below the detection limit of the SMS instrument (10^{-2} cm^{-3}). These authors noted the lack of K_p dependence of ion depletion zone occurrence, and attributed the active-time occurrence to the increase in ion energization to beyond the upper energy limit of the thermal ion measurements (and the quiet-time occurrence to convection vortex in the nightside polar cap).

The outflow rate of both species exhibited very similar IMF B_z dependence, and increased with B_z under northward IMF conditions. This increase is evidently due to the larger flux from the noon and dusk sectors during northward IMF (cf. Figure 12 above), and is consistent with the topside polar cap ionosphere being a stronger and more dominant source of the observed polar wind plasma in comparison with other sources such as the cleft ion fountain and auroral bulk upflow.

Abe et al. (2004) extended their earlier analyses to examine the solar activity and seasonal variations of the H^+ and O^+ polar wind velocity profiles at Akebono altitudes, by including data throughout the April 1989 to December 1998 period. As shown in Figure 6, the average solar radio flux $F_{10.7}$, which is a proxy of solar electromagnetic radiation energy (EUV flux), remained fairly high (> 150) during the first three years of this period, and then decreased gradually to about 70 in late 1993 and remained below 80 thereafter until early 1997. In an attempt to separate the other ion populations from the polar wind, and to minimize the contributions of these populations to the velocity averages in the analysis, Abe et al. (2004) excluded measurements below 77° invariant as well as those in which the upper limit of ion temperature (inferred from the moments of the measured count rate distribution) exceeded 30,000 K.

Figure 15 shows the averaged H^+ polar wind velocity for different levels of $F_{10.7}$ as a function of altitude in the sunlit ($SZA < 90^\circ$) and shadow (non-sunlit, $SZA > 90^\circ$) regions, respectively.

In the sunlit region (Figure 15a), the velocity increased with altitude at all altitudes for all solar flux levels, except at low solar flux ($F_{10.7} < 100$) where it remained almost constant above 4000 km. However, the velocity gradient at different altitudes varied with solar flux. At high solar flux ($F_{10.7} > 180$), the averaged velocity of the H^+ ions increased continuously from 1500 km to 8500 km. In comparison, the increase in velocity with altitude at low solar flux was much larger below 3600 km and much smaller above 4000 km. As a result, the averaged velocity at low solar flux was about 50-60% larger than that at high flux at 4000 km altitude, and was comparable to the latter at high altitude (~ 7000 km). In the non-sunlit region (Figure 15b), the velocity increased with altitude below 4000 km but did not appear to do so significantly above at both low ($F_{10.7} < 100$) and medium ($100 < F_{10.7} < 180$) solar fluxes.

Figure 16 shows the corresponding O^+ velocity profiles for the different levels of $F_{10.7}$. In Figure 16a, the velocity in the sunlit region remained below 1 km s^{-1} below 6500 km but increased with altitude above at high solar flux ($F_{10.7} > 180$). Similar transition in the velocity was observed at 4000 km at medium solar activity level ($100 < F_{10.7} < 180$). At low solar flux, the velocity increased gradually with altitude from 1500 to 7000 km, and reached 4 km s^{-1} at 5000 km. In comparison, the altitudinal increase of the velocity in the non-sunlit region in Figure 16b was more gradual. A comparison of the altitudinal velocity gradients for the three solar flux levels suggests that the altitudinal increase becomes more significant as the solar flux decreases. At high solar flux, the velocity remained below 1.5 km s^{-1} at all altitudes.

The altitudinal gradients of both H^+ and O^+ velocity had very similar solar flux dependence and altitude variations, i.e. larger gradient at low altitude and smaller gradient at high altitude at low solar flux than at high solar flux, resulting in generally higher H^+ and O^+ velocities below 7000 km and 8500 km, respectively, at low solar activity.

Figure 17 shows the averaged active time ($Kp > 3$) H^+ and O^+ velocities at 4000 ± 1000 and 8000 ± 1000 km altitude, respectively, for different seasons as a function of $F_{10.7}$. At 4000 km (Figures 17a and 17b), a transition from high to low velocity was apparent near $F_{10.7}$ of ~ 150 for both H^+ and O^+ . The velocity was generally largest in the summer, and decreased with increasing solar flux. Its variation with solar flux was smallest in the winter. In contrast, at 8000 km (Figure 17c and 17d), the H^+ velocity at high solar flux ($F_{10.7} = 260$) was 30-50% higher than its value near $F_{10.7} = 100$. The O^+ velocity was essentially independent of the solar flux in the summer, and decreased slightly with increasing $F_{10.7}$ over the range of $F_{10.7}$ from 80 to 140 at equinox and the range from 140 to 220 in the winter.

Abe et al. (2004) compared the averaged active-time ($Kp > 3$) velocity profiles of both species in different seasons at low ($F_{10.7} < 100$) and high ($F_{10.7} > 180$) solar flux, respectively. At low solar flux, the difference in velocity between summer and equinox was insignificant compared with the standard deviation, which was typically 20–40%. In comparison, at high solar flux, the corresponding difference was significantly larger than the standard deviation at high altitude (above 5000 km), where the equinox velocity was as much as a factor of 1.5–2 larger, and the velocity gradient was fairly constant with altitude and was largest in the summer and smallest in the winter. This implies that the magnitude of ion acceleration was largest in the summer, and smallest in the winter.

Figure 18 compares the averaged quiet-time ($Kp \leq 2$) invariant latitude (ILAT) and MLT distributions of H^+ and O^+ velocity at 6000–8000 km altitude, at low ($F_{10.7} < 100$), medium ($100 < F_{10.7} < 180$) and high ($F_{10.7} > 180$) solar flux levels, respectively. This figure shows the distributions down to 60° invariant, in order to illustrate the solar activity dependence of the observed ion velocity at both auroral and polar cap latitudes. As noted above, the data below 77°

invariant were excluded in Abe et al. (2004) and in the altitude profiles in Figure 15 to 16 above. For both species, the ILAT-MLT distribution was essentially similar at all solar fluxes, and slightly more extended latitudinally at low solar flux. However, the O^+ velocity was about a factor of 2 higher on average at low solar flux than it was at higher flux, not only in the polar cap but also in the auroral region; for example, it was a factor of ~ 3.5 higher at low solar flux was at auroral latitudes at 20 MLT. The corresponding difference in the H^+ velocity was smaller.

Similar differences between solar minimum and maximum were observed for both species at active times ($K_p \geq 4$), when the region of largest ion velocity expanded toward lower latitudes, consistent with the equatorward expansion of the auroral oval. This is reflected in Figure 19, which compares the velocity distributions of the two species at $F_{10.7}$ below 150, under northward ($B_z > 2$ nT) and southward ($B_z < -2$ nT) IMF conditions, respectively. In both H^+ and O^+ (upper and lower panels), the latitude of largest velocity was more equatorward under southward IMF (left panels), while the velocity in the high-latitude polar cap ($>80^\circ$ invariant) was generally larger during northward IMF. As shown in Abe et al. (2004), these relations were also true at high $F_{10.7}$ levels.

The observed seasonal dependence of the polar wind ion velocity profile on Akebono suggests the solar zenith angle (SZA) as an important control parameter of the polar wind outflow. Because the SZA of a given point in the polar cap generally correlates with its anti-sunward distance from the cleft in any season of the year, it is sometimes difficult to separate the SZA dependence of polar wind velocity from the anti-sunward distance dependence. Figure 20 shows the observed SZA dependence of both H^+ and O^+ velocities at 4000 and 8000 km altitude, respectively, under magnetically active ($K_p > 3$) and moderate solar flux ($F_{10.7} > 100$) conditions, over a limited range of invariant latitudes (80° to 85° invariant on the nightside). The limited invariant latitude range corresponded to a limited range of anti-sunward distances from the cleft. At both altitudes, the velocity of both species was larger at smaller SZA, and decreased as the SZA increased from 65° to 115° . The large variation in velocity within the limited range of invariant latitudes (and therefore anti-sunward distance) suggests a strong dependence of the polar wind ion velocity on the SZA.

Because ion mass spectrometers and retarding potential analyzers generally have energy and angular responses that are comparable to the energy and angular widths of the polar wind and other thermal-energy ion populations, ion temperatures estimated from the first moment of measured ion velocity distributions such as those from the DE-1 RIMS, Akebono SMS, and POLAR TIDE instruments are in general upper limit estimates. In their analysis of the polar wind temperature, Drakou et al. (1997) used an alternative technique, in which the measured angular distributions at individual retarding potential analyzer (RPA) settings were fitted iteratively to the theoretical angular and energy response of the instrument to an assumed drifting Maxwellian distribution, to estimate the temperature and parallel velocity of each ion species as well as the spacecraft potential and the perpendicular ion velocity.

Figure 21 shows the estimated ion temperature of H^+ , He^+ , and O^+ from 13 northern polar passes on Akebono between 4000 and 10,000 km during a period of moderate to high geomagnetic activity, as a function of altitude, magnetic local time, and invariant latitude, respectively. The straight line in each panel is a least square fit to the data. In general, the observed temperature was in the range of 0.05 to 0.35 eV and mostly below 0.25 eV. The temperature did not vary significantly with altitude, magnetic local time, or invariant latitude. Note that the data points below 7000 km altitude in the altitude (left) panel and those at 12–06 MLT in the MLT (middle) panel are dominated by data samples at auroral latitudes. This aliasing

in altitude versus local time and invariant latitude sampling is believed to contribute to the apparent magnetic local time and invariant latitude variations in the observed temperature. The observed ions were generally cold at both polar cap and auroral latitudes.

Drakou et al. (1997) used the estimated ion temperature and parallel ion velocity to derive the corresponding ion Mach number (square root of drift energy to thermal energy ratio) for each ion species. In the high-altitude (>7000 km) region of the polar cap, the Mach number of all three species was found to exceed unity and increase with altitude, from ~1.5 to 4, from ~1.5 to 1.8, and from ~5 to 7 in the case of H^+ , He^+ , and O^+ , respectively. In other words, all three species were supersonic above 7000 km. The O^+ ions had a higher Mach number while He^+ had a lower Mach number than H^+ , although the physical reason for this mass dependence is not clear.

The technique of Drakou et al. (1997) provides an independent estimate of the plasma velocity and temperature parameters from each RPA setting. These authors found that the H^+ and O^+ velocity (and ion Mach number) estimates derived from data at the highest RPA setting were often larger than those from data at the lowest RPA setting and those from the moment method. Since at the highest RPA setting the SMS instrument sampled only the highest-energy portion of the ion distribution, this suggests that the latter was perhaps drifting at a higher speed, or that the actual distributions were more complicated than a simple drifting Maxwellian.

Drakou et al. (1997) observed downward flowing He^+ and O^+ with a net downward velocity below ~1.5 km/s below 7000 km on the nightside. Although the observed downward velocity was in some cases attributed to the non-zero minimum pitch angle of the sampled ions and the contribution of the perpendicular ion velocity component, downward flowing He^+ and O^+ ions were clearly present in the polar cap, but were less frequent with increasing altitude compared with their upward flowing counterparts.

As discussed in Drakou et al. (1997), a one-temperature Maxwellian description is a zeroth-order approximation to the actual polar wind distributions, which is theoretically expected to be more complex. As noted in Section 2, a number of polar wind theories and numerical models predict departure from a simple, one-temperature drifting Maxwellian in the form of temperature anisotropy and/or asymmetry in the distribution.

In the case of ion temperature anisotropy, the parallel and perpendicular temperatures are unequal, i.e. $T_{\parallel} \neq T_{\perp}$, and a bi-Maxwellian distribution represents a better approximation to the actual distribution. However, direct experimental confirmation of ion temperature anisotropy has proven difficult. This is because the observed polar wind ion flux on an orbiting spacecraft is typically highly peaked near the spacecraft ram or the upward magnetic field direction due to the large spacecraft ram (or ion drift) speed compared to the thermal ion speed. This makes it difficult to measure simultaneously both the component of the detailed ion velocity distribution along the ram (or magnetic field) direction and the component perpendicular to it, and this explains the scarcity of ion temperature anisotropy measurements in the literature. In Drakou et al. (1997), for example, the estimated ion temperature corresponded to the ion temperature in the direction perpendicular to the ion drift velocity vector, and was essentially independent of the ion temperature along the drift velocity vector when the parallel-to-perpendicular temperature ratio was in the range of 1/3 to 3 ($1/3 < T_{\parallel}/T_{\perp} < 3$).

In the case of asymmetric distributions, external heat flux or ambipolar electric field coupled with Coulomb collisions may result in a skew in the distribution function in the field-aligned direction. Drakou et al. (1997) noted the occasional observation of asymmetric spin-angle distributions in their study which are indicative of the possible presence of heat flux or spatial in-

homogeneity and temperature anisotropy. However, they excluded such data samples in their analysis, by observing the “goodness-of-fit” criteria for the nonlinear least square fit to their data. Biddle et al. (1985) reported asymmetries in the observed distributions on DE-1 RIMS, which they attributed to possible heat flux, and described these asymmetries as a first order correction to a Maxwellian distribution using the Spitzer-Harm heat flux formulation.

As noted earlier in the beginning of this subsection, the TED instrument on Akebono provided 8 independent estimates of electron temperature (averaged electron thermal energy regardless of whether the distribution is Maxwellian) per spacecraft spin. Simultaneous electron temperature measurements in the magnetic field and perpendicular directions were available from a small number of orbit passes in the polar wind region. In some of these orbit passes, measurements at intermediate pitch angles were also available. The TED data in these orbits revealed an asymmetry in the electron velocity distribution in the field-aligned direction in the sunlit polar wind (Yau et al., 1995).

Figure 22 shows the measured electron temperature as a function of electron pitch angle, from a low-altitude orbit pass through the dayside northern polar cap ($>80^\circ\Lambda$, 16-20 MLT) from 2478 to 2818 km altitude. Data from both TED sensors are combined in this figure, in order to cover the full 180° pitch angle range. The measured temperature near the upward magnetic field direction ($>150^\circ$ pitch angle) is significantly larger than that near the downward and perpendicular directions. Also, the data from the two sensors are consistent with each other where they overlap (near 50° and 140° pitch angles). The higher temperatures near the upward magnetic field direction cannot be attributed to wake effects since they were measured at small ram angles, away from the spacecraft wake. Indeed, if spacecraft wake effects were present, they would be expected to increase the measured electron temperatures at the perpendicular and downward directions, which were made at larger ram angles. In other words, the actual temperatures in the downward and perpendicular directions would have been smaller than the measured values, and the actual difference between the upward and downward temperatures would have been larger than observed.

Figure 23 compares the measured electron temperatures in the upward, downward, and perpendicular directions, respectively, from a dayside auroral orbit pass from 792 km at 63° invariant and 10 MLT through its highest invariant latitude location at 78° invariant and 16.2 MLT to 2404 km at 75° invariant and 18.9 MLT. In this figure, the measurements above and below 75° invariant are denoted by squares and triangles, respectively, and the dotted traces above and below the dashed traces correspond to a temperature ratio of 1.25 and 0.8, respectively, between the ordinate and the abscissa. The small range of pitch angles sampled in this orbit pass precluded the measurement of the full pitch-angle distribution. However, it did make the data very well suited for detailed correlations between the three temperatures at various altitudes. The three temperatures were clearly correlated with each other both above and below 75° invariant (i.e. both inside and equatorward of the auroral oval). The upward temperature (solid symbol in the figure) varied from ~ 4000 K to ~ 8000 K, which was due in part to the increase in electron temperature with altitude, and was consistently a factor of 1.5–2.0 higher than the downward temperature, which was comparable to the perpendicular temperature (open symbol). Thus, the measured velocity distribution in the upward magnetic field direction had a higher temperature than those in the perpendicular and the downward directions, i.e. $T_{\text{up}} / T_{\text{down}} \sim 1.5\text{--}2.0$ and $T_{\text{down}} / T_{\perp} \sim 1.0$. In other words, the upward-moving ambient electrons (those with pitch angles near 180° in the northern hemisphere) are on average more energetic than their downward-moving (near 0° pitch angles) and locally mirroring (near 90° pitch angles) counterparts.

The higher electron temperature (average thermal energy) in the upward magnetic field direction relative to that in the downward direction resulted in an estimated heat flux of $\sim 1.0 \times 10^{-5}$ Joule $\text{m}^{-2}\text{s}^{-1}$ in the upward direction at ~ 2500 km altitude (Figure 22). The observed electron temperature anisotropy was attributed to the large ambipolar electric field that was required to maintain quasi-neutrality along the field line in the presence of escaping atmospheric photoelectrons, and to the Coulomb collisions between the low-energy ambient electrons and the more energetic photoelectrons (Yau et al. 1995). The upward heat flux due to the observed electron temperature anisotropy was comparable in magnitude to that carried by the atmospheric photoelectrons (above 2×10^{-6} Joule $\text{m}^{-2}\text{s}^{-1}$), and dominated any downward heat flux that may be present in the polar wind plasma due to electron temperature gradients and the heat flux predicted in polar wind models (e.g., Schunk and Watkins, 1981).

3.5 POLAR Observations

On POLAR, the thermal ion dynamics experiment (TIDE) instrument combined a number of electrostatic energy analyzers with RPA and a time-of-flight mass analyzer, to measure the three-dimensional ion distributions in the 0.3–450 eV energy range once every 6-s spacecraft spin at high energy and angular (22.5° polar angle and 11.25° spin azimuth) resolution (Moore et al., 1995). Its companion plasma source instrument (PSI) used a low-energy Xenon ion and electron source to reduce the electrical potential of the POLAR spacecraft relative to the surrounding plasma to a minimum. Near the POLAR apogee, the plasma density was very low (typically < 10 cm^{-3}). The spacecraft typically charged positive to tens of volts in the presence of sunlight due to photo-ionization on the spacecraft surface, and the severe imbalance between the resulting photoelectron flux leaving the surface and the much smaller incident thermal electron flux on the surface. The large spacecraft potential would prevent low energy ions from reaching the spacecraft. The operation of PSI lowered the spacecraft potential to a few electron volts or less, and allowed the access of low energy ions to the TIDE instrument.

Su et al. (1998) presented a comprehensive survey of observed polar wind characteristics on POLAR at both perigee (~ 5000 km) and apogee ($\sim 51,000$ km altitude, or $9 R_E$ geocentric distance) using TIDE data over the period of April and May 1996, near the minimum of SC 23 and in the early portion of the mission when the mass analyzer was operational. The survey was based on 1-min averaged data from 20 perigee passes and 3 apogee passes, and encompassed H^+ and O^+ at both perigee and apogee as well as He^+ ions at apogee.

Su et al. (1998) restricted their analysis to data in the polar cap region, i.e. poleward of the cleft region and the auroral zone (as identified from ion energy-angle-time spectrograms), and to low-energy ions (< 10 eV at perigee), in order to focus on the “quiet” polar wind. They used an iterative procedure similar to that of Watanabe et al. (1992) on Akebono to “fill-in” (correct for) the distributions shielded by the positive spacecraft potential. For the detailed example given, their procedure increased the estimated ion density by a factor of ~ 2 and decreased the estimated parallel ion velocity by less than 10% relative to the initial estimates from moment calculations.

Figure 24 is adapted from Figures 7 and 8 in Su et al. (1998), and it shows the occurrence distributions of density, parallel velocity, number flux, and temperature, and perpendicular temperature of H^+ and O^+ polar wind, respectively, at 5000 km altitude. For O^+ (right panel), each occurrence distribution is shown for all samples (in solid circles) and for low-solar-zenith-angle ($\text{SZA} < 100^\circ$) data samples only (in open circles), respectively, and the occurrence distribution of parallel number flux is shown for upward and downward flux separately. Near

solar minimum, the H^+ density ranged from <0.1 to 100 cm^{-3} , and its average was $\sim 10 \text{ cm}^{-3}$. The parallel velocity ranged from 10 to 21 km/s and its average was 15 km/s. The parallel number flux was upward and ranged from 10^5 to $10^8 \text{ cm}^{-2} \text{ s}^{-1}$, and its average was $1.2 \times 10^7 \text{ cm}^{-2} \text{ s}^{-1}$. The averaged parallel and perpendicular temperature was ~ 0.12 and 0.23 eV , respectively. The O^+ density ranged from 0.1 to 100 cm^{-3} , and its average was $\sim 7.7 \text{ cm}^{-3}$. The parallel velocity ranged from -3 to 2 km/s and its average was -0.9 km/s , i.e. downward. The averaged downward number flux was $9.5 \times 10^5 \text{ cm}^{-2} \text{ s}^{-1}$, and the averaged upward flux, which is not shown in the figure, was $7.4 \times 10^5 \text{ cm}^{-2} \text{ s}^{-1}$. The averaged parallel and perpendicular temperature was ~ 0.34 and 0.61 eV , respectively.

Su et al. (1998) examined the solar zenith angle dependence of polar wind characteristics in order to assess the influence of solar illumination on the overall polar wind dynamics. Both the H^+ and O^+ densities were independent of SZA below 90° but decreased by about 2 orders and 1 order of magnitude, respectively, as SZA increased from 90° to 125° ; see their Figure 6. On the other hand, in the case of O^+ , the parallel velocity did not vary significantly with SZA over the range of 70° to 130° , while both the upward and downward flux generally decreased with increasing SZA and exhibited orders-of-magnitude variations at a given SZA. In the case of H^+ , both the parallel velocity and number flux exhibited no discernible variations with SZA below 100° ; data above 100° SZA were excluded in their analysis. The large density variation with SZA suggests that solar illumination at the ionospheric level may exert a controlling influence on the characteristics of the polar wind at high altitude. Su et al. (1998) found a strong correlation between the H^+ and O^+ densities and the day-night distance in the solar magnetic coordinate system, the correlation coefficient between the logarithm of O^+ density and the distance (X_{SM}) being 0.98 and the corresponding coefficient for H^+ being 0.93. They noted that such a high correlation is consistent with the cleft ion fountain as the origin of the observed ions. However, there were no definitive trends for the parallel velocities and temperatures with X_{SM} .

Su et al. (1998) also examined the O^+/H^+ composition ratios of the various polar wind parameters, by correlating the density, velocity, and flux of the two species at low SZA (SZA $< 100^\circ$). The O^+ and H^+ densities generally correlated with each other, as did the O^+ and H^+ fluxes to a lesser degree, but there was no clear trend between the O^+ and H^+ velocities. As may be inferred from Figure 24 above, the averaged O^+/H^+ density ratio was ~ 3.54 . The averaged velocity ratio was about -0.07 ; the corresponding flux ratio was ~ 4.19 . The corresponding ratios for parallel and perpendicular temperature were 2.5 and 2.0, respectively. We shall discuss the physical significance of the observed composition ratios later in this subsection.

As noted above, the apogee survey included He^+ in addition to H^+ and O^+ , and was based on three long-duration apogee passes in April and May 1996, when the plasma source instrument (PSI) was turned on and the spacecraft potential was kept at about $+1.8$ to 2.2 V , to allow low-energy ion measurements. Figure 25 is adapted from Figures 15 and 16 in Su et al. (1998). Figure 25a and 25b show the occurrence distributions of density, parallel velocity, number flux and temperature, and perpendicular temperature of H^+ and O^+ polar wind, respectively, at 50,500 km altitude.

In Figure 25a, the H^+ density ranged from 0.01 to 2 cm^{-3} , and its average was $\sim 0.3 \text{ cm}^{-3}$. The parallel velocity ranged from 20 to 110 km/s and its average was 45 km/s. The parallel number flux was upward and ranged from 10^5 to $10^7 \text{ cm}^{-2} \text{ s}^{-1}$, and its average was $1.2 \times 10^6 \text{ cm}^{-2} \text{ s}^{-1}$. The averaged parallel and perpendicular temperature was ~ 1.7 and 1.1 eV , respectively.

In Figure 25b, the O^+ density ranged from 0.001 to 0.3 cm^{-3} , and its average was $\sim 0.05 cm^{-3}$. The parallel velocity ranged from 8 to 32 km/s, and its average was ~ 17 km/s. Note that in contrast to the observed velocities at 5000 km (perigee), where both upward and downward velocities were observed, all observed velocities were upward at this altitude (50,500 km). The averaged number flux was $8.3 \times 10^4 cm^{-2} s^{-1}$. The averaged parallel and perpendicular temperature was ~ 7.5 and 3.4 eV, respectively.

The observed He^+ density ranged from 0.001-0.1 cm^{-3} , and its average was 0.012 cm^{-3} . The parallel velocity ranged from 8 to 63 km/s, and its average was ~ 25 km/s (upward). The averaged number flux was $2.5 \times 10^4 cm^{-2} s^{-1}$. The averaged parallel and perpendicular temperature was ~ 3.0 and 1.5 eV, respectively. Note that the averaged He^+ density was about a factor of 25 and 4 smaller than that of H^+ and O^+ , respectively. As noted in Su et al. (1998), the He^+ count rate observed at POLAR apogee was often close to the TIDE instrument noise level, and only data samples of large ($>10^3$ eV cm^{-3}) He^+ energy-density were included in the analysis. The uncertainty of the derived He^+ bulk parameters due to counting statistics was estimated to be larger than those of the H^+ and O^+ parameters and exceed 20%, but its effect on the derived parameter averages is believed to be insignificant.

Su et al. (1998) computed the Mach number of individual data samples and presented the occurrence distribution of H^+ and O^+ Mach number, respectively. The Mach number of H^+ ranged from ~ 2 to 7, with an average of 4.6; and the Mach number of O^+ ranged from ~ 1 to 8, with an average of 3.5. For He^+ , the average Mach number may be estimated from the ratio of its average parallel drift speed (25 $km s^{-1}$) and average parallel thermal speed (8.5 $km s^{-1}$) to be about 2.5. Thus, all three ion species are supersonic at this altitude.

The composition ratio of the observed density and velocity between H^+ , O^+ and He^+ provides interesting insight into the relative energy gains of the three ion species. Su et al. (1998) found good correlation between the densities of the three species and between their parallel velocities. On average, $n(H^+) : n(He^+) : n(O^+) \sim 25 : 1 : 4.2 \sim 1 : 0.04 : 0.17$ and $v_{||}(H^+) : v_{||}(He^+) : v_{||}(O^+) \sim 2.6 : 1.5 : 1 \sim 1 : 0.57 : 0.38$.

In comparison, the corresponding ratio in the case of equal energy gain due to, for example, ambipolar electric field is $v_{||}(H^+) : v_{||}(He^+) : v_{||}(O^+) = 4 : 2 : 1$. In the case of velocity filtering from a single distant source such as the cleft ion fountain, the corresponding ratio would be expected to be close to 1 : 1 : 1. The fact that the observed ratio lies between these two cases and spans a wide range of values suggests that a number of processes and factors of comparable energy gain probably contribute to the overall ion acceleration, including ambipolar electric field, velocity filtering associated with the cleft ion fountain, gravitational force, and centrifugal acceleration at high altitude due to strong convection electric field.

The observed composition ratios for density and velocity above translate into a density-velocity product ratio of $n v_{||}(H^+) : n v_{||}(He^+) : n v_{||}(O^+) \sim 48 : 1 : 3.3$, compared with the observed parallel flux ratio $\sim 63 : 1 : 3.7$ (Su et al. 1998, Figure 20). The difference between the two O^+/H^+ ratios (48/3.3 versus 63/3.7, or 14.5 versus 17) is believed to reflect the significant difference in asymmetry between the density and velocity occurrence distributions in each species, cf. Figure 25. This can be seen by noting that $\bar{n} = \int n f_n dn$; $\bar{v} = \int v f_v dv$; $\bar{F} = \int F f_F dF$, where f_n , f_v , and f_F are the normalized occurrence frequencies of density, velocity, and flux, and that although $F = n v$ for a given data sample, \bar{F} is in general not equal to $\bar{n} \bar{v}$ unless $f_n = f_v = f_F$.

The observed parallel to perpendicular temperature ratio of the three ion species was significantly different at the two survey altitudes (50,500 and 5,000 km). As may be inferred from the above, the ratio of the averaged parallel to perpendicular temperature, $\langle T_{\parallel} \rangle / \langle T_{\perp} \rangle$, was ~ 1.5 , 2.0 , and 2.2 for H^+ , He^+ , and O^+ , respectively, at POLAR apogee (50,500 km). The corresponding averaged parallel-to-perpendicular temperature ratio, $\langle T_{\parallel} / T_{\perp} \rangle$, was 1.37 and 1.86 for H^+ and O^+ , respectively (Su et al., 1998a, Figure 21). In other words, the parallel temperature was higher than the perpendicular temperature in all three species at 51,000 km. This is the exact opposite of the condition at POLAR perigee (5,000 km), at least for H^+ and O^+ , where the $\langle T_{\parallel} / T_{\perp} \rangle$ ratio was 0.46 and 0.58 for H^+ and O^+ , respectively. The increasing ratio with increasing altitude presumably reflects the conversion of perpendicular to parallel ion energy along the diverging magnetic field line due to conservation of the first adiabatic invariant, and possibly additional ion acceleration or heating along the field line.

The composition ratios of parallel and perpendicular temperatures between the three ion species are of interest. The observed O^+ / H^+ parallel temperature ratio, $\langle T_{\parallel}(O^+) / T_{\parallel}(H^+) \rangle$, was ~ 4.6 , while the corresponding perpendicular temperature ratio, $\langle T_{\perp}(O^+) / T_{\perp}(H^+) \rangle$, was ~ 3.4 . Thus, the O^+ ions have a higher temperature than the H^+ ions in both the parallel and perpendicular directions.

Su et al. (1998) found that for at least H^+ and O^+ , the ion velocity decreased and the ion density increased from the dayside to the nightside, while the temperature did not show any increasing or decreasing trend. As noted by these authors, an increasing trend in both the velocity and the temperature might be expected for a cleft ion fountain origin for both ions.

The POLAR observation shows that near solar minimum: (1) The polar wind is dominated by O^+ at 5000 km and H^+ at 50,500 km, in terms of density; He^+ is a minor constituent at both altitudes. (2) At 5,000 km, H^+ is supersonic and upward, while O^+ is subsonic and on average downward, the averaged downward O^+ flux being slightly greater than the corresponding upward flux. For both species, the perpendicular temperature exceeds the parallel temperature. This may suggest perpendicular ion heating of the polar wind plasma in the topside ionosphere. (3) At 50,500 km, in contrast, the polar wind is supersonic and upward for all ion species. Also, the parallel temperature is significantly higher than the perpendicular temperature, presumably due to the conversion of perpendicular to parallel ion energy along the magnetic field line as explained above. H^+ and O^+ reach an averaged velocity of ~ 45 and 27 km/s, respectively, which is faster than predicted by most polar wind models. (4) At both altitudes, O^+ has a higher temperature than H^+ , and the observed temperature of both species is higher than that from polar wind model predictions. Atmospheric photo-ionization appears to play a controlling role in the density of all polar wind species, and possibly a significant role in the velocity of at least H^+ ; in the case of the O^+ polar wind, low-energy ions from both the cleft ion fountain and the F-region cleft ionosphere are believed to be important contributors, and several other factors may play significant roles in its velocity.

Recently, Huddlestone et al. (2005) re-derived the H^+ polar wind flux estimates near POLAR perigee (5600 ± 1000 km), using revised values of the spacecraft potential that included a 2-volt correction to the measured potential (Scudder et al. 2000). Huddlestone et al. (2005) obtained a revised flux of 6.0×10^7 $\text{cm}^{-2} \text{s}^{-1}$ (normalized to 5000 km), which was a factor of 5 higher than the original Su et al. (1998) estimate (cf. Figure 24 above), and a revised density that was a factor of 3 higher. Huddlestone et al. (2005) interpreted the increased flux estimate in terms of the polar wind being always present but usually hidden by the spacecraft potential. The increased flux estimate clearly demonstrates the critical dependence of polar wind and other in-situ thermal

plasma measurements on the spacecraft potential – and the acute need for its accurate determination.

The analysis of Huddleston et al. (2005) covered the period of April to August 1996, which corresponded to the winter season in the southern hemisphere near solar minimum. While the observed flux on a given day typically varied over 2 orders of magnitude, the maximum flux appeared to decrease by an order of magnitude from near (southern fall) equinox to winter solstice. Likewise, the observed flux at a given SZA varied over a similar order of magnitude, while the averaged flux decreased with increasing SZA above 90° , as found in Su et al. (1998).

Huddleston et al. (2005) restricted their analysis to ions below 3.5 eV in the sensor frame in order to isolate the polar wind from more energetic ions, and to data samples with smooth pitch-angle distributions in which the differential ion flux exceeded $10^5 \text{ cm}^{-2} \text{ sr}^{-1} \text{ s}^{-1}$. They characterized the observed polar wind distribution as a function of MLT and invariant latitude in terms of its averaged full-width-half-maximum (FWHM) energy and pitch angle ranges. Figure 26 summarizes the observed distribution in polar plot format, and identifies the energy and the pitch-angle ranges in each invariant latitude and MLT bin. Above 80° invariant, the observed energy range was from 0.5 eV to 1.5 or 2.0 eV at all MLT. Below 80° invariant, the energy range was larger near the dayside cleft and the nightside auroral zone, where it varied from 0.5 eV to 2.5 or 3.0 eV in the 03–12 and 17–24 MLT sectors between 75° and 80° invariant, and largest in the morning sector, where it varied from 0.5 eV to 3.0 or 3.5 eV in the 02–08 MLT sector between 70° and 75° invariant. The observed pitch-angle range varied between 0° – 25° and 0° – 55° , but was typically smallest in the morning sector. This suggests that the polar wind originating from the morning sector had a larger flow velocity and temperature and was also more field-aligned. As noted in Huddleston et al. (2005) and demonstrated earlier in Cully et al. (2003), the initial energy and pitch angle values of an individual polar wind (and other thermal-energy) ion at low altitude appear to have an important effect on its ultimate fate (destination). More observational knowledge of detailed polar wind velocity distributions is clearly needed.

Elliott et al. (2001) examined TIDE data in several (~ 10) northern POLAR apogee passes in the period from April to July 1996, to investigate the influence of the solar wind on O^+ ions at high altitudes. Both H^+ and O^+ ions were observed, and only upward ions were observed in both species. H^+ was observed throughout the 4.5–7.8 R_E altitude range of the polar cap except for brief intervals. In comparison, O^+ was observed much less frequently, and its density was an order of magnitude smaller than the H^+ density, except at times of high solar wind speeds and large solar wind dynamic pressures. The lower occurrence frequency of O^+ is perhaps not surprising given the lower O^+/H^+ density ratio of the polar wind population at low altitudes near solar minimum, and that a larger fraction of the O^+ events may be below the detection threshold of TIDE. The absence of any observed downward H^+ or O^+ ions implies that downward H^+ or O^+ ion fluxes were absent or too low to be detectable by TIDE above 4.5 R_E altitude.

Elliot et al. (2001) found that, perhaps surprisingly, the O^+ density did not appear to depend on the orientation of the IMF, B_z , given that at least a fraction of the O^+ observed in the high-altitude polar cap is believed to originate from the cleft ion fountain, and the latter depends strongly on anti-sunward convection, which is determined primarily by IMF B_z .

4. Summary Discussions

Over the past 40 years since the seminal papers of Nishida (1966) and others (Axford 1968, Banks and Holzer 1968, Marubashi 1970), observations from several polar-orbiting satellites

have confirmed the existence of the polar wind as well as established its basic characteristics. Table 2 summarizes statistical studies or surveys of polar wind ion or electron observations using data from 10 or more satellite orbit passes. As summarized in Table 2 and in Figure 5, these observations were made from the ISIS-2, DE-1, Akebono, and POLAR satellites over the altitude range of 1000 to 50,500 km, and spanned different phases of SC 20–23. Ion observations were made on all four satellites. The ISIS-2 and DE-1 observations were both made in the declining phase of the solar cycle, and covered the 1000–4000 km altitude range. The POLAR observations were made at solar minimum, and were focused at the 5000–6000 km and 29,000–50,500 km altitude (near the POLAR perigee and apogee) region, respectively. The Akebono observations were made over a 10-year period spanning two 11-year solar cycles, and covered the 1000–10,000 km altitude range. Electron measurements were also made on DE-1 and Akebono. The DE-1 electron observations covered a higher altitude range (7000–23,300 km) than that of the corresponding ion observations (1000–4000 km). The Akebono electron measurements were mostly below 3000 km.

A composite picture of the polar wind emerges from these observations:

- (1) The polar wind is composed primarily of electrons and H^+ , He^+ and O^+ ions. Its ion composition varies with the solar cycle, and is dominated in density by O^+ ions up to at least 4000 km and perhaps 6000–7000 km (Figure 6 and Table 2).
- (2) On average, the velocity of polar wind ions increases with altitude, and correlates with the electron temperature at a given altitude. This demonstrates the relationship between the magnitude of polar wind ion acceleration and that of the ambipolar electric field responsible for the acceleration (Figure 10 and 11).
- (3) The velocity of polar wind ions is higher on the dayside than on the nightside. This suggests the possible increase in the amplitude of the ambipolar electric field or the presence of additional ion acceleration on the dayside due to escaping atmospheric photoelectrons (Figure 10).
- (4) The velocity ratio between ion species spans a wide range of values, and on average lies between unity and the inverse square root mass ratio of the species, e.g. $1 < v_{||}(H^+) / v_{||}(O^+) < [m(O^+)/m(H^+)]^{1/2} = 4$. This suggests that a number of processes and factors of comparable energy gain probably contribute to the overall ion acceleration (Figure 10, 24 and 25).
- (5) The H^+ ions typically attain significant velocity (0.5 km/s or greater) at 1000–1500 km altitude, and reach average velocities of ~12 km/s at 10,000 km and ~45 km/s at 50,500 km, respectively (Figure 6, 7, 10 and 25).
- (6) The rate of increase with altitude is greatest at low altitude (below 4000 km for H^+) on both the dayside and the nightside (Figure 10).
- (7) The altitude profile of the rate of velocity increase varies with the level of solar activity (as measured by the solar radio flux $F_{10.7}$ index), the rate of increase at high $F_{10.7}$ being larger at low altitudes (below 5000 km) and smaller at high altitudes (above 7000 km) compared with that at low $F_{10.7}$ (Figure 15 and 16).
- (8) The average velocity does not vary significantly with the level of magnetic activity (as measured by the Kp index). However, the standard deviation of the velocity at a given altitude is often comparable to the average of the velocity, particularly during times of high Kp. This indicates a large variation in the measured velocities (Figure 7 and 10).
- (9) Compared with H^+ and He^+ , O^+ ions attain significant average upward velocity at higher altitudes. Also, the standard deviation to average ratio of O^+ velocity is typically larger at low altitudes (below 4000 km), which indicates the comparable occurrence of ions with upward and downward net (measured) velocities, respectively (Figure 10).

- (10) The O^+ velocity below 4000 km correlates with the IMF B_z , and is on average downward during southward IMF and upward during northward IMF (Figure 8).
- (11) The temperature of polar wind ions is generally low, and is in the range of 0.05–0.35 eV between 7000 and 10,000 km. The parallel-to-perpendicular temperature ratio is less than unity at low altitudes (~ 0.52 for H^+ and ~ 0.55 for O^+ at 5000 km), but exceeds unity at high altitude (~ 1.5 for H^+ and ~ 2.0 for O^+ at 50,500 km) (Figure 21, 24 and 25).
- (12) In the absence of simultaneous ion velocity and temperature measurements at (subsonic to supersonic) transition altitudes, the H^+ , He^+ , and O^+ ions are estimated to reach sonic speed (Mach number of 1) near 1500, 3000, and 6000 km, respectively, on average, based on the measured ion velocities at transition altitudes and the averaged ion temperature (0.02 eV) above 7000 km.
- (13) All three ion species are supersonic by the time they reach 7000 km, the ion Mach number of H^+ , He^+ , and O^+ being ~ 1.5 , 1.5, and 5, respectively at this altitude and increasing to ~ 4.6 , 2.5, and 3.5 at 50,500 km (Table 2).
- (14) The electron density of the polar wind appears to transition to a slower density decrease with increasing altitude at 1000–1500 km. This is believed to be consistent with the transition of the H^+ polar wind from subsonic to supersonic speed in this altitude region.
- (15) At higher altitude, the median electron density follows a power law relationship with geocentric distance with a power law index of -3.85 , i.e., $n_e \propto R^\alpha$ where $\alpha = -3.85 \pm 0.32$, and ranges from ~ 35 to ~ 1 cm^{-3} from 7000 to 23,300 km altitude (2.1 to 4.66 R_E geocentric). This suggests an approximately linear increase in the polar wind ion velocity with geocentric distance over this altitude range (Figure 9).
- (16) The temperature of the polar wind electrons is generally higher than that of the ions, and is in the range of 0.3 – 0.7 eV, at least at low altitude (below 4000 km); reliable electron temperature estimate is difficult to obtain in regions of low plasma density at higher altitudes (Figure 11, 22 and 23).
- (17) The temperature of sunlit polar wind electrons is higher in the upward direction compared with the perpendicular and downward directions, i.e. $T_{up}/T_\perp \sim 1.5-2$, $T_{down}/T_\perp \sim 1$. The temperature anisotropy is absent in the non-sunlit polar wind, and is attributed to the ambipolar electric field that is required to maintain quasi-neutrality along the field line in the presence of escaping atmospheric photoelectrons, and to Coulomb collisions between the electrons and the photoelectrons (Figure 22 and 23).
- (18) The different polar wind ion species have markedly different seasonal dependences in general. In the case of He^+ , the flux has a winter-to-summer ratio of ~ 20 , which is attributed to the seasonal variations of neutral atmospheric helium and molecular nitrogen, which affect the photo-ionization rate of helium, and the loss rate of He^+ due to the He^+-N_2 charge-exchange reaction, respectively.
- (19) The density of both H^+ and O^+ depends strongly on the solar zenith angle (SZA), and decreases by a factor of 10 and 100, respectively, at 5000 km altitude as SZA increases from 90° to 125° . The velocity of both species also decreases slowly as SZA increases above 100° (Figure 20 and Table 2).

Overall, the different observations in Table 2 in general complement each other in terms of altitude and time coverage, as well as corroborate with each other in most aspects of the observed polar wind characteristics. Indeed, there is remarkable consistency between the different observations, given the different phases in the 11-year solar cycle in which these observations were made, and the significant variability in polar wind characteristics with local

time, season, SZA, solar and geomagnetic activity levels, and prevailing ionospheric conditions (e.g. electron temperature). Nevertheless, it is important to keep in mind the underlying limitations of the respective measurements. In particular, as demonstrated in the revised H^+ polar wind ion flux estimates in Huddleston et al. (2005), polar wind ion measurements are critically dependent on the accurate determination of the spacecraft potential, particularly in the case of positive spacecraft potential and at high altitudes. In the case where velocity phase space sampling is restricted to only a portion of the 4π steradians, such as on DE-1 and Akebono, they are also subject to additional uncertainties associated with the un-sampled velocity components.

It is apparent from Table 2 and Figure 5 that significant gaps exist between the observations in several areas. One is high-altitude ion and electron observations (above 10,000 km) at solar maximum and the ascending phase of the solar cycle, and ion or electron observations in the other phases of the cycle. In particular, it would be of interest to determine from such data if the polar wind flow undergoes transitions at different altitudes in different phases of the solar cycle, and whether the observed dominance of H^+ over O^+ near POLAR apogee at solar minimum persists in the rest of the solar cycle. High altitude observation in conjunction with measurements of the cross polar cap potential and/or the convection electric field at ionospheric level will be particularly useful for assessing the relative importance of centrifugal acceleration, convection and other polar wind ion acceleration mechanisms, and may shed interesting light onto the possible connection between polar wind and cold, dense ion flows observed in the magnetotail on GEOTAIL (Seki et al., 1998).

Another gap is 3D ion velocity observations in the topside ionosphere below 1500 km at both polar-cap and auroral latitudes, where collisions dominate, the parallel ion velocity is expected to be small or negligible, and the ions may convect in or out of the polar cap from time to time and constitute a significant source of polar wind ions at higher altitudes. It should be possible to definitively identify the trajectories of such ions from a combination of in-situ observation, ground-based convection electric field observation (using EISCAT, SuperDARN or PolarDARN), and time-dependent 3-dimensional polar wind models.

Another gap in existing observation is the relative scarcity of quantitative He^+ flux measurements compared with those of H^+ and O^+ , due in part to the lower He^+ density and the consequent need of stringent mass discrimination (i.e. avoidance of contamination by major ion species) in the ion composition measurements. The quantitative determination of the total He^+ ion outflow rate (fluence) associated with the polar wind and energetic upflowing ionospheric ions may be important to the question of terrestrial helium budget (Axford 1968). Another related observation of interest is that of minor ions in the polar wind population. Yau et al. (1991) reported significant variability in minor ion composition at Akebono altitudes in the high-latitude ionosphere. Demars and Schunk (1994) modeled the behavior of multiple minor ions including O^{++} and NO^+ in their 16-moment model. The characteristics of minor ion species are expected to provide sensitive tests of polar wind model predictions.

Several polar wind models have presented solutions on the direction and characteristics of heat flow and their effects on the dynamics of both major and minor species in the polar wind. However, aside from the case study of Biddle et al. (1985) in which the asymmetry in the observed ion velocity distribution on DE-1 was used to infer the presence of upward heat flux, and the measurement of ion temperature anisotropy on POLAR discussed in the preceding section (Su et al., 1998a), direct or indirect observation of ion heat flux does not yet exist with which to test these model predictions. The same is true of detailed observation of ion velocity distributions that would allow one to determine the precise functional form of the ion velocity

distribution and compare it with predictions of double humps or other non-Maxwellian features in the distribution function in various polar wind models (e.g. Barakat et al., 1995).

The existing body of polar wind observations leaves two important questions remaining open in our view. The first question is whether the cleft ion fountain is the sole or dominant source of O^+ polar wind in the high-altitude polar cap. Some observational evidences appear to suggest this to be the case. These include the correlation between the observed O^+ density and velocity on POLAR with the location of observation from the cleft (Su et al., 1998a), and the apparent geomagnetic mass dispersion in the anti-sunward direction. On the other hand, evidences that appear to suggest the opposite also exist. These include the lack of IMF dependence in the observed O^+ polar cap ion occurrence and flux distributions in the polar cap, the different apparent seasonal dependence of cleft ion fountain occurrence and O^+ polar wind flux, and the dominant SZA dependence of polar cap ion velocities (Abe et al., 2004). It is believed that detailed studies based on coordinated observations at multiple altitudes and latitude locations in different seasons and under different IMF conditions will be required to address this question more definitively.

The second question relates to the magnitude of the lowest-energy-per-charge component of H^+ polar wind (the component below the spacecraft potential), and whether it represents a dominant source of plasma in the magnetosphere. The recent study of Huddleston (2005) found that the estimated H^+ polar wind flux using revised values of the spacecraft potential increased by a factor of 5 from the original estimate of Su et al. (1998), to a value that is sufficient to supply the observed plasma densities in the plasma sheet and the tail lobes. The flux value derived by these authors (6.0×10^7 ions $cm^{-2} s^{-1}$ at 5000 km altitude during local winter and magnetically quiet conditions at solar minimum) compares with that of Chandler et al. (1991) on DE-1 (5.0×10^7 ions $cm^{-2} s^{-1}$ at 1000–4000 km altitude in the winter), and corresponds to a normalized flux of $\sim 1.9 \times 10^8$ $cm^{-2} s^{-1}$ at 1400 km, which is a factor of about 3 to 6 larger than the flux observed on ISIS-2 (Hoffman and Dobson 1980) in winter and magnetically quiet conditions in the declining phase of the solar cycle ($3\text{--}7 \times 10^7$ ions $cm^{-2} s^{-1}$). New observations with accurate spacecraft potential control or measurements may be needed to shed light on the source of apparent discrepancies between the different measurements and provide a more definitive answer to this question.

Table 1 summarizes the predictions of the different polar wind models discussed in Section 2, and compares them with the observational evidences reviewed in Section 3 above. Table 1 shows that in general, many model predictions remain to be verified experimentally, but that there is good accord between most model predictions and observations where the latter exist. For example, collisionless kinetic models predict (1) the transition from O^+ to H^+ as major ion species above 5500 km and (2) the decrease of the ambipolar electric field amplitude from ~ 0.5 $\mu V/m$ at “baropause” to < 0.02 $\mu V/m$ at higher altitude, resulting in a potential difference of 1.7 V and the acceleration of H^+ ions to supersonic speed below $\sim 10,000$ km. In comparison, (1) the observed transition altitude was above at least 4000 km on DE-1 near solar maximum; and at or near 5000 km on POLAR near solar minimum, and (2) the observed H^+ Mach number was ~ 1.5 at 5000 km on POLAR; and ~ 1 at 5000 km and 1.5–4 above 7000 km on Akebono.

The moments-based models predict (3) the transition of H^+ ions from subsonic to supersonic flow above the H^+O^+ collision region, (4) the increase in H^+ and O^+ densities and temperatures and decrease in their velocities due to convection, (5) the effects of thermal diffusion and diffusion thermal heat flow, namely that downward thermal diffusion increases H^+ density and reduces H^+ temperature and upward flow and that diffusion thermal heat flow cools the topside

H^+ , and (6) the variation of He^+ flux with the neutral atmospheric helium density and the non-negligible velocity of He^+ above the collision-dominated altitudes. In comparison, (3) the H^+-O^+ collision frequency depends on the local ion density and temperature, as does the transition altitude from the collisional to the collisionless region. A definitive experimental test requires simultaneous ion density, temperature, and velocity altitude profiles. (4) There is as yet no definitive experimental test on the effects of convection of H^+ and O^+ densities and velocities at low altitudes; however, evidence exists of ion acceleration at high altitude due to strong convection; this point will be discussed further in point (13) below. (5) Heat flow measurement is difficult to make in the topside ionosphere, and there is as yet no definitive experimental test yet on the effects of thermal diffusion and diffusion thermal heat flow. (6) A factor of $\sim 10-20$ of seasonal variation in He^+ flux was observed on both ISIS-2 and DE-1, and this variation is associated with atmospheric helium and nitrogen density variations. Non-negligible He^+ velocity (≥ 1 km/s) was observed on ISIS-2, DE-1 and Akebono above 1400–2000 km.

The generalized transport equations based models predict (7) the absence of an H^+ ion temperature anisotropy below 2500 km and the existence of parallel-to-perpendicular temperature ratios exceeding unity at high altitude, (8) the dependence of the direction of electron temperature anisotropy on the upper boundary conditions of the polar wind, and (9) supersonic H^+ flow at high altitudes at velocity as large as 16-20 km/s and Mach number in the range of 2.5–4 at or below 12,000 km, and the dominance in ion composition of H^+ in supersonic flow and of He^+ in subsonic flow, respectively. In comparison, (7) the parallel ion temperature $T_{//}$ was observed to be smaller than the perpendicular temperature T_{\perp} at 5000 km, and larger than T_{\perp} at 50,500 km on POLAR. The latter was consistent with prediction but the former was apparently not predicted. (8) The upward electron temperature $T_{//,up}$ at 2000–3000 km altitude exceeds the corresponding perpendicular and downward temperatures (T_{\perp} and $T_{//,down}$) by a factor of $\sim 1.5-2$ in the sunlit polar wind, but is equal to the latter (i.e. $T_{//,up} = T_{\perp} = T_{//,down}$) in non-sunlit polar wind. (9) The observed Mach number of H^+ was $\sim 1.5-4$ above 7000 km on Akebono and $\sim 2-7$ at 50,500 km on POLAR. (10) The observed polar wind on DE-1, Akebono, and POLAR was predominantly supersonic and H^+ or O^+ dominant at high altitude.

The collisional kinetic models predict (11) a slower thermalization of higher-energy particles relative to the thermal-energy ones due to the strong velocity dependence of the Coulomb collision frequency, and the evolution of H^+ ions into a double-humped distribution at 1000–2000 (or higher) altitude. In comparison, the test of this prediction requires the measurement of detailed ion velocity distribution function at sufficiently high sampling resolution in velocity space. Such a test does not yet exist.

Finally, the non-classical polar wind models predict (12) the enhancement of heavy (O^+) ion escape due to perpendicular ion heating at lower altitude followed by magnetic mirroring in Earth's divergent magnetic field, (13) the “centrifugal acceleration” of ions in the parallel direction at high altitude due to strong $E \times B$ convection in regions of curved magnetic field, (14) the scenario of ions convecting through a time-dependent force field through different regions of the high-latitude topside ionosphere and being accelerated to polar wind altitudes, (15) the effect of elevated electron temperature in increasing O^+ ion velocity to a few km/s as the electron temperature increases to 10,000 K, (16) similar increase in O^+ flux by 5 orders of magnitude as the ion temperature at the exobase increases to 10,000 K, (17) the effects of hot magnetospheric electrons in developing a discontinuity in the field-aligned electric field and reducing the potential barrier for O^+ ions, thereby enhancing their escape, and (18) the effects of atmospheric

photoelectrons in increasing the electron temperature and the formation of electron temperature anisotropy in the sunlit polar wind, leading to increased O^+ velocity and flux.

In comparison, (13) ample episodic and statistical evidences exist of ion acceleration at lower altitude in observed thermal-energy O^+ ions on DE-1 and Akebono. (14) Active-time convection electric field maps are often consistent with the transport of flux tubes in and out of the polar cap, which would under certain conditions result in the heating or acceleration of ions in the flux tubes and the eventual upflow of the ions to higher altitudes. (15) No simultaneous observation of elevated electron temperature and large polar wind O^+ ion velocity has been made yet. However, O^+ flow velocity of 1-4 km/s and electron temperature exceeding 5000 – 7000 K have both been observed at times. (16) On the other hand, ion temperatures exceeding a few thousand degrees K have never been observed at exobase to our knowledge. (17) Likewise, no simultaneous observation of hot precipitating magnetospheric electrons and enhanced O^+ polar wind ion flux has been documented, but given the frequent occurrence of precipitating soft electrons or polar rain in the polar cap during times of northern IMF, their effects on enhancing O^+ escape should be easily testable with such simultaneous observations. (18) Day-night asymmetry in polar wind velocity in favor of the dayside was regularly observed on Akebono; as was electron temperature anisotropy in the sunlit polar wind. Both observations may be attributed to escaping atmospheric photoelectrons.

The body of existing observations clearly illustrates the 3-dimensional and time-dependent nature of the polar wind and its drivers, i.e. the solar electromagnetic (solar irradiance) and electrodynamic input (solar wind flux and IMF) and magnetospheric energy input, and the intimate relationship and mixing between the polar wind and other ionospheric outflow populations. The strength of polar ion outflow depends strongly on ionospheric conditions. Cully et al. (2003) found a strong positive correlation between the outflow rates of both H^+ and O^+ low-energy ions (below 20 eV primarily) and the solar EUV flux. The strong correlation was attributed in part to the higher plasma density in the topside ionosphere at times of higher solar EUV flux.

Figure 27 shows the observed low-energy outflow rates on Akebono below 9000 km integrated over all MLT and invariant latitudes in the high-latitude ionosphere (including both polar-cap and auroral latitudes) as a function of the Kp index, and the corresponding suprathermal energy rates on POLAR at the same altitudes (15 eV–16 keV) and on DE-1 above 16,000 km (10 eV–16 keV), respectively. In the case of H^+ , the low-energy rate on Akebono was comparable with the suprathermal energy rate on DE-1 and a factor of 4–10 higher than the suprathermal energy rate on POLAR. This indicates that significant acceleration of H^+ occurs above 9000 km in the high-latitude ionosphere. In contrast, in the case of O^+ , the low-energy outflow rate below 9000 km is below the corresponding suprathermal rate above this altitude, which is in turn below the corresponding suprathermal rate above 16,000 km. This means that a significant fraction of the O^+ ions is accelerated below 9,000 km, and that the acceleration continues between 9,000 and 16,000 km.

The low-energy outflow rates in Figure 27 include contributions from both the polar wind and other low-energy ion outflow populations. Note that a significant fraction of low-energy ions at low altitudes in the high-latitude ionosphere, including polar wind ions, is accelerated to suprathermal energies and appears as suprathermal ion outflows at higher altitudes. In other words, a fraction of low-altitude “polar wind” ions can in general “lose their identities” as thermal-energy ions and become suprathermal ions as they reach higher altitudes. Thus, it is

important to consider polar wind and the other outflow populations in the high-latitude ionosphere as an integrated entity.

In conclusion, satellite-borne ion composition observations over the past 4 decades have confirmed the existence of the polar wind as well as its basic characteristics as predicted by various polar wind theory models. These observations spanned the altitude range from 1000 km to ~50,500 km, and revealed several important features in the polar wind that are unexpected from “classical” polar wind theories. These include the day-night asymmetry in polar wind velocity, appreciable O⁺ flow at high altitudes, and significant electron temperature anisotropy in the sunlit polar wind. These features are attributable to a number of “non-classical” polar wind ion acceleration mechanisms resulting from strong ionospheric convection, enhanced electron and ion temperatures, and escaping atmospheric photoelectrons.

The observed polar wind has an averaged ion temperature of ~0.2–0.3 eV, and a rate of ion velocity increase with altitude that correlates strongly with electron temperature and is greatest at low altitudes (<4000 km for H⁺). The strong correlation is a direct experimental evidence of the ambipolar electric field. The rate of increase below 4000 km is larger at solar minimum than at solar maximum. Above ~6000 km, the reverse is the case. This suggests that the dominant polar wind ion acceleration process may be different at low and high altitudes, respectively. At a given altitude, the polar wind velocity is highly variable, and is on average largest for H⁺ and smallest for O⁺. Near solar maximum, H⁺, He⁺, and O⁺ ions typically reach a velocity of 1 km/s near 2000, 3000, and 6000 km, respectively, and velocities of 12, 7, and 4 km/s, respectively, at 10,000 km altitude. Near solar minimum, the velocity of all three species is smaller at high altitudes.

Gaps in our observational knowledge remain, which include the variability of the polar wind at high altitudes with solar activity level, and specific polar wind model predictions that have yet to be verified or tested observationally. Significant questions remain on (1) the relative contribution between the cleft ion fountain, auroral bulk upflow, and the topside polar-cap ionosphere to the O⁺ polar wind population at high-altitude, (2) the effect of positive spacecraft charging on the lowest-energy component of the H⁺ polar wind population, and (3) the relative importance of the various classical and non-classical ion acceleration mechanisms, including those that are not yet identified.

These questions pose several challenges in future polar wind observations. These include (1) measurement of the lowest-energy component in the presence of positive spacecraft potential, (2) definitive determination and, if possible, active control of the spacecraft potential, (3) definitive discrimination between polar wind and other inter-mixed thermal ion populations, (4) measurement of the 3-dimensional ion drift velocity vector and the parallel and perpendicular ion temperatures, or the detailed 3-dimensional velocity distribution function, (5) the resolution of He⁺ and other minor ion species, and (6) coordinated measurements of the ions, electrons, and neutral populations at multiple altitudes and latitudes in the collision-dominated altitude region.

Acknowledgment

We thank Joseph Lemaire for stimulating discussions and constructive comments. We also acknowledge the support of the Canadian Space Agency and the Natural Science and Engineering Research Council (NSERC) Industrial Research Chair Program, respectively.

References

- Abe, T., et al., 1990. Measurements of temperature and velocity distribution of thermal electrons by the Akebono (EXOS-D) satellite: Experimental setup and preliminary results, *J. Geomagn. Geoelectr.*, 42, 537-554
- Abe, T., et al., 1993a. EXOS-D (Akebono) SMS observations of the polar wind, *J. Geophys. Res.*, 98, 11191-11203
- Abe, T., et al., 1993b. Altitude profile of the polar wind velocity and its relationship to ionospheric conditions, *Geophys. Res. Lett.*, 20, 2825-2828
- Abe, T., et al., 1996. Observations of polar wind and thermal ion outflow by Akebono/SMS, *J. Geomag. Geoelectr.*, 48, 319-325
- Abe, T., et al., 2004. Long-term variation of the polar wind velocity and its implication for the ion acceleration process: Akebono/suprathermal ion mass spectrometer observations, *J. Geophys. Res.*, 109, A09035, doi:10.1029/2003JA010223
- Axford, W.I., 1968. The polar wind and the terrestrial helium budget, *J. Geophys. Res.*, 73, 6855-6859
- Banks, P.M., and Holzer, T.E., 1968. The polar wind, *J. Geophys. Res.*, 73, 6846, 1968
- Bank, P.M., and Holzer, T.E., 1969. High latitude plasma transport: the polar wind, *J. Geophys. Res.*, 74, 6317
- Barakat, A.R., and Barghouthi, I.A., 1994. The effect of wave-particle interactions on the polar wind O^+ , *Geophys. Res. Lett.*, 21, 2279–2282
- Barakat, A.R., and Schunk, R.W., O^+ ions in the polar wind, *J. Geophys. Res.*, 88, 7887-7894, 1983
- Barakat, A.R., and Schunk, R.W., 1984. Effect of hot electrons in the polar wind, *J. Geophys. Res.*, 89, 9771-9783
- Barakat, A.R., and Schunk, R.W., 2001. Effects of wave-particle interactions on the dynamic behavior of the generalized polar wind, *J. Atmos. Solar Terr. Phys.*, 63, 75–83
- Barakat, A.R., et al., 1991. Monte Carlo study of the transition from collision-dominated to collisionless polar wind flow, In: T. Chang, G.B. Crew, J.R. Jasperse, (eds.), *Physics of Space Plasmas (1990)*, SPI Conference Proceedings and Reprint Series, Number 10, Scientific Publishers, Cambridge, MA, pp. 431–437, 1991
- Barakat, A.R., Barghouthi, I.A. and Schunk, R.W., 1995, Double-hump H^+ velocity distribution in the polar wind, *Geophys. Res. Lett.*, 22, 1857–1860
- Barghouthi, I., et al., 2001. A Monte Carlo simulation of the H^+ polar wind: Effect of velocity distributions with Kappa suprathermal tails, *Ap. Sp. Sci.*, 277, 427–436
- Biddle, A. P., et al., 1985. Evidence for ion heat flux in the light ion polar wind, *J. Geophys. Res.*, 90, 8552-8558
- Blelly, P.L. and Schunk, R.W., 1993. A comparative study between standard, 8-, 13- and 16-moment approximations, *Ann. Geophys.*, 11, 443-469
- Brinton, H.C., et al., 1971. Altitude variation of ion composition in the mid-latitude trough region: Evidence for upward plasma flow, *J. Geophys. Res.*, 76, 3738
- Chandler, M.O., et al., 1991. Observations of polar ion outflows, *J. Geophys. Res.*, 96, 1421-1428
- Chandler, M.O., 1995. Observations of downward moving O^+ in the polar topside ionosphere, *J. Geophys. Res.*, 100 (A4), 5795-5800

Cladis, J.B., 1986. Parallel acceleration and transport of ions from polar ionosphere to plasma sheet, *Geophys. Res. Lett.*, 13, 893-896

Cully, C.M., et al., 2003. Akebono/suprathermal mass spectrometer observations of low-energy ion outflow: Dependence on magnetic activity and solar wind conditions, *J. Geophys. Res.*, 108(A2), 1093, doi:10.1029/2001JA009200

Demars, H.G., et al., 1989. Solutions to bi-Maxwellian transport equations for the polar wind, *Planet. Sp. Sci.*, 37, 85–96

Demars, H.G., Schunk, R.W., 1991. Comparison of semikinetic and generalized transport models of the polar wind, *Geophys. Res. Lett.*, 18, 713–716

Demars, H.G., Schunk, R.W., 1992. Semikinetic and generalized transport models of the polar and solar winds, *J. Geophys. Res.*, 97, 1581–1595

Demars, H.G., Schunk, R.W., 1994. A multi-ion generalized transport model of the polar wind, *J. Geophys. Res.*, 99, 2215-2226

Demars, H.G., Schunk, R.W., 1996. Effect of centrifugal acceleration on the polar wind, *J. Geophys. Res.*, 101 (A12), 24565

Demars, H.G., Schunk, R.W., 2002. Three-dimensional velocity structure of the polar wind. *J. Geophys. Res.*, 107(A9), 1250, doi:10.1029/2001JA000252

Dessler, A.J., Michel, F.C., 1966. Plasma in the geomagnetic tail, *J. Geophys. Res.*, 71, 1421

Drakou, E., et al., 1997. Ion temperature measurements from the Akebono suprathermal mass spectrometer: Application to the polar wind, *J. Geophys. Res.*, 102, 17523-17539

Elliott, H.A., et al., 2001. Solar wind influence on the oxygen content of ion outflow in the high-altitude polar cap during solar minimum conditions, *J. Geophys. Res.*, 106, 6067-6084

Ganguli, S.B., 1996. The polar wind, *Rev. Geophys.*, 34, 311-348

Ganguli, S.B., Palmadesso, P.J., 1987. Plasma transport in the auroral return current region, *J. Geophys. Res.* 92, 8673

Ganguli, S.B., et al., 1987. Behavior of ionized plasma in the high latitude topside ionosphere: The polar wind. *Planetary and Space Science* 35, 703–713

Gombosi, T.I., et al., 1985. A time dependent theoretical model of the polar wind, *Geophys. Res. Lett.*, 12, 160-170

Gombosi, T.I., Killeen, T. L., 1987. Effects of thermospheric motions on the polar wind: a time-dependent numerical study, *J. Geophys. Res.*, 92, 4725-4729

Green, J.L., Waite, Jr., J.H., 1985. On the origin of polar ion streams, *Geophys. Res. Lett.*, 12, 149-152

Gurgiolo, C., Burch, J.L., 1982. DE-1 observations of the polar wind - A heated and unheated component, *Geophys. Res. Lett.*, 9, 945-948

Ho, C.W., et al., 1997. Dynamics of the H⁺ and O⁺ polar wind in the transition region as influenced by ionospheric convection and electron heating, *J. Geophys. Res.*, 102, 395-406

Hoffman, J.H., 1970. Studies of the composition of the ionosphere with a magnetic deflection mass spectrometer, *Int. J. Mass Spectrom. Ion Phys.*, 4, 315

Hoffman, J.H., et al., 1974. Initial ion composition results from the Isis 2 satellite, *J. Geophys. Res.*, 79, 4246-51

Hoffman, J.H., Dodson, W.H., 1980. Light ion concentrations and fluxes in the polar regions during magnetically quiet times, *J. Geophys. Res.*, 85, 626-632

Holzer, T.E., et al., 1971. A comparison of kinetic and hydrodynamic models of an expanding ion-exosphere, *J. Geophys. Res.*, 76, 2453

Horita, R.E., et al., 1993. Ion depletion zones in the polar wind: EXOS-D suprathermal ion mass spectrometer observations in the polar cap, *J. Geophys. Res.*, 98, 11439-11448

Horwitz, J.L., Lockwood, M., 1985. The cleft ion fountain: a two-dimensional kinetic model, *J. Geophys. Res.*, 90, 9749

Horwitz, J.L., et al., 1994. Centrifugal acceleration of the polar wind, *J. Geophys. Res.*, 99 (A8), 15051-15064

Huddleston, M.M., et al., 2005. An examination of the process and magnitude of ionospheric plasma supply to the magnetosphere, *J. Geophys. Res.*, 110, A12202, doi:10.1029/2004JA010401, 2005

Lemaire, J., Scherer, M., 1971. Simple model for an ion-exosphere in an open magnetic field, *Phys. Fluids*, 14, 1683-1694

Lemaire, J., Scherer, M., 1972a. Simple model for an ion-exosphere in an open magnetic field, *Phys. Fluids*, 14, 1683-1694

Lemaire, J., 1972b. Effect of escaping photoelectrons in a polar exospheric model, *Space Research XII*, 1413-1416

Lemaire, J., et al., 2007. History of kinetic polar wind models and early observations, *J. Atmos. Solar Terr. Phys.*, this issue

Li, P., et al., 1998. Effect of mid-altitude ion heating on ion outflow at polar latitudes, *J. Geophys. Res.*, 93, 9753-9763

Lie-Svendsen, O., Rees, M.H., 1996. An improved kinetic model for the polar outflow of a minor ion, *J. Geophys. Res.*, 101, 2415-2433

Marubashi, K., 1970. Escape of the polar ionospheric plasma into the magnetospheric tail, *Rep. Ionos. Sp. Res. Japan*, 24, 322-340

Mitchell, Jr., H.G., Palmadesso, P.J., 1983. A dynamic model for the auroral field line plasma in the presence of field-aligned current, *J. Geophys. Res.*, 88, 2131

Moore, T.E., et al., 1986. Upwelling O⁺ ion source characteristics, *J. Geophys. Res.*, 91, 7019

Moore, T.E., et al., 1995. The Thermal Ion Dynamics Experiment and Plasma Source Instrument, *Space Science Rev.*, 71, 409-458

Nagai, T., et al., 1984. First measurements of supersonic polar wind in the polar magnetosphere, *Geophys. Res. Lett.*, 11, 669-672

Nishida, A., 1966. Formation of plasmopause, or the magnetospheric plasma knee, by the combined action of magnetospheric convection and plasma escape from the tail, *J. Geophys. Res.*, 71, 5669-5679

Ogawa, Y., et al., 2000. Simultaneous EISCAT Svalbard and VHF radar observations of ion upflows at different aspect angles, *Geophys. Res. Lett.*, 27, 81-84

Persoon, A.M., et al., 1983. Polar cap electron densities from DE-1 plasma wave observations, *J. Geophys. Res.*, 88, 10123-10136

Pierrard, V., Lemaire, J., 1998. A collisional kinetic model of the polar wind, *J. Geophys. Res.*, 103, 11701-11709

Pollock, C. J., et al., 1990. A survey of upwelling ion event characteristics, *J. Geophys. Res.*, 95, 18969-18980

Raitt, W.J., et al., 1975. A comparison of the temperature and density structure in high and low speed thermal proton flows, *Planet. Sp. Sci.*, 23, 1103-1117

Raitt, W.J., Dorling, E.B., 1976. The global morphology of light ions measured by the ESRO-4 satellite, *J. Atmos. Terr. Phys.*, 38, 1077-1083

- Raitt, W. J., et al., 1977. The influence of convection electric fields on thermal proton outflow from the ionosphere, *Planet. Sp. Sci.*, 25, 291-301
- Raitt, W. J., et al., 1978. Quantitative calculations of Helium ion escape fluxes from the polar ionosphere, *J. Geophys. Res.* 83 (A12), 5617-5623
- Raitt, W.J., Schunk, R.W., 1983. Composition and characteristics of the polar wind, In: Johnson, R.G. (Ed.), *Energetic Ion Composition in the Earth's Magnetosphere*, pp. 99-141, Terra Scientific Publishing, Tokyo
- Schunk, R.W., 2007. Time-dependent simulations of the global polar wind, *J. Atmos. Solar Terr. Phys.*, this issue
- Schunk, R.W., Nagy, A.F., 2000. *Ionospheres Physics, Plasma Physics, and Chemistry*, Cambridge University Press, Cambridge, U.K.
- Schunk, R.W., Sojka, J.J., 1989. A three-dimensional time-dependent model of the polar wind, *J. Geophys. Res.*, 94, 8973-8991
- Schunk, R.W., Sojka, J.J., 1997. Global ionosphere-polar wind system during changing magnetic activity, *J. Geophys. Res.*, 102, 11625–11651
- Schunk, R.W., Walker, J.C.G., 1970a. Thermal diffusion in the F₂-region of the ionosphere, *Planet. Sp. Sci.*, 18, 535-557
- Schunk, R.W., Walker, J.C.G., 1970b. Minor ion diffusion in the F₂-region of the ionosphere, *Planet. Sp. Sci.*, 18, 1319-1334
- Schunk, R.W., Watkins, D.S., 1981. Electron temperature anisotropy in the polar wind, *J. Geophys. Res.*, 86, 91-102
- Schunk, R.W., Watkins, D.S., 1982. Proton temperature anisotropy in the polar wind, *J. Geophys. Res.*, 87, 171-180
- Schunk, R.W., et al., 1978. Effect of diffusion-thermal processes in the high-latitude topside ionosphere, *Planet. Sp. Sci.*, 26, 189-191
- Scudder, J. D., et al., 2000. Photoemission current-spacecraft voltage relation: key to routine quantitative low-energy plasma measurements, *J. Geophys. Res.*, 105, 10.1029/1999JA900423 21281-22942
- Seki, K., et al., 1998. Quantification of tailward cold O⁺ beams in the lobe/mantle regions with Geotail data: Constraints on polar O⁺ outflows, *J. Geophys. Res.*, 103(A12), 29371-29382, 10.1029/98JA02463
- Shelley, E.G., et al., 1972. Satellite observations of energetic heavy ions during a geomagnetic storm, *J. Geophys. Res.*, 77, 6104-6110
- Su, Y.J., et al., 1998a. Polar wind survey with the Thermal Ion Dynamics Experiment/Plasma Source Instrument suite aboard POLAR, *J. Geophys. Res.*, 103, 29305-29337
- Su, Y.J., et al., 1998b. Self-consistent simulation of the photoelectron-driven polar wind from 120 km to 9 RE altitude, *J. Geophys. Res.*, 103, 2279-2296
- Tam, S.W.Y., et al., 1995a. Self-consistent kinetic photoelectron effects on the polar wind, *Geophys. Res. Lett.*, 22, 2107-2110
- Tam, S.W.Y., et al., 1995b. Anisotropic kinetic effects of photoelectrons on polar wind transport, in *Cross-scale coupling in space plasmas*, Horwitz, J.L., Singh, N., Birch, J.L., Eds., *Geophys. Monogr. Series 93*, 133-139
- Tam, S.W.Y., et al., 1998. Further development in theory/data closure of the photoelectron-driven polar wind and day-night transition of the outflow, *Ann. Geophysicae*, 16, 948-968
- Tam, S.W.Y., et al., 2007. Kinetic modeling of the polar wind, *J. Atmos. Solar Terr. Phys.*, this issue

- Titheridge, J.E., 1976. Ion transition heights from topside electron density profiles, *Planet. Sp. Sci.*, 24, 229-245
- Wahlund, J.E., et al., 1992. EISCAT observations of topside ionospheric ion outflows during auroral activity: Revisited, *J. Geophys. Res.*, 97, 3019-3037
- Watanabe, S., et al., 1992. Thermal ion observations of depletion and refilling in the plasmaspheric trough, *J. Geophys. Res.*, 97, 1081-1096
- Whalen, B.A., et al., 1990. The Suprathermal Ion Mass Spectrometer (SMS) for the Akebono (EXOS-D) spacecraft, *J. Geomag. Geoelectr.*, 42, 511-536
- Wilson, G.R., 1992. Semi-kinetic modeling of the outflow of ionospheric plasma through the topside collisional to collisionless transition region, *J. Geophys. Res.*, 97, 10551-10565
- Yasseen, F., Retterer, J.M., 1991. Critical points in the 16-moment approximation, *J. Geophys. Res.*, 96, 1827-1830
- Yasseen, F., et al., 1989. Monte-Carlo modeling of polar wind photoelectron distributions with anomalous heat flux, *Geophys. Res. Lett.*, 16, 1023-1026
- Yau, A.W., et al., 1991. Minor ion composition in the polar ionosphere, *Geophys. Res. Lett.*, 18, 345-348
- Yau, A.W., et al., 1995. Akebono observations of electron temperature anisotropy in the polar wind, *J. Geophys. Res.*, 100, 17451-17463
- Yau, A.W., Andre, M., 1997. Sources of ion outflow in the high latitude ionosphere, *Space Sci. Rev.*, 80 (1-2), 1-26
- Yau, A.W., et al., 1998. Radio-frequency ion mass spectrometer measurements of ion composition, velocity and temperature: The EXOS-D suprathermal mass spectrometer, in *Measurement techniques in space plasmas, particles*, Pfaff, R.F., Borovsky, J.E., Young, D.T., Eds., *Geophys. Monogr. Series*, 102, 307-312

Figure Captions

Figure 1: Calculated electric field and electric potential as a function of altitude in the model of Lemaire and Scherer (1971)

Figure 2: Contour plots of the H^+ velocity distributions at six different altitudes in the collisional kinetic test-particle calculations of Barakat et al. (1995). The velocities v_{\parallel} and v_{\perp} are normalized by the O^+ thermal speed. The dotted line shows the H^+ drift velocity.

Figure 3: Altitude profile of simulated O^+ polar wind velocity in Tam et al. (1998) for a photoelectron to thermal electron density ratio of (a) 0%; (b) 0.05%, (c) 0.1%, and (d) 0.15%

Figure 4: Schematic diagram of polar wind flow in the polar ionosphere: As the polar wind ions flow upward along “open” geomagnetic field lines and undergo anti-sunward convection in the polar cap and dayside cusp poleward of the plasmasphere, they generally increase in both drift speed and temperature. The direction, length, width, and color of the arrows denote the polar wind ion flow direction, speed, temperature, and mass species, respectively.

Figure 5: (a) Mean, maximum and minimum solar radio flux $F_{10.7}$ in each 27-day solar rotation from 1965 to 2005 in solar radio flux unit ($1 \text{ sfu} = 10^{-22} \text{ W m}^{-2} \text{ Hz}^{-1}$), and (b) altitude and epoch range of polar wind observations. Note the large variation of $F_{10.7}$ within a solar rotation near solar maximum.

Figure 6: Polar wind H^+ and O^+ ion densities, H^+ ion flux, and H^+ ion velocity (from top to bottom) observed on ISIS-2 at 1400 km in 1971–1972 in the early declining phase of SC 20, near summer solstice (left) and winter solstice (right). (Hoffman and Dobson, 1980)

Figure 7: Averaged polar wind H^+ ion velocity observed on DE-1 in 1981–1983 in the early declining phase of SC 21 as a function of altitude, (a) for high and low solar radio flux ($F_{10.7} > 190$ and $F_{10.7} < 140$, respectively), and (b) for summer and winter (Chandler et al., 1991)

Figure 8: Averaged polar wind O^+ ion velocity observed on DE-1 in 1981–1983 in the early declining phase of SC 21 between 2000 and 4000 km as a function of IMF B_z . (Chandler et al., 1995)

Figure 9: Median plasma density as a function of geocentric distance in the high-altitude polar cap ionosphere derived from DE-1 PWI data in 1981–1982 (Persoon et al., 1983).

Figure 10: Averaged polar wind H^+ , He^+ and O^+ ion velocity (left panel) and standard deviation (right panel) above 80° invariant observed on Akebono in 1990–1992 near the maximum of SC 22 as a function of altitude, in the (a) dayside and (b) nightside, respectively (Abe et al., 1993a)

Figure 11: Scatter plot of H^+ polar wind ion velocity versus electron temperature observed on Akebono at (a) 2000 km, (b) 2500 km, and (c) 3000 km. (Abe et al., 1993b)

Figure 12: Integrated H^+ ion flux per unit area observed at 6000–9000 km on Akebono and normalized to 2000 km altitude for each MLT sector as a function of invariant latitude under (a) northward (IMF $B_z > 1$ nT) and (b) southward (IMF $B_z < -1$ nT) (Abe et al., 1996)

Figure 13: Integrated ion flux observed at 6000–9000 km on Akebono for each MLT sector as a function of the K_p index: (a) H^+ , and (b) O^+ (Abe et al., 1996)

Figure 14: Integrated H^+ and O^+ ion flux observed at 6000–9000 km on Akebono above and below 75° invariant as a function of (a) the K_p index and (b) IMF B_z (Abe et al., 1996)

Figure 15: (a) Sunlit ($SZA < 90^\circ$) and (b) non-sunlit ($SZA > 90^\circ$) averaged H^+ velocity observed on Akebono as a function of altitude for different levels of solar radio flux ($F_{10.7}$) (Abe et al., 2004)

Figure 16: (a) Sunlit ($SZA < 90^\circ$) and (b) non-sunlit ($SZA > 90^\circ$) averaged O^+ velocity observed on Akebono as a function of altitude for different levels of solar radio flux ($F_{10.7}$) (Abe et al., 2004)

Figure 17: Averaged active-time ($K_p > 3$) (a) H^+ and (b) O^+ velocity at 3000-5000 km altitude and (c) H^+ and (d) O^+ velocity at 7000-9000 km altitude observed on Akebono as a function of solar radio flux ($F_{10.7}$) in different seasons (Abe et al., 2004)

Figure 18: Distribution of averaged quiet-time ($K_p \leq 2$) H^+ and O^+ velocity observed at 6000-8000 km altitude on Akebono for different levels of solar radio flux ($F_{10.7}$) (Abe et al., 2004)

Figure 19: Distribution of averaged H^+ (top) and O^+ (bottom) velocity observed at 6000-8000 km altitude on Akebono at low solar flux ($F_{10.7} < 150$) for negative (left) and positive (right) IMF B_z . (Abe et al., 2004)

Figure 20: Averaged active-time ($K_p > 3$) H^+ and O^+ velocities at (a) 3000-5000 km and (b) 7000-9000 km altitude as a function of solar zenith angle for $F_{10.7} > 100$ (Abe et al., 2004)

Figure 21: Estimated H^+ (top), He^+ (middle) and O^+ (bottom) polar wind ion temperatures from 13 Akebono orbit passes as a function of altitude (left), magnetic local time (middle), and invariant latitude (right) (Drakou et al., 1997)

Figure 22: Measured electron temperature in a low-altitude (2478–2818 km) orbit pass through the dayside northern polar cap ($> 80^\circ$ invariant, 16–20 MLT) on Akebono as a function of pitch angle. (Yau et al., 1995)

Figure 23: Scatter plot of measured electron temperature in the upward (solid symbols) and perpendicular (open symbols) versus downward temperature below (triangles) and above (squares) 75° invariant in a low-altitude (792-2404 km) dayside (10-18.9 MLT) auroral ($63-78^\circ$ invariant) orbit pass (Yau et al., 1995)

Figure 24: Occurrence histograms of (a) H^+ and (b) O^+ polar wind (from top to bottom) density, parallel velocity, flux, and temperature, and perpendicular temperature observed on POLAR at 5000 km altitude near solar minimum (Su et al., 1998a)

Figure 25: Occurrence histograms of (a) H^+ and (b) O^+ polar wind (from top to bottom) density, parallel velocity, flux, and temperature, and perpendicular temperature observed on POLAR at 50,500 km altitude near solar minimum (Su et al., 1998a)

Figure 26: H^+ polar wind full-width-half-maximum (FWHM) energy and pitch angle range observed on POLAR at 5000 km altitude as a function of invariant latitude and MLT (Huddleston et al., 2005)

Figure 27: Integrated H^+ and O^+ ion outflow rates over all MLT and invariant latitudes in the high-latitude ionosphere near solar minimum as a function of K_p . squares: low-energy rate on Akebono below 9000 km, triangles: suprathermal energy rate on DE-1 above 16000 km, diamonds: suprathermal energy rate on POLAR below 9000 km (Cully et al., 2003)

Table 1 – Summary of Polar Wind Model Predictions and Experimental Verification

Model Prediction	Reference	Experimental Evidence / Comments	Reference
<i>A. Collisionless Kinetic Model Predictions</i>			
1 Composition transition altitude: Transition from O ⁺ to H ⁺ as major ion species above 5500 km	Lemaire and Scherer 1972a, b	Transition altitude above at least 4000 km on DE-1 near solar maximum; and at/near 5000 km on POLAR near solar minimum	Chandler et al. 1991; Su et al. 1998
2 Ambipolar electric field amplitude: Electric field decreases from ~0.5 μV/m at “baropause” to <0.02 μV/m at higher altitude; potential difference (1.7 V) results in H ⁺ ions at supersonic speed below ~10,000 km	Lemaire and Scherer 1971; Figure 1	H ⁺ mach number ~ 1.5 at 5000 km on POLAR; ~1 at 5000 km and 1.5–4 above 7000 km on Akebono	Su et al. 1998; Drakou et al. 1998
<i>B. Moments-Based Model Predictions</i>			
3 Transition from subsonic to supersonic flow: H ⁺ ion flow becomes supersonic above H ⁺ -O ⁺ collision region	Banks 1968; Marubashi 1970	The H ⁺ -O ⁺ collision frequency depends on the local ion density and temperature, as does the transition altitude from the collisional to the collisionless region. Definitive experimental test requires simultaneous ion density, temperature, and velocity altitude profiles.	
4 Effects of convection: Convection increases H ⁺ and O ⁺ densities and temperatures and decreases H ⁺ velocity	Raitt et al 1975, 1977	No definitive experimental test yet; however, evidence exists of ion acceleration at high altitude due to strong convection (see #13 below)	
5 Effects of thermal diffusion and diffusion thermal heat flow: Downward thermal diffusion increases H ⁺ density and reduces H ⁺ temperature and upward flow. Diffusion thermal heat flow cools topside H ⁺ .	Schunk and Walker 1970a, 1970b	No definitive experimental test yet; heat flow measurement difficult to make in topside ionosphere.	
6 Helium polar wind: He ⁺ flux varies with neutral atmospheric helium density primarily; He ⁺ velocity is non-negligible above collision-dominated altitudes	Raitt et al. 1978	Factor of ~10 seasonal variation in He ⁺ flux observed on ISIS-2 and DE-1 associated with atmospheric helium and nitrogen density variations; non-negligible He ⁺ velocity (≥1 km/s) observed on ISIS-2, DE-1 and Akebono above 1400–2000 km.	Hoffman and Dobson 1980; Chandler et al., 1991
<i>C. Generalized Transport-Equations Based Model Predictions</i>			
7 Ion temperature anisotropy: For H ⁺ , temperature anisotropy is absent below 2500 km; parallel-to-perpendicular temperature ratio > 1 at high altitude	Schunk and Watkins 1983	T _∥ < T _⊥ at 5000 km; T _∥ > T _⊥ at 50,500 km; region of T _∥ < T _⊥ not predicted.	Su et al. 1998
8 Electron temperature anisotropy: Direction of electron temperature anisotropy depends on upper	Ganguli and Palmadesso 1987	T _∥ > T _⊥ in sunlit polar wind at 2000–3000 km; T _∥ = T _⊥ in non-sunlit polar wind	Yau et al. 1995

	boundary conditions			
9	Supersonic flow at high altitudes: H ⁺ velocity as large as 16-20 km/s and Mach number in the range of 2.5–4 at/below 12,000 km	Ganguli et al. 1987; Demars and Schunk 1989	H ⁺ Mach number of ~1.5–4 observed above 7000 km on Akebono and ~2–7 observed at 50,500 km on POLAR	Drakou et al., 1998; Su et al., 1998a
10	H⁺/He⁺ composition: H ⁺ is dominant ion in supersonic flow; He ⁺ is dominant in subsonic flow	Demars and Schunk 1994	Observed polar wind on DE-1, Akebono, and POLAR predominantly supersonic and H ⁺ or O ⁺ dominant at high altitude.	Abe et al., 1993; Su et al. 1998

D. Collisional Kinetic Model Predictions

11	Effects of Coulomb collisions: Coulomb collision frequency is strongly velocity dependent; this results in slower thermalization of higher-energy particles and the evolution of H ⁺ ions into a double-humped distribution at 1000–2000 km (or higher) altitude	Barakat et al., 1995; Pierrard and Lemaire 1998; Tam et al., 1998; Figure 2	No definitive experimental test yet: Test requires measurement of detailed ion velocity distribution function.	
----	--	---	--	--

E. Non-classical Polar Wind Model Predictions

12	Wave particle interaction: Perpendicular ion heating followed by magnetic mirroring in Earth's divergent magnetic field enhances heavy (O ⁺) ion escape	Barakat and Barghouthi 1994	Evidence of ion acceleration at lower altitude, both episodic and statistical, in observed O ⁺ polar wind ions on DE-1, Akebono and POLAR	Gurgiolo and Burch 1982; Su et al., 1998a
13	Centrifugal acceleration: Strong E × B convection in regions of curved magnetic field produces significant parallel ion acceleration at high altitude	Cladis 1986; Horwitz et al. 1994	Observed low-energy O ⁺ ions on DE-1, Akebono and POLAR up to 50,500 km can be attributed in part to centrifugal acceleration.	Su et al., 1998a; Elliott et al., 2001
14	Convection: Convection of ions through different regions of the high-latitude topside ionosphere subjects polar wind ions through a time-dependent force field and at times accelerates ions to polar wind altitude.	Schunk and Sojka 1989, 1997	Evidence of active-time convection electric field map that is consistent with flux tube transport in and out of the polar cap	
15	Effect of elevated electron temperature: Increase in electron temperature to 10,000 K increases O ⁺ velocity to a few km/s	Barakat and Schunk 1983	Both O ⁺ flow velocity of 1-4 km/s and electron temperature exceeding 5000–7000 K observed at times; no definitive experimental test yet, however	Abe et al., 1993a, 1993b
16	Effect of ion heating: Increase in ion temperature at exobase to 10,000 K increases O ⁺ flux by 5 decades	Li et al. 1988	No definitive experimental test yet: required ion temperature has never been observed at exobase	
17	Effect of hot magnetospheric electrons: Hot electrons develop discontinuity in the electric field and reduce the potential barrier for O ⁺ ions, enhancing their escape.	Barakat and Schunk 1984	No definitive experimental test yet	
18	Effect of atmospheric photoelectrons: Collisions between photoelectrons and thermal electrons increase the electron temperature and result in temperature anisotropy, leading to increased O ⁺ velocity and flux	Lemaire and Scherer 1972b; Tam et al. 1995a, b	Day-night asymmetry in polar wind velocity in favor of the dayside observed on Akebono; electron temperature anisotropy in sunlit polar wind also observed	

Table 2 Summary of Observed Polar Wind Characteristics (a)

A. Data Coverage						
<i>Altitude (km)</i>	<i>Satellite</i>	<i>Epoch</i>	<i>Solar Cycle & Phase (b)</i>	<i>Observed Species</i>	<i>Reference</i>	<i>Notes</i>
1400	ISIS-2	1971–1972	SC20 dec	H ⁺ , He ⁺ , O ⁺ (c)	Hoffman 1980	Magnetically quiet
1000 – 4000	DE-1	1981–1983	SC21 dec	H ⁺ , He ⁺ , O ⁺	Chandler 1991, 1995	
1000 – 10,000	Akebono	1989–1998	SC22 max – SC23 max	H ⁺ , He ⁺ , O ⁺ , e ⁻	Abe 1993, 2004, Yau 1995	
5000 – 6000	POLAR	1996	SC23 min	H ⁺ , O ⁺	Su 1998, Huddleston 2005	Magnetically quiet
7000 – 23,300	DE-1	1981–1982	SC21 dec	e ⁻	Persoon 1983	
50,500	POLAR	1996	SC23 min	H ⁺ , He ⁺ , O ⁺	Su 1998, Elliott 2001	
B. Average Characteristics						
<i>Altitude (km)</i>	<i>Velocity v (km/s) (d)</i>		<i>Temperature (eV)</i>	<i>Flux F (cm⁻² s⁻¹)</i>	<i>Density n (cm⁻³)</i>	<i>Mach Number M</i>
1400	H ⁺	1.0 to 2.5 (S); 0.5 to 4 (W)	-	(3–7) × 10 ⁷ (W) to 7 × 10 ⁷ (S)	50 (S) to 20–30 (W)	-
	He ⁺	0.5 to 2.0 (S); 0 to 2 (W)	-	1.5 × 10 ⁶ (S) to (1–2) × 10 ⁷ (W)	10–20 (S) to 100–200 (W)	-
	O ⁺	-	-	-	100–2000 (W) to 1 × 10 ⁴ (S)	-
1000 – 4000	H ⁺	3 to 12 (S); 3 to 9 (W)	-	5 × 10 ⁷ (S) – 1.5 × 10 ⁸ (V)	30–150; H ⁺ /O ⁺ ~ 0.05	-
	He ⁺	1 to 3 (S); 0.5 to 4.5 (W)	-	1 × 10 ⁶ (S) – 2 × 10 ⁷ (W)	8–70; He ⁺ /O ⁺ ~ 0.02	-
	O ⁺	-2 to 2	-	~ 0	700–2500	~ 0
1000 – 10,000	H ⁺	0 – 12	0.05 – 0.35	~1 × 10 ⁷ to 2 × 10 ⁸ (@ 2000 km)	-	~1.5–4 (>7000 km)
	He ⁺	0 – 7	0.05 – 0.35	-	-	~1.5 – 1.8 (>7000 km)
	O ⁺	0 (<4000 km) – 4	0.05 – 0.35	~7 × 10 ⁶ to 1 × 10 ⁸ (@ 2000 km)	-	~5 – 7 (>7000 km)
	e ⁻	-	0.3 – 0.7	-	-	-
5000 – 6000	H ⁺	15 (10 – 21)	T =0.12, T _⊥ =0.23	1.2 × 10 ⁷ (10 ⁵ – 10 ⁸) (e)	10 (<0.1 – 100)	1.5
	O ⁺	-0.9 (-3 to 2)	T =0.34, T _⊥ =0.61	7.4 × 10 ⁵ (down), 9.5 × 10 ⁵ (up)	7.7 (<0.1 – 100)	-0.1
7000 – 23,300	e ⁻	-	-	-	1 – 30; ∝ R ^{-3.85}	-
50,500	H ⁺	45 (20 – 110)	T =1.7, T _⊥ =1.1	1.2 × 10 ⁶ (10 ⁵ – 10 ⁷)	0.3 (0.01 – 2)	4.6 (2 – 7)
	He ⁺	25 (8 – 63)	T =3.0, T _⊥ =1.5	2.5 × 10 ⁴	0.012 (0.001 – 1)	~2.5
	O ⁺	17 (8 – 32)	T =7.5, T _⊥ =3.4	8.3 × 10 ⁴	0.05 (0.001 – 0.3)	3.5 (1 – 8)

C. Variability

<i>Altitude (km)</i>		<i>Local Time (f)</i>	<i>Solar Activity ($F_{10.7}$)</i>	<i>Season</i>	<i>Magnetic Activity (K_p)</i>	<i>SZA / Other</i>
1400	H ⁺	-	-	F : S:W ~ 1-2.5 : 1	-	-
	He ⁺	-	-	F : S:W ~ 1 : 10	-	-
	O ⁺	-	-	-	-	-
1000 – 4000	H ⁺	-	v : high/low $F_{10.7}$ ~ 1.3 n : no significant trend	F : V:S:F:W ~ 15 : 5 : 8 : 6 v : S:W ~ 1.3-1.7 : 1 n : S:W ~ 1 : 2 (<2000 km)	F : high/low K_p ~ 3; insignificant compared with standard deviation	-
	He ⁺	-	n : no significant trend	F : V:S:F:W ~ 10 : 1 : 6 : 20 v : S:W ~ 0.8 : 1 n : S:W ~ 1 : 10 (<2000 km)	-	-
	O ⁺	-	n : high/low $F_{10.7}$ ~ 2	n : S:W ~ 1.5-3 : 1		v < 0 for B_z < 0; v > 0 for B_z > 0
1000 – 10,000	H ⁺	D: 0-12 N: 0-7	v : high/low $F_{10.7}$ ~ 0.5-1 Larger (smaller) gradient at low (high) altitude at high $F_{10.7}$	v : S:E:W ~ 2-3 : 2 : 1	F : weak dependence on K_p v : more variable at high K_p	v : decrease with SZA above 100°; v : larger for B_z > 0
	He ⁺	D: 0-6 N: 0-4		-	-	F : increase with B_z (>0)
	O ⁺	D: 0-4 (>4000 km) N: 0-3 (>6000 km)	v : (same as in H ⁺)	v : S:E:W ~ 2 : 2 : 1	F : weak dependence on K_p v : more variable at high K_p	v : (same as in H ⁺); F : (same as in H ⁺)
	e-	D: T_{up}/T_{\perp} ~ 1.5-2 N: T_{up}/T_{\perp} ~ 1	-	-	-	-
5000 – 6000	H ⁺	-	-	-	-	n : 10-fold H ⁺ and 100- fold O ⁺ decrease w/ SZA
	O ⁺	-	-	-	-	
7000 – 23,300	e-	-	-	-	-	-
50,500	H ⁺ :	-	-	-	-	-
	He ⁺	-	-	-	-	-
	O ⁺	-	-	-	-	-

(a) Statistical studies and surveys using data from 10 or more satellite orbit passes only; does not include episodic studies

(b) SC = Solar Cycle; Phase: asc = ascending, dec = declining, min = solar minimum, max = solar maximum

- (c) O⁺ density only
- (d) S = summer; W = winter; V = spring (vernal equinox), F = fall (autumn equinox); E = equinox
- (e) Su et al. (1998); revised flux estimate in Huddlestone (2005): $6 \times 10^7 \text{ cm}^{-2} \text{ s}^{-1}$
- (f) D: dayside; N: nightside

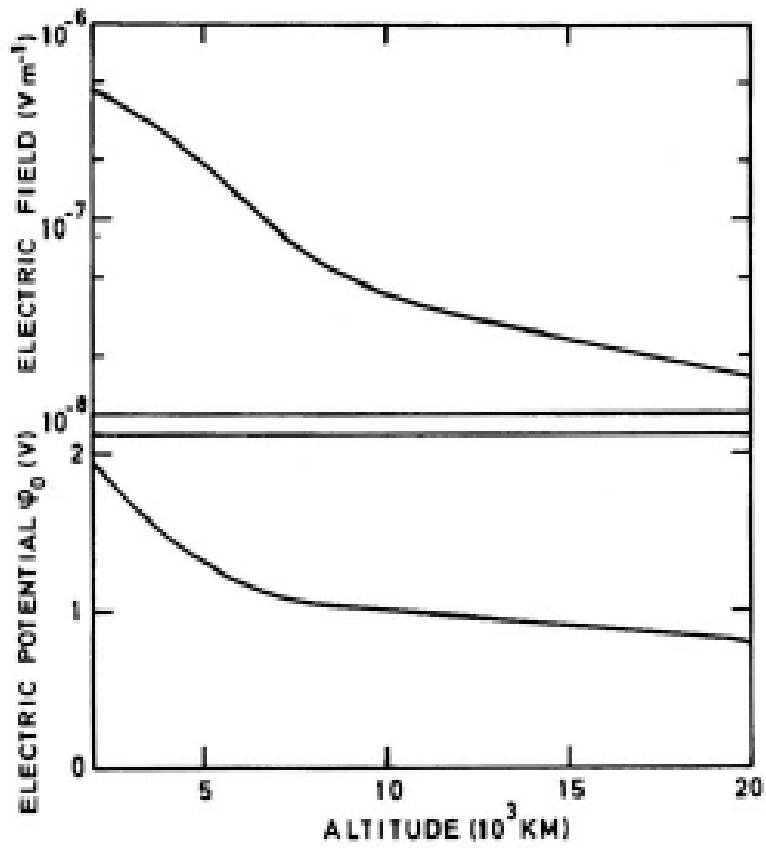


Figure 1: Calculated electric field and electric potential as a function of altitude in the model of Lemaire and Scherer (1971) (from Lemaire and Scherer, 1971)

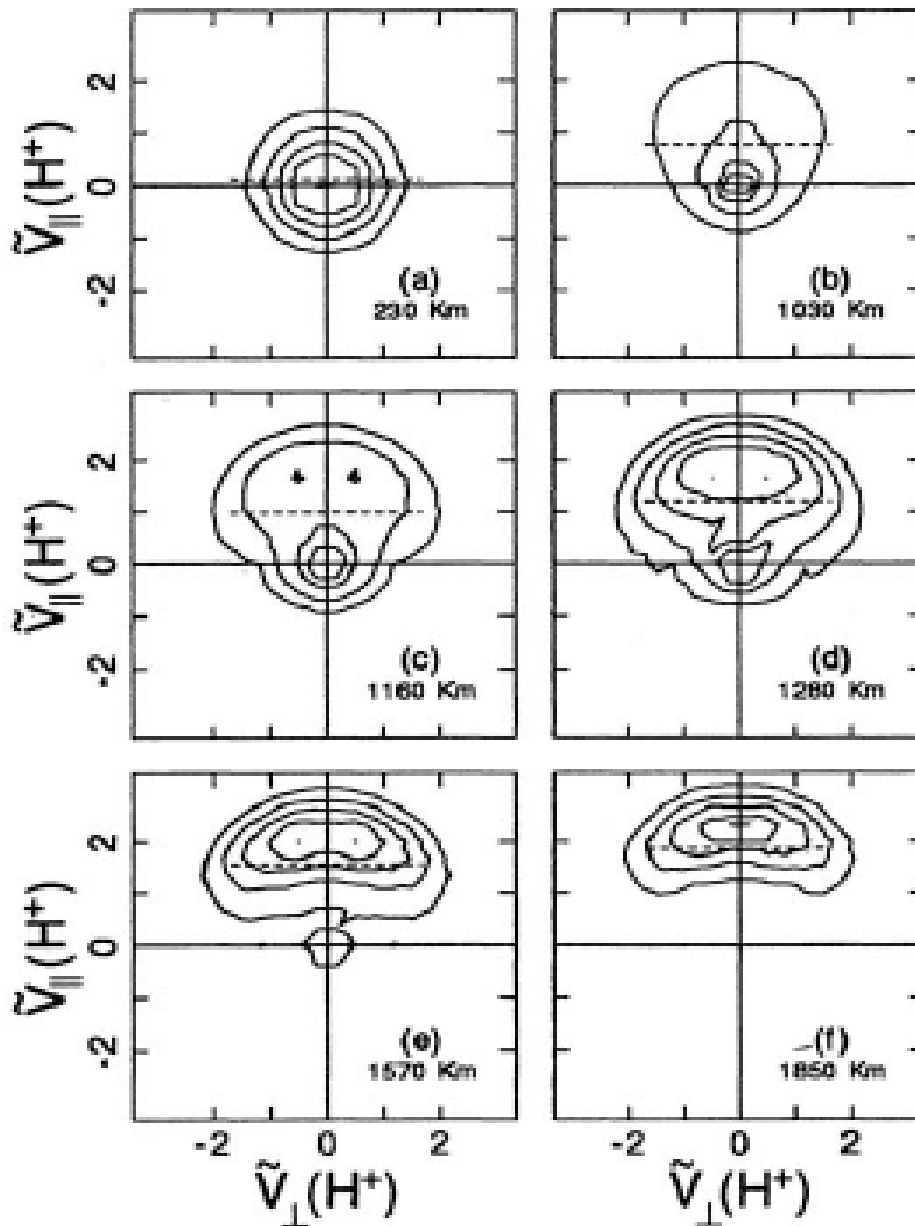


Figure 2: Contour plots of the H^+ velocity distributions at six different altitudes in the collisional kinetic test-particle calculations of Barakat et al. (1995). The velocities v_{\parallel} and v_{\perp} are normalized by the O^+ thermal speed. The dotted line shows the H^+ drift velocity (from Barakat et al., 1995).

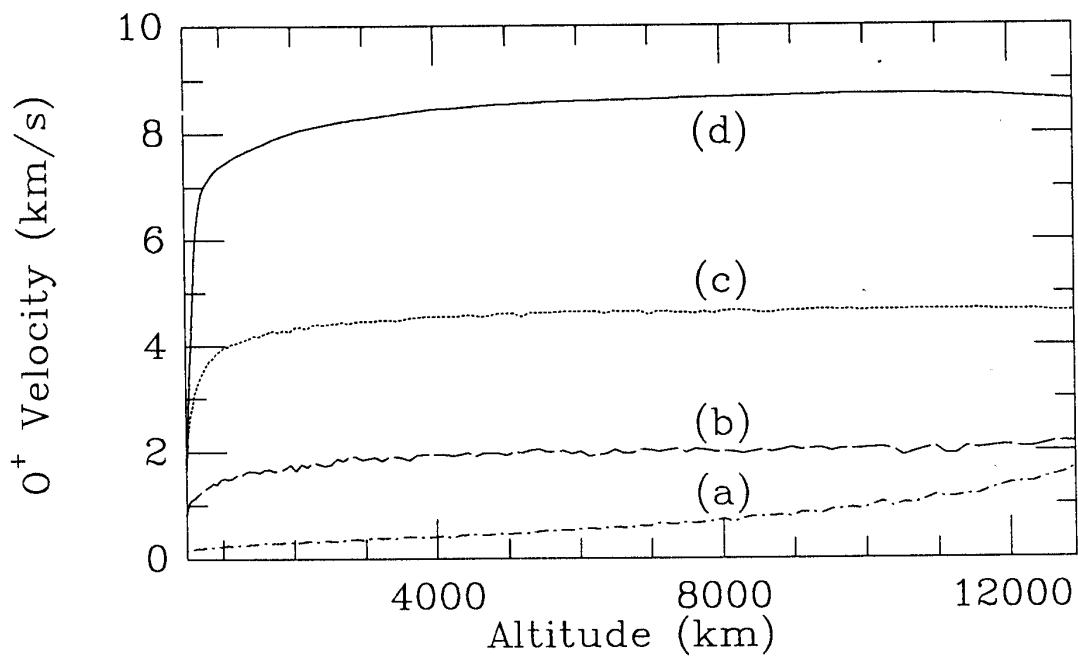


Figure 3: Altitude profile of simulated O^+ polar wind velocity in Tam et al. (1998) for a photoelectron to thermal electron density ratio of (a) 0%; (b) 0.05%, (c) 0.1% , and (d) 0.15% (from Tam et al., 1998, Figure 16)

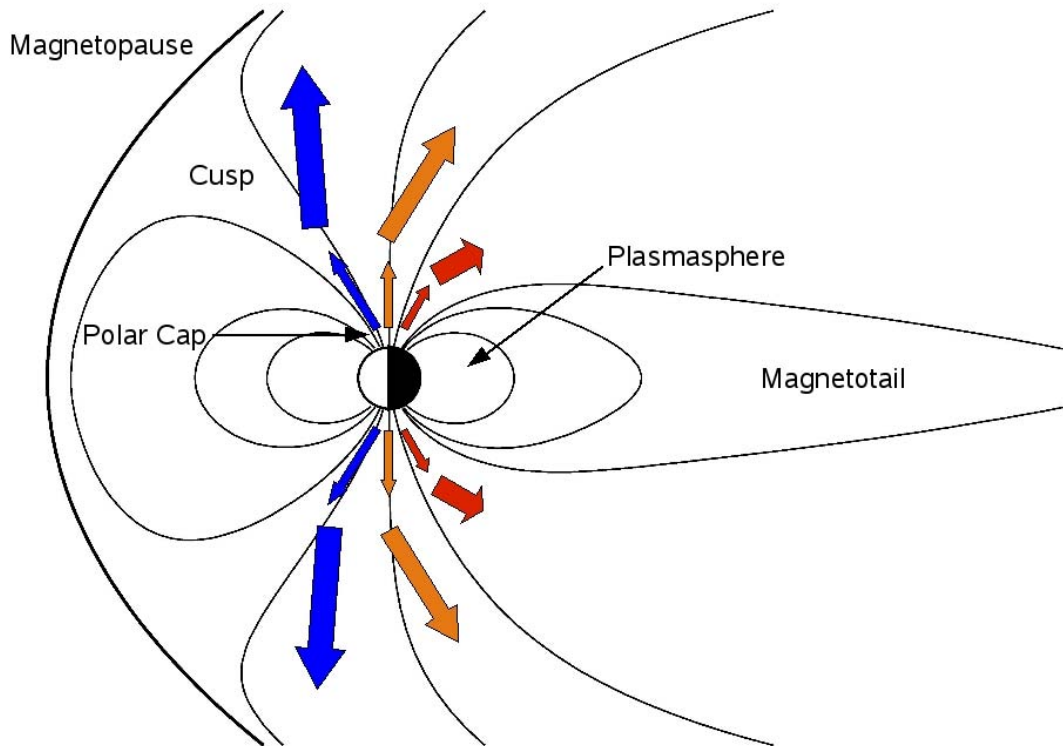


Figure 4: Schematic diagram of polar wind flow in the polar ionosphere: As the polar wind ions flow upward along “open” geomagnetic field lines and undergo anti-sunward convection in the polar cap and dayside cusp poleward of the plasmasphere, they generally increase in both drift speed and temperature. The direction, length, width, and color of the arrows denote the polar wind ion flow direction, speed, temperature, and mass species, respectively.

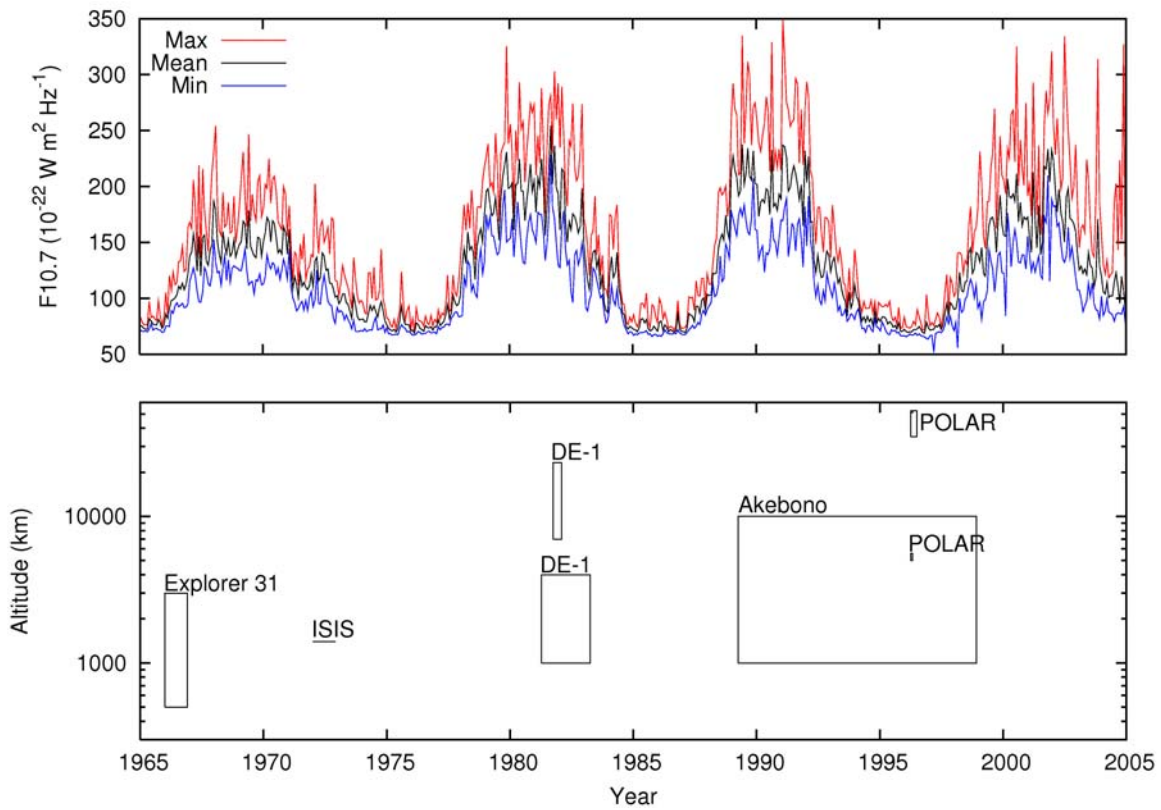


Figure 5: (a) Mean, maximum and minimum solar radio flux $F_{10.7}$ in each 27-day solar rotation from 1965 to 2005 in solar radio flux unit ($1 \text{ sfu} = 10^{-22} \text{ W m}^{-2} \text{ Hz}^{-1}$), and (b) altitude and epoch range of polar wind observations. Note the large variation of $F_{10.7}$ within a solar rotation near solar maximum.

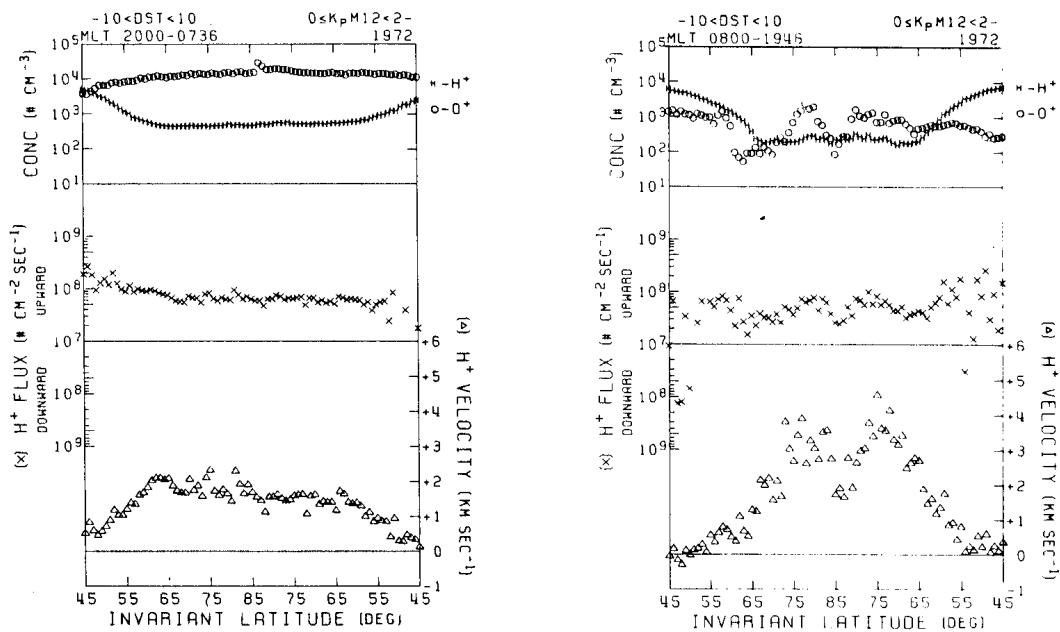


Figure 6: Polar wind H^+ and O^+ ion densities, H^+ ion flux, and H^+ ion velocity (from top to bottom) observed on ISIS-2 at 1400 km in 1971–1972 in the early declining phase of SC 20, near summer solstice (left) and winter solstice (right). (Hoffman and Dobson, 1980)

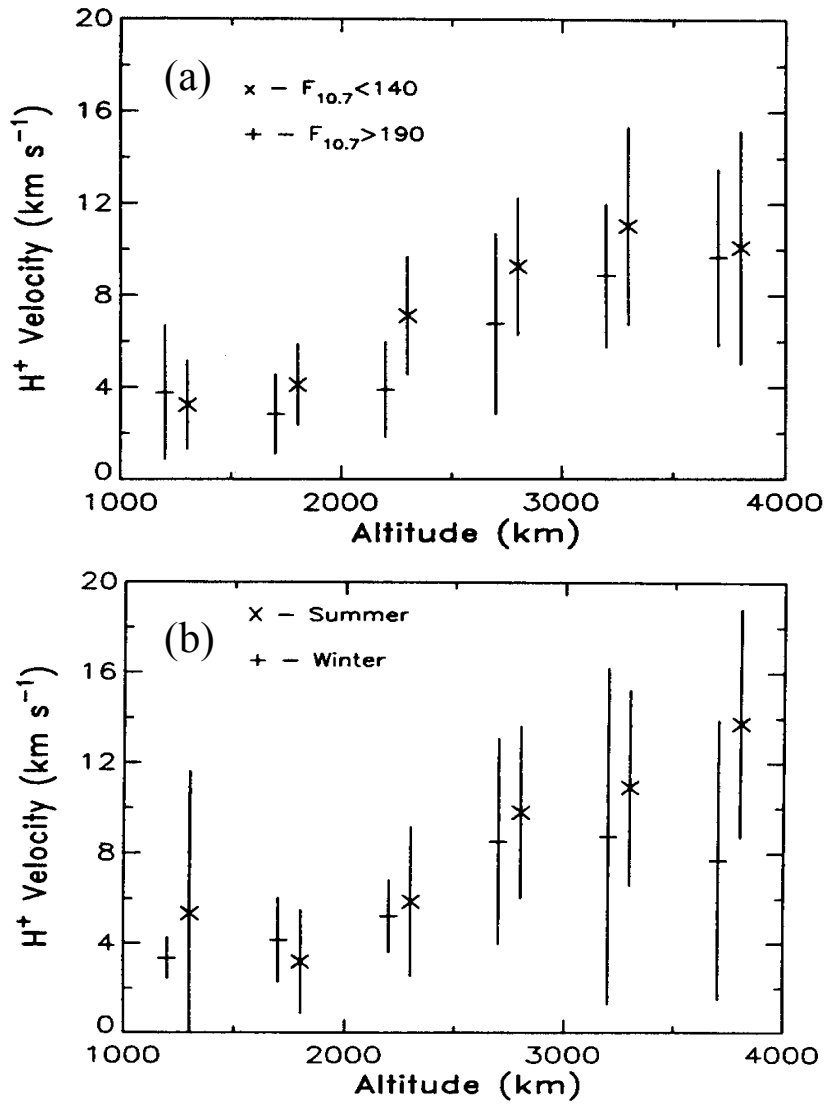


Figure 7: Averaged polar wind H⁺ ion velocity observed on DE-1 in 1981–1983 in the early declining phase of SC 21 as a function of altitude, (a) for high and low solar radio flux ($F_{10.7} > 190$ and $F_{10.7} < 140$, respectively), and (b) for summer and winter (Chandler et al., 1991)

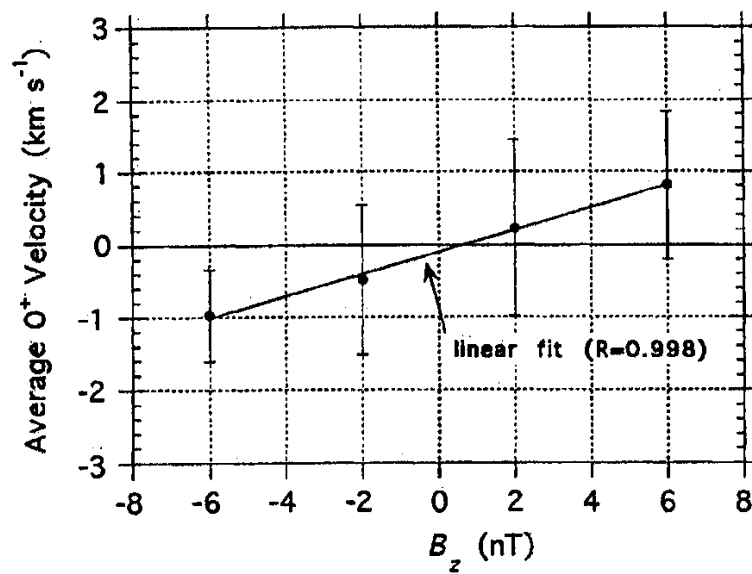


Figure 8: Averaged polar wind O^+ ion velocity observed on DE-1 in 1981–1983 in the early declining phase of SC 21 between 2000 and 4000 km as a function of IMF B_z . (Chandler et al., 1995)

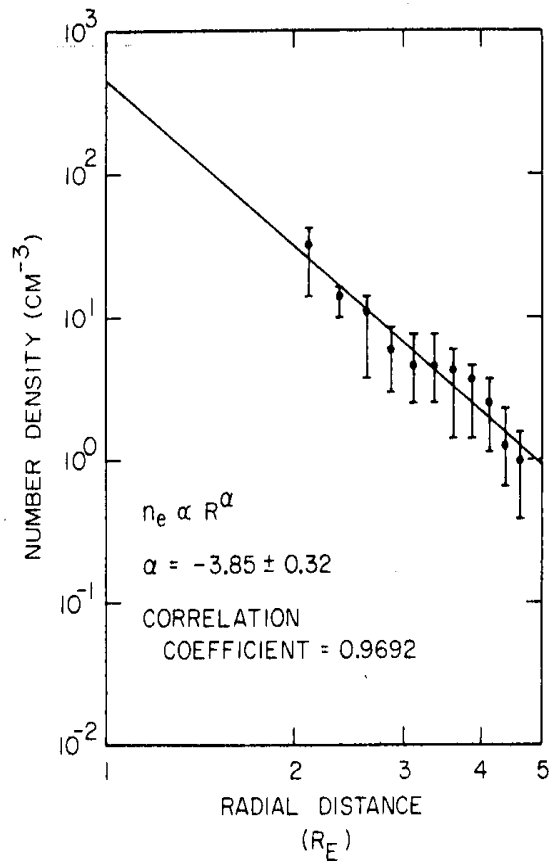


Figure 9: Median plasma density as a function of geocentric distance in the high-altitude polar cap ionosphere derived from DE-1 PWI data in 1981–1982 (Persoon et al., 1983)

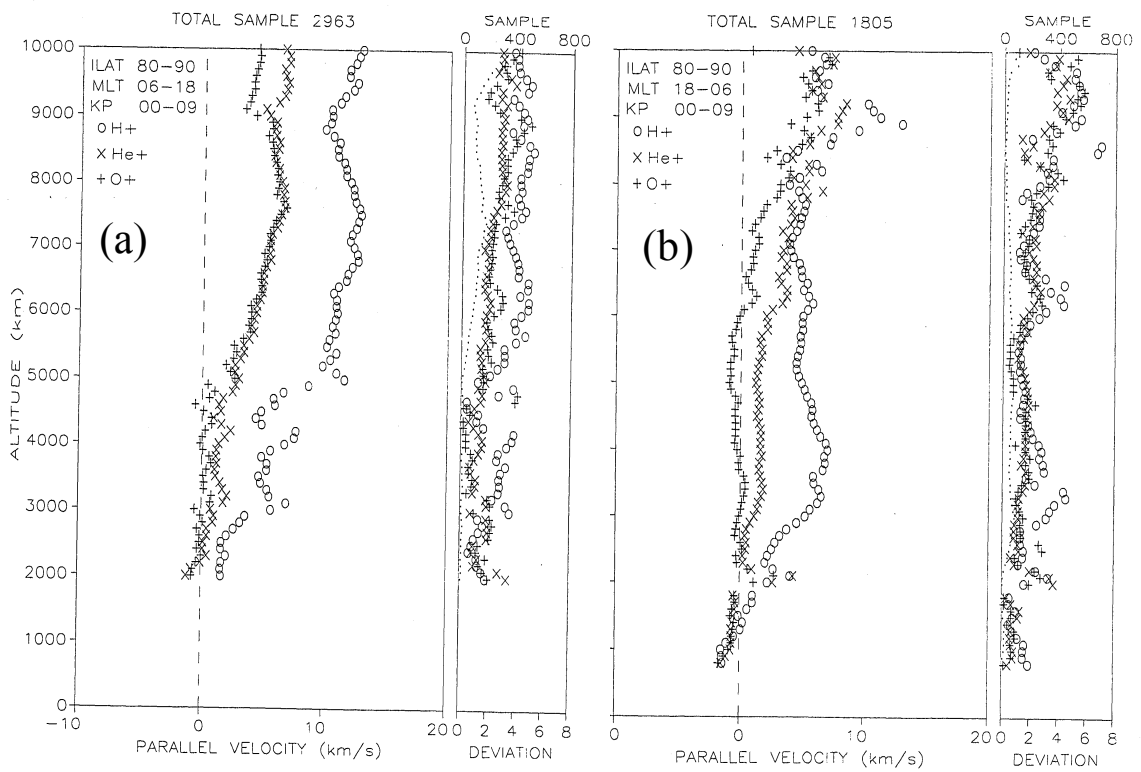


Figure 10: Averaged polar wind H⁺ ion velocity (left panel) and standard deviation (right panel) observed on Akebono in 1990–1992 near the maximum of SC 22 as a function of altitude, in the (a) dayside and (b) nightside, respectively (Abe et al., 1993a)

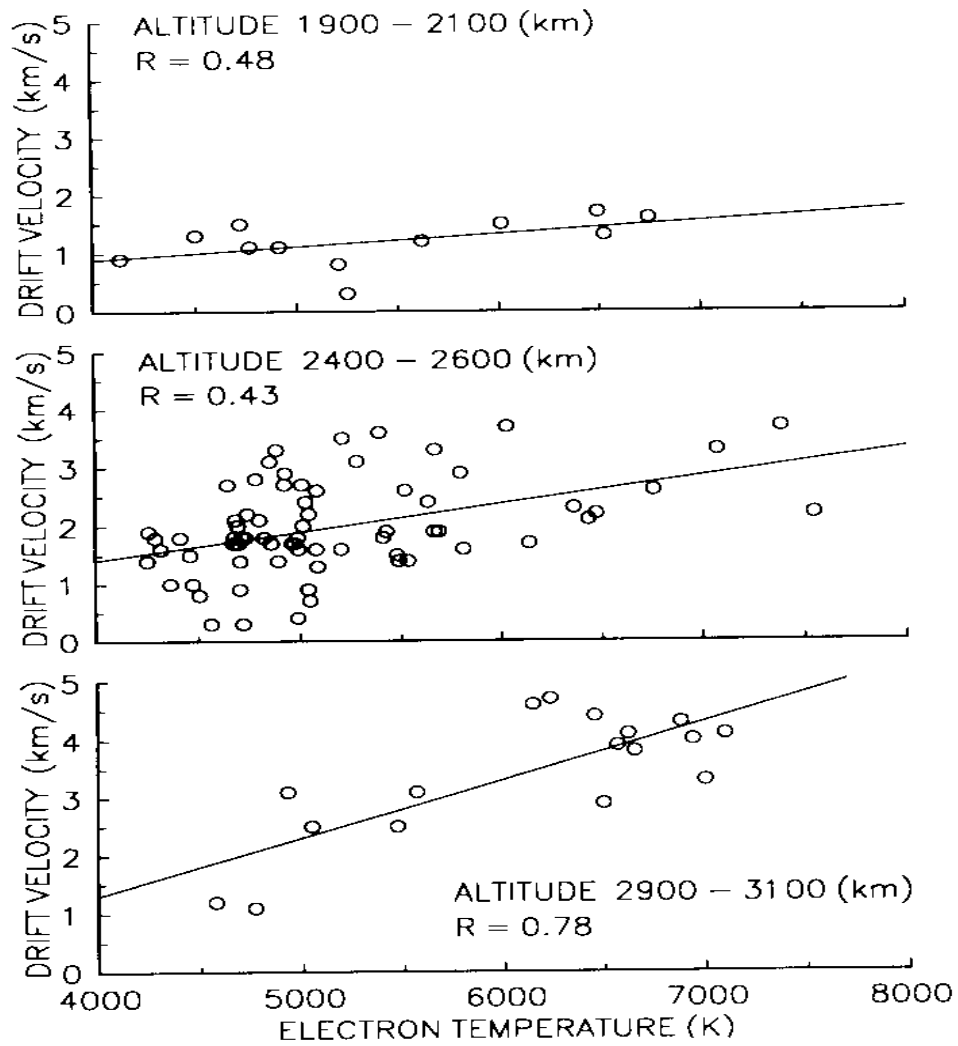


Figure 11: Scatter plot of H^+ polar wind ion velocity versus electron temperature observed on Akebono at (a) 2000 km, (b) 2500 km, and (c) 3000 km. (Abe et al., 1993b)

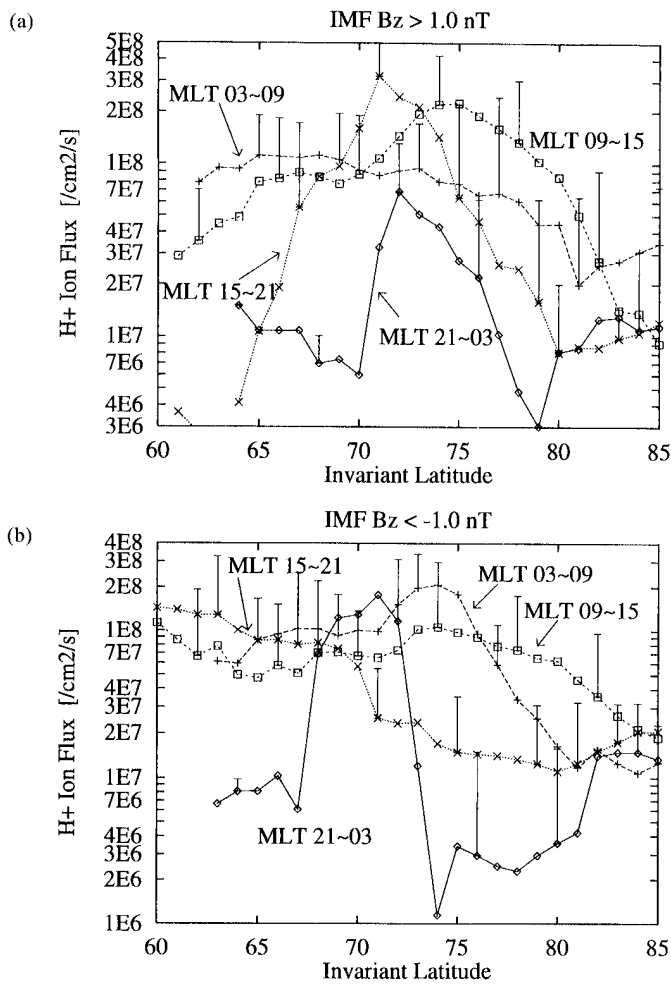


Figure 12: Integrated H⁺ ion flux per unit area observed at 6000–9000 km on Akebono and normalized to 2000 km altitude for each MLT sector as a function of invariant latitude under (a) northward (IMF B_z > 1 nT) and (b) southward (IMF B_z < -1 nT) (Abe et al., 1996)

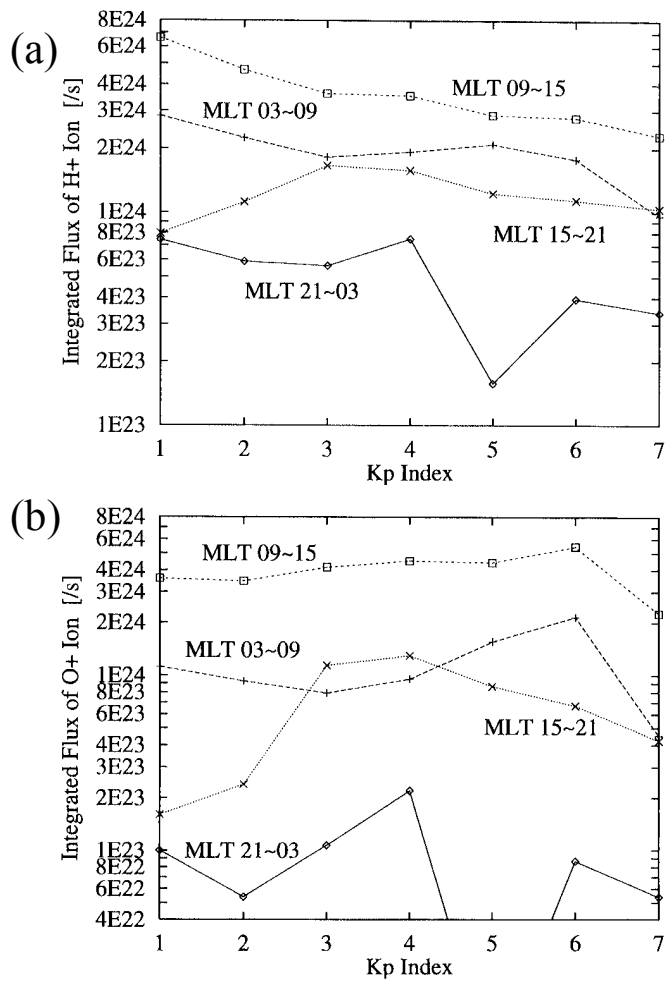


Figure 13: Integrated ion flux observed at 6000–9000 km on Akebono for each MLT sector as a function of the Kp index: (a) H⁺, and (b) O⁺ (Abe et al., 1996)

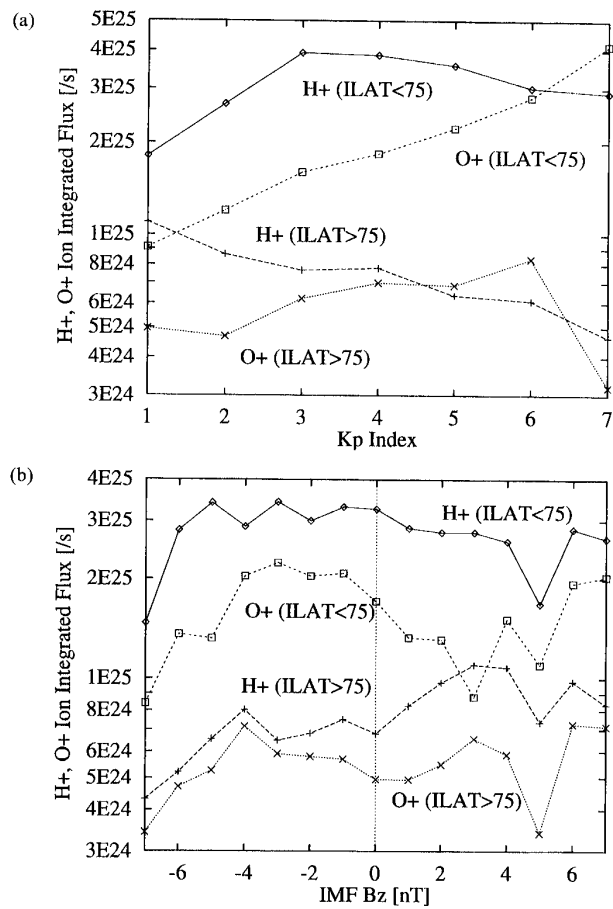


Figure 14: Integrated H⁺ and O⁺ ion flux observed at 6000–9000 km on Akebono above and below 75° invariant as a function of (a) the Kp index and (b) IMF Bz (Abe et al., 1996)

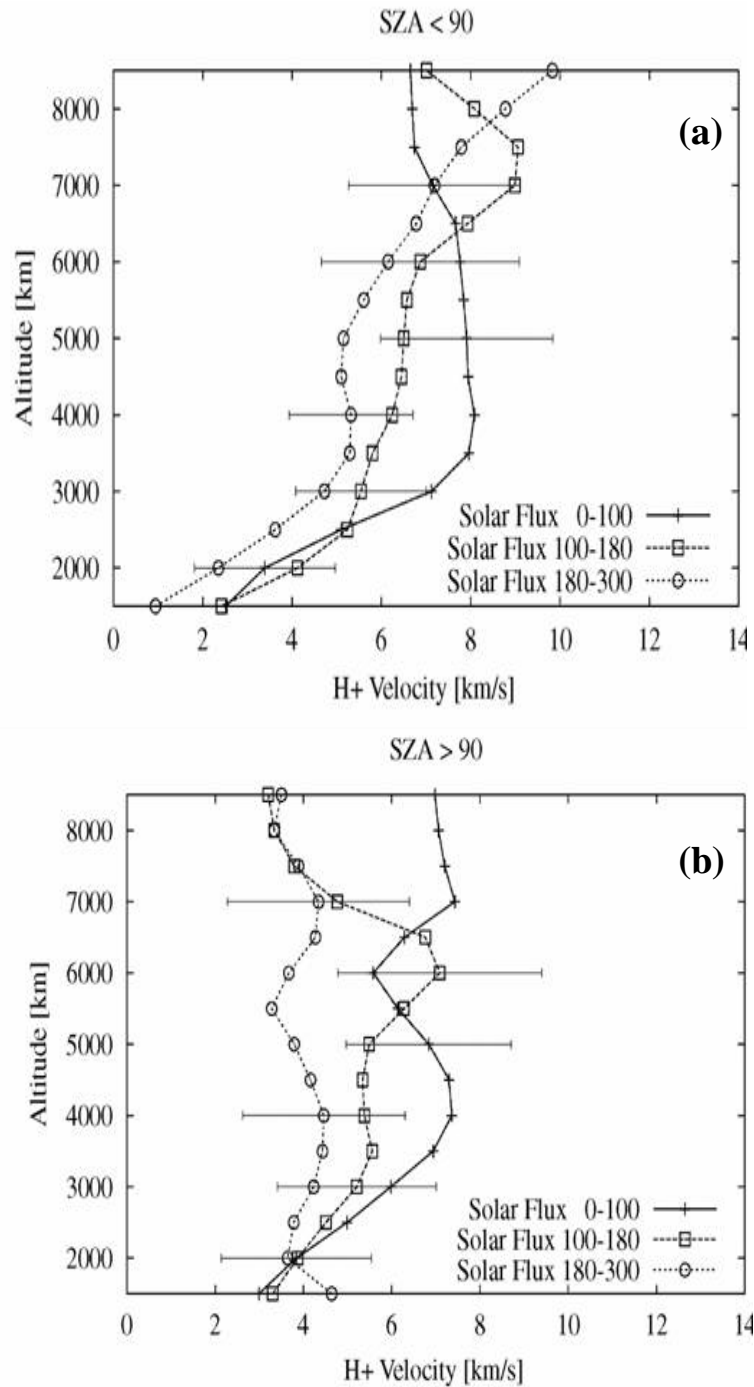


Figure 15: (a) Sunlit ($SZA < 90^\circ$) and (b) non-sunlit ($SZA > 90^\circ$) averaged H^+ velocity observed on Akebono as a function of altitude for different levels of solar radio flux ($F_{10.7}$) (Abe et al., 2004)

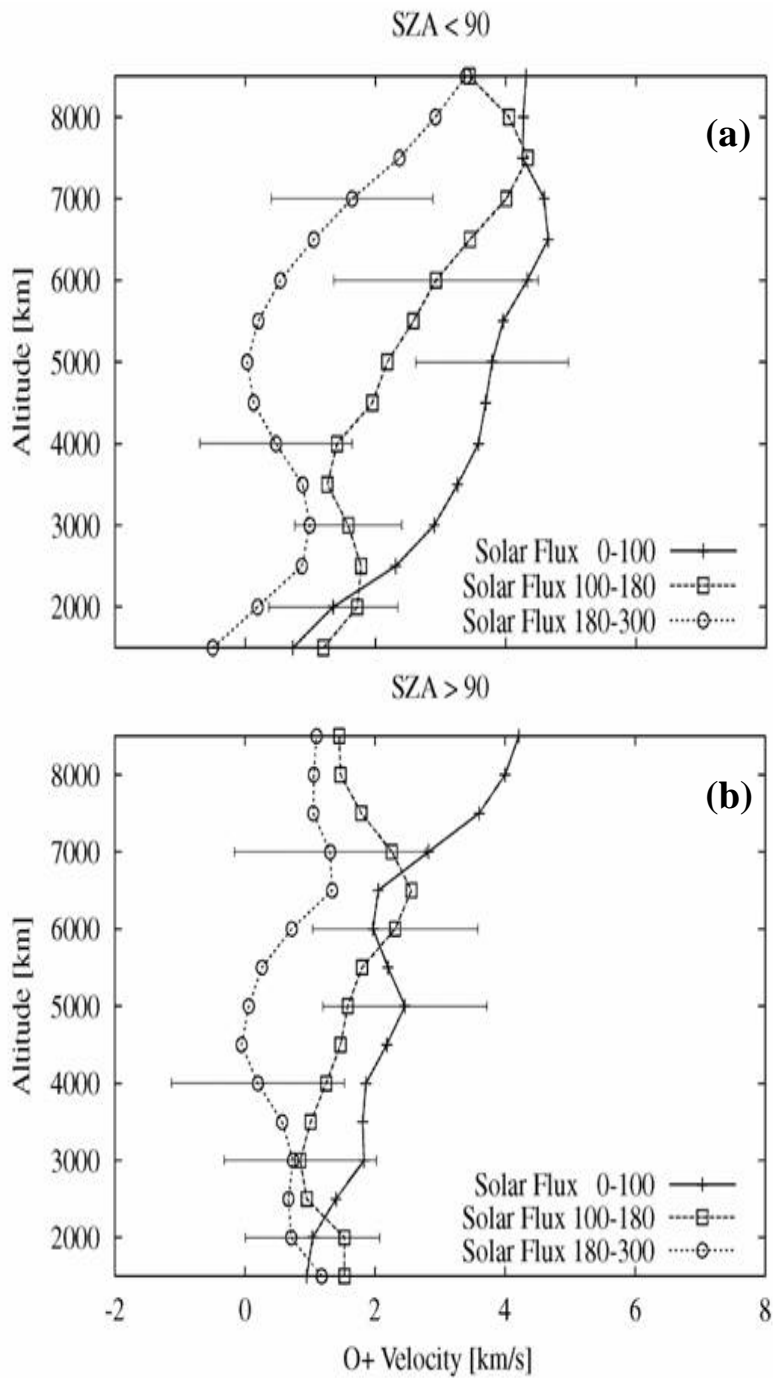


Figure 16: (a) Sunlit ($SZA < 90^\circ$) and (b) non-sunlit ($SZA > 90^\circ$) averaged O^+ velocity observed on Akebono as a function of altitude for different levels of solar radio flux ($F_{10.7}$) (Abe et al., 2004)

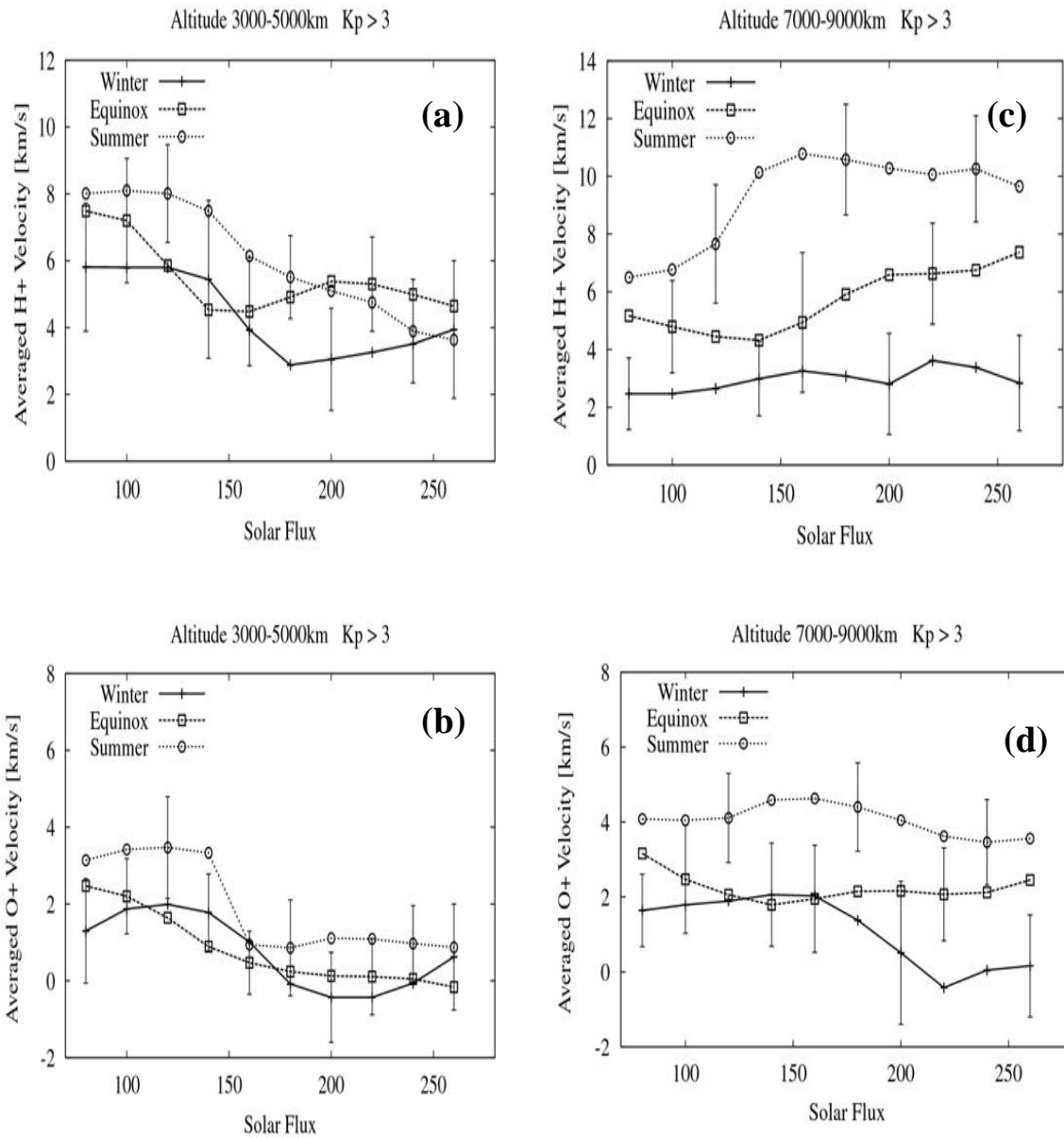


Figure 17: Averaged active-time ($K_p > 3$) (a) H^+ and (b) O^+ velocity at 3000-5000 km altitude and (c) H^+ and (d) O^+ velocity at 7000-9000 km altitude observed on Akebono as a function of solar radio flux ($F_{10.7}$) in different seasons (Abe et al., 2004)

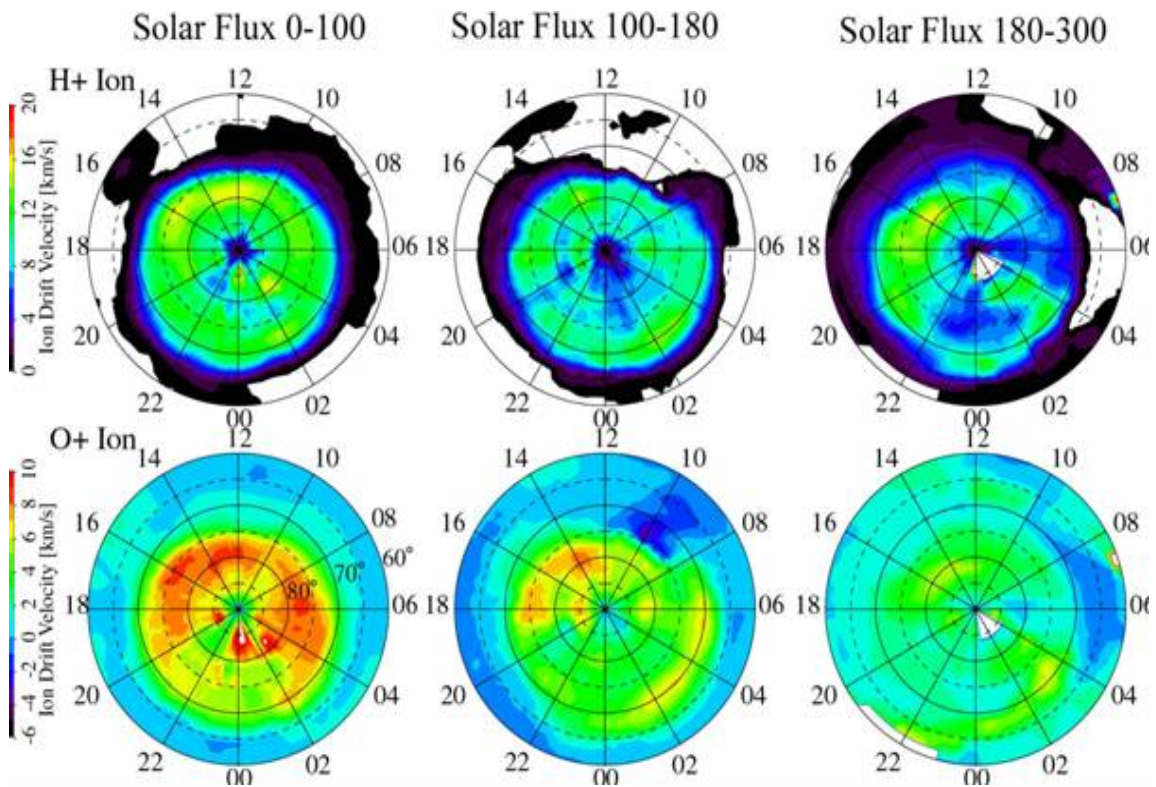


Figure 18: Distribution of averaged quiet-time ($K_p \leq 2$) H^+ and O^+ velocity observed at 6000-8000 km altitude on Akebono for different levels of solar radio flux ($F_{10.7}$) (Abe et al., 2004)

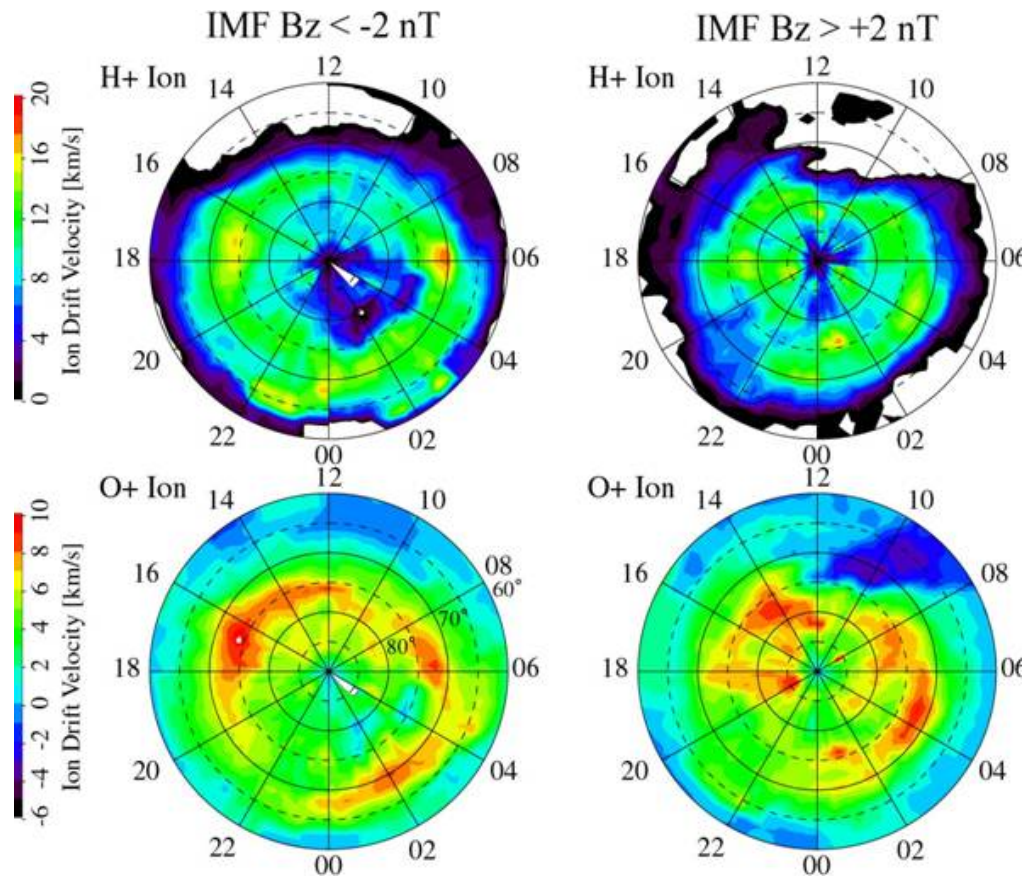


Figure 19: Distribution of averaged H⁺ (top) and O⁺ (bottom) velocity observed at 6000-8000 km altitude on Akebono at low solar flux ($F_{10.7} < 150$) for negative (left) and positive (right) IMF B_z (Abe et al., 2004)

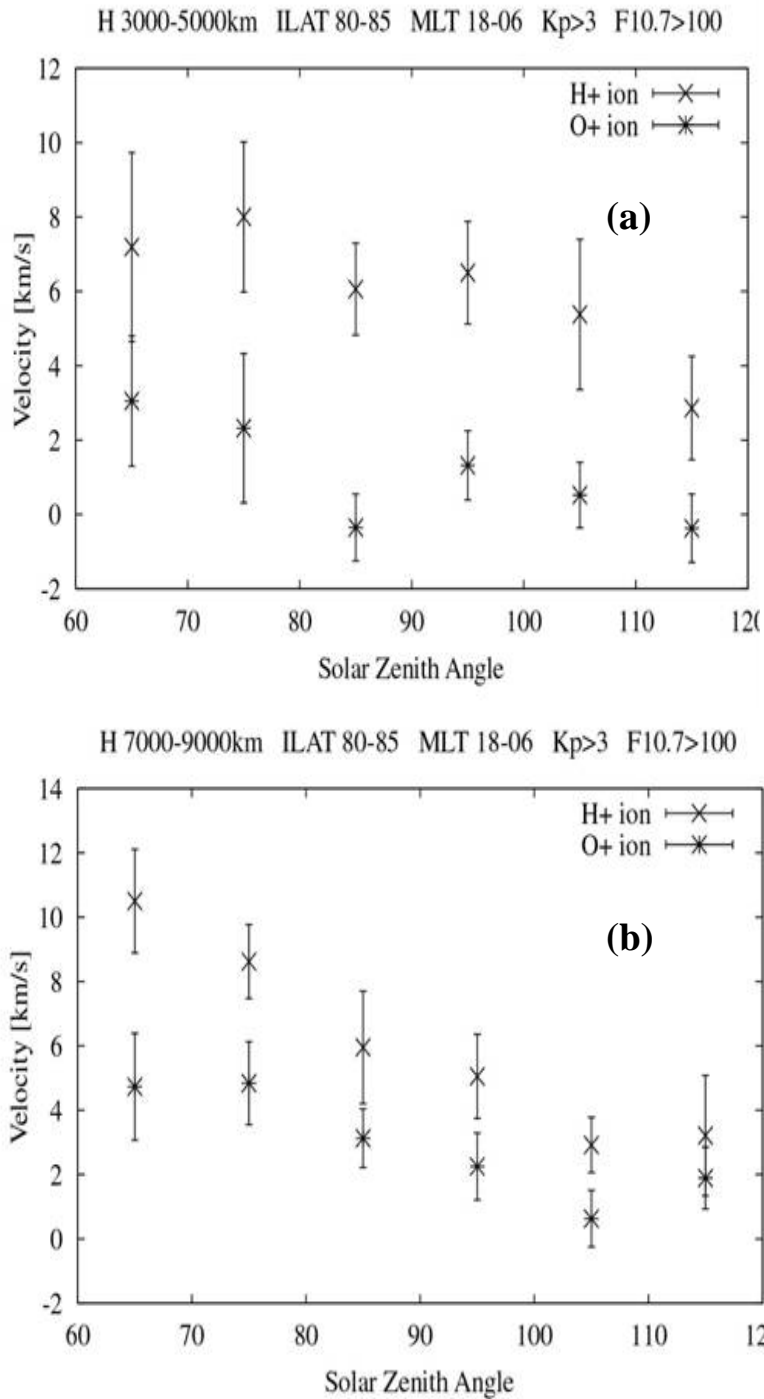


Figure 20: Averaged active-time ($K_p > 3$) H^+ and O^+ velocities at (a) 3000-5000 km and (b) 7000-9000 km altitude as a function of solar zenith angle for $F_{10.7} > 100$ (Abe et al., 2004)

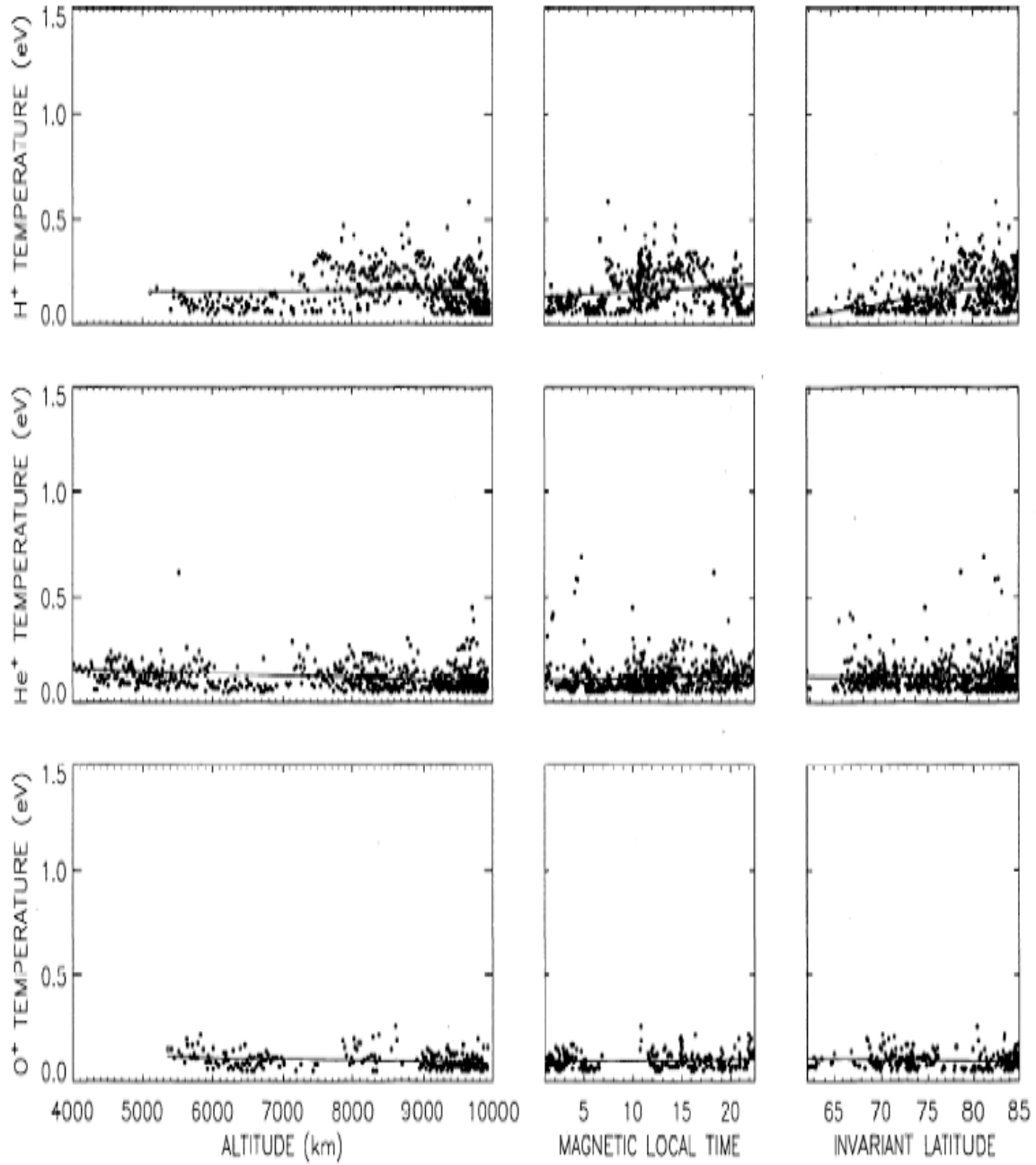


Figure 21: Estimated H⁺ (top), He⁺ (middle) and O⁺ (bottom) polar wind ion temperatures from 13 Akebono orbit passes as a function of altitude (left), magnetic local time (middle), and invariant latitude (right) (Drakou et al., 1997)

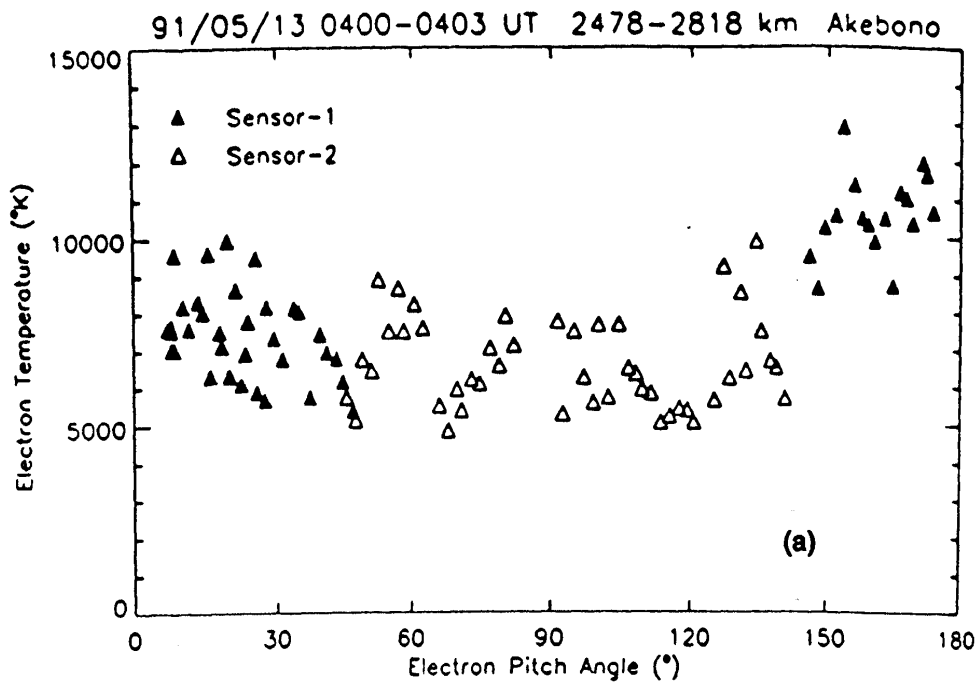


Figure 22: Measured TED electron temperature in a low-altitude orbit pass through the dayside northern polar cap ($>80^\circ$ invariant, 16-20 MLT, 2478-2818 km) on Akebono as a function of pitch angle. (Yau et al., 1995)

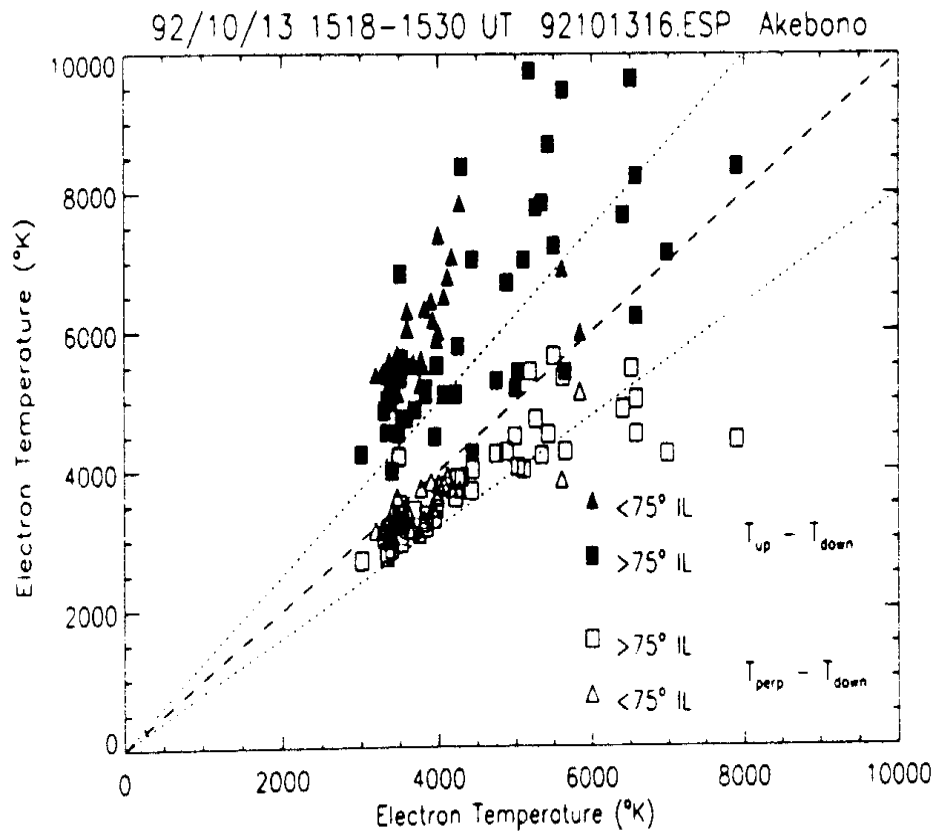


Figure 23: Scatter plot of measured electron temperature in the upward (solid symbols) and perpendicular (open symbols) versus downward temperature below (triangles) and above (squares) 75° invariant in a low-altitude (792-2404 km) dayside (10-18.9 MLT) auroral (63°-78° invariant) orbit pass (Yau et al., 1995)

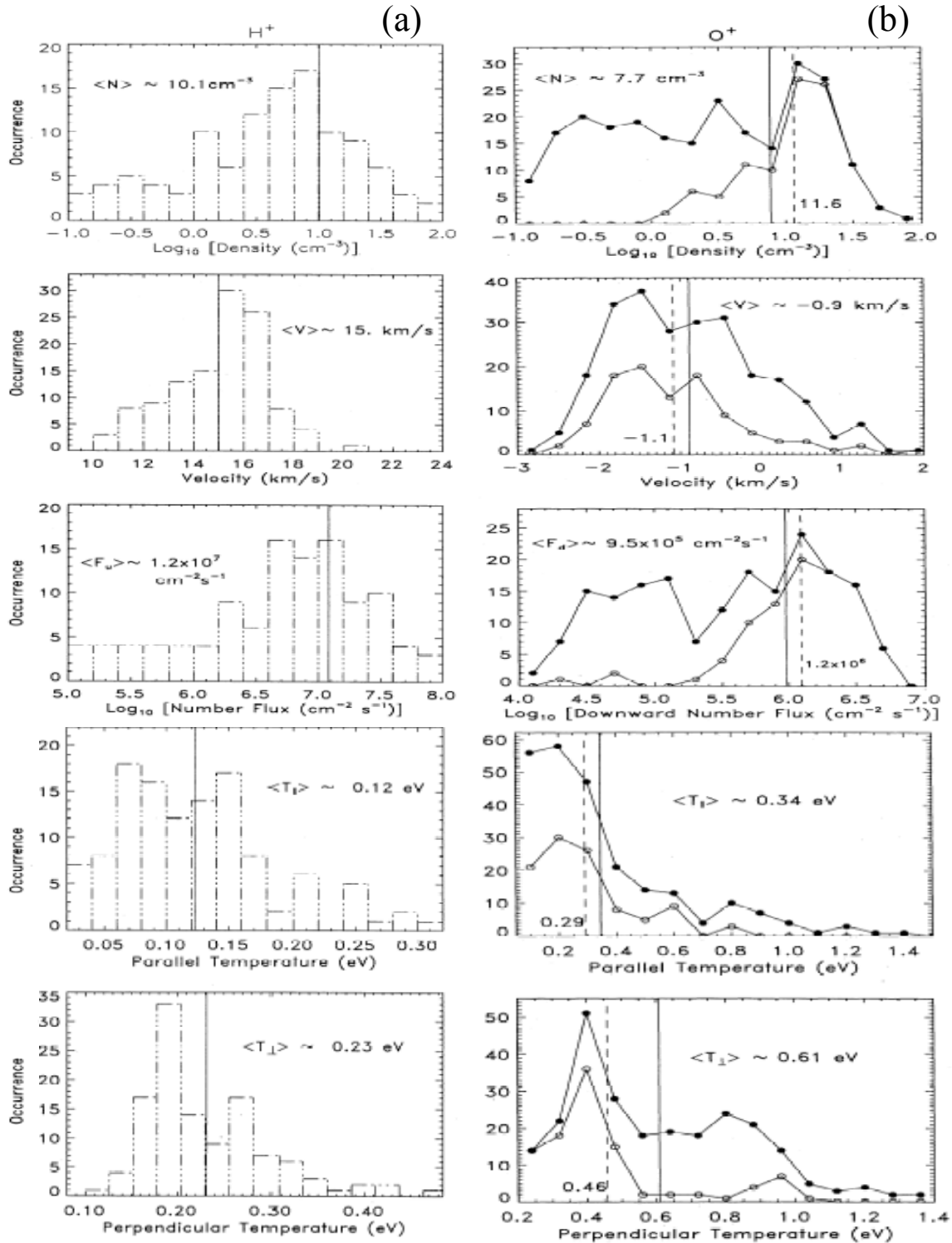


Figure 24: Occurrence histograms of (a) H^+ and (b) O^+ polar wind (from top to bottom) density, parallel velocity, flux, and temperature, and perpendicular temperature observed on POLAR at 5000 km altitude near solar minimum (Su et al., 1998)

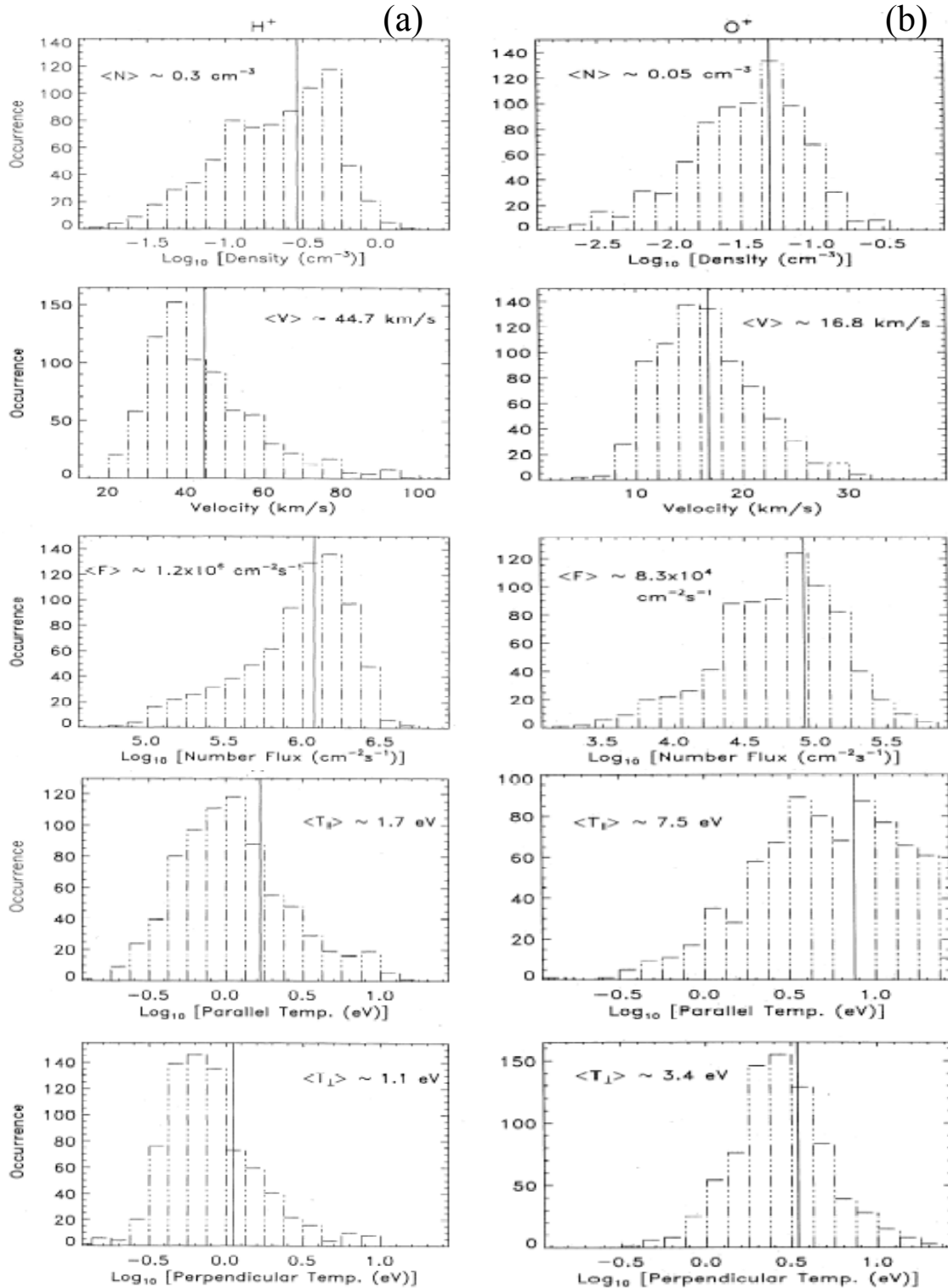


Figure 25: Occurrence histograms of (a) H^+ and (b) O^+ polar wind (from top to bottom) density, parallel velocity, flux, and temperature, and perpendicular temperature observed on POLAR at 50,500 km altitude near solar minimum (Su et al., 1998)

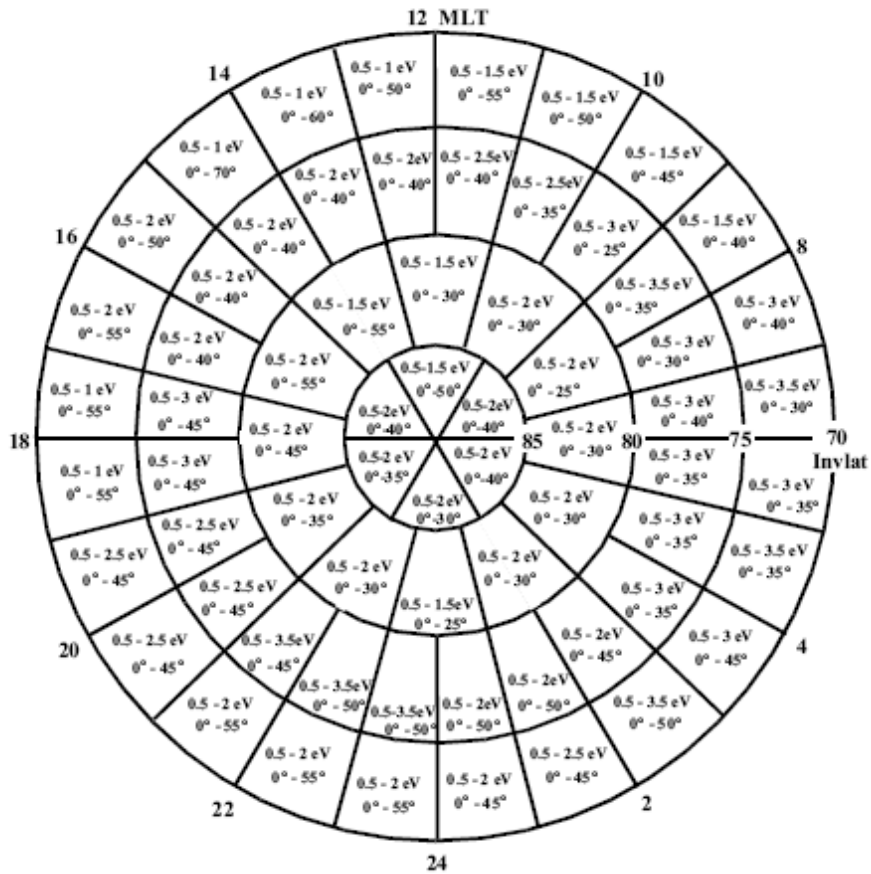


Figure 26: H⁺ polar wind full-width-half-maximum (FWHM) energy and pitch angle range observed on POLAR at 5000 km altitude as a function of invariant latitude and MLT (Huddleston et al., 2005)

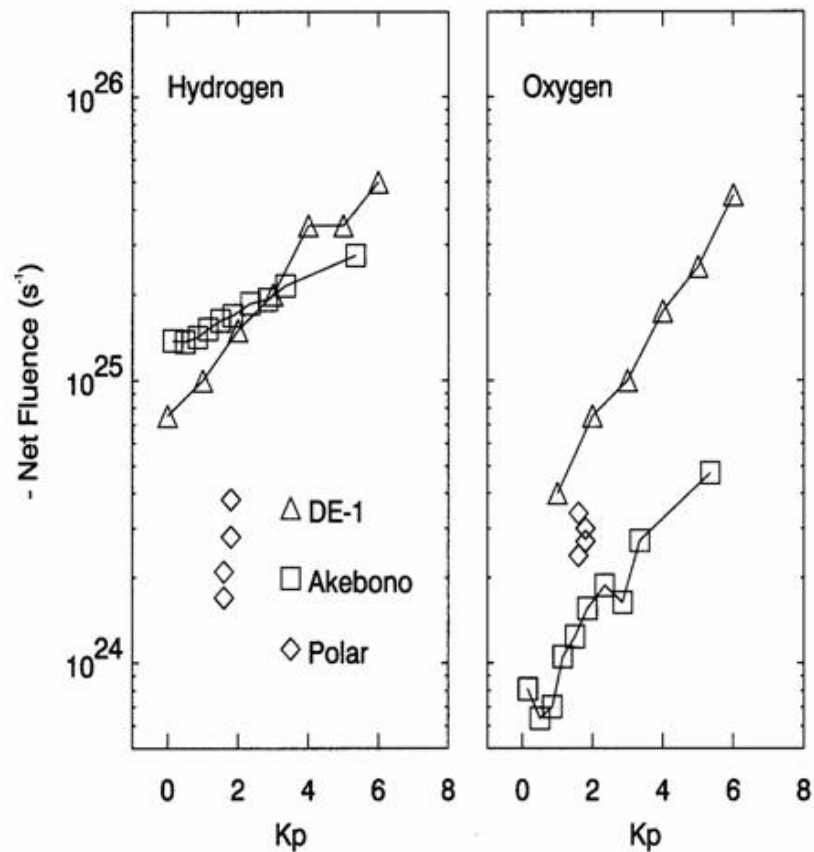


Figure 27: Integrated H⁺ and O⁺ ion outflow rates over all MLT and invariant latitudes in the high-latitude ionosphere near solar minimum as a function of Kp. squares: low-energy rate on Akebono below 9000 km, triangles: suprathermal energy rate on DE-1 above 16000 km, diamonds: suprathermal energy rate on POLAR below 9000 km (Cully et al., 2003)